Investigating the Role of Microstructure in Bone Permeability

by

Thoma Beno

A dissertation submitted to the Graduate Faculty in Engineering in partial fulfillment of the requirements for the degree of Doctor of Philosophy, The City University of New York

2005

INFORMATION TO USERS

The quality of this reproduction is dependent upon the quality of the copy submitted. Broken or indistinct print, colored or poor quality illustrations and photographs, print bleed-through, substandard margins, and improper alignment can adversely affect reproduction.

In the unlikely event that the author did not send a complete manuscript and there are missing pages, these will be noted. Also, if unauthorized copyright material had to be removed, a note will indicate the deletion.

ProQuest Information and Learning Company
300 North Zeeb Road
P.O. Box 1346
Ann Arbor, MI 48106-1346

This manuscript has been read and accepted for the Graduate Faculty in Engineering in satisfaction of the dissertation requirement for the degree of Doctor of Philosophy.

1/12/05
Date

Professor Susannah P. Fritton, Ph.D.

Chair of Examining Committee

1/18/2005
Date

Professor Mumtaz Kassir, Ph.D.

Executive Officer

Stephen C. Cowin, Ph.D.

Ali M. Sadegh, Ph.D.

Stephen B. Doty, Ph.D.

Supervisory Committee

THE CITY UNIVERSITY OF NEW YORK

ABSTRACT

INVESTIGATING THE ROLE OF MICROSTRUCTURE IN BONE PERMEABILITY

By

Thoma Beno

Adviser: Professor Susannah P. Fritton

Osteocyte shear stresses and cytoskeleton deformation resulting from bone interstitial fluid flow in the lacunar-canalicular porosity have been proposed to be involved in bone's mechanotransduction mechanism. However, the fluid flow properties that regulate bone's adaptive response are poorly understood. We first present a two-step analytical approach to determine the degree of anisotropy of the permeability of the lacunar-canalicular porosity in bone. In the first step, we estimate the total number of canaliculi emanating from each osteocyte lacuna based on published measurements for several species (chick, rabbit, cow, horse, dog, and man). In the second step, we determine the local three-dimensional permeability of the lacunar-canalicular porosity for these species by adapting a previously developed microstructural model. Permeability coefficients for the lacunar-canalicular porosity were found to exhibit local orthotropic symmetry for all species examined. We next designed experiments that provide a complete three-dimensional characterization of bone's microstructure to confirm and

quantify the essential bone parameters used in our model. Measurements of the osteocyte lacuna axes length, the volumetric lacunae density, the number of canaliculi emanating per lacuna, the number of canaliculi intersected by the bone territory assigned to each lacuna, and the canaliculus annulus size were obtained in rat bone using confocal laser scanning microscopy. The experimentally measured number of canaliculi emanating per osteocyte lacuna falls within the range of values estimated in our theoretical study. One aspect evident in rat bone that was not considered in the theoretical study was that many canaliculi emanating from the osteocyte lacuna exhibited branching. The permeability coefficients calculated using the rat confocal lacunar-canalicular measurements were found to represent local orthotropic symmetry of bone permeability, although the degree of orthotropy was different from our previous theoretical calculations mostly due to the branching of canaliculi. The local lacunar-canalicular permeability coefficients presented here will provide an important material property dataset that can be used to build poroelastic finite element models of bone. These finite element models will also include the vascular porosity, thus providing the most realistic models to date to solve for load-induced interstitial fluid pressure and velocity fields in complex bone geometries.

ACKNOWLEDGEMENTS

I would like to express my deepest gratitude to my mentor, Professor Susannah Fritton, who has influenced me greatly. Over the past several years, she taught me how to become a real scientist. Her enthusiasm for the research, and her work style is greatly appreciated.

Great thanks to Professors Stephen Cowin and Ali Sadegh for their wonderful scientific advice, careful guidance and encouragement. Professors Cowin and Sadegh have been extremely kind to me. In the past, they taught me a number of graduate courses and also gave me many wonderful ideas for my research. I appreciate all they have done for me during this time.

I wish to extend special thanks to Dr. Stephen Doty for his guidance and advice with the experimental part of this research. Many thanks go to Dr. Mitch Schaffler for providing the basic fuchsin protocol. I am also grateful to Ms. Leona Cohen-Gould for her technical assistance with the confocal microscopy.

I would like to thank the staff of the New York Center for Biomedical Engineering. I have to mention Cesare Ciani, a graduate student fellow and a good friend of mine who has helped me enormously, including overseeing bone specimen preparation for the confocal microscopy studies.

Finally, but not least I would like to thank my family especially my parents, my wife, Christine Beno and my son, James Beno. I will always appreciate their encouragement and love. Christine has always been there for me through these tough years. Whenever I have difficulties, she supports and encourages me. Thanks.

This research is supported by grants from NIH/NIAMS (AR46429), Whitaker Foundation (RG-01-0440) and PSC-CUNY (65736).

Table of Contents

List of Tables

List of Illustrations and Diagrams

Chapter 1 Introduction

1. 1 Bone Structure Types

Bone tissue differs from other connective tissues by its rigidity and hardness owing to the mineral impregnated in the predominately collagen matrix. Bone enables the skeleton to maintain the shape of the body and to protect the soft tissues of the cranial and thoracic cavities. It provides the framework for the bone marrow and transmits the force of the muscular contraction from one part of the body to another during movement. The next three sections (1.1.1, 1.1.2, and 1.1.3) briefly describe the macroscopic structure of bone, bone tissue classification, and the microscopic structure of bone, respectively.

1.1.1 Macroscopic Structure of Bone

On a gross level, all bones are composed of two basic architectural structures: a) cortical or compact bone; and b) trabecular or cancellous bone (Figs. 1-1 & 1-2). With the exception of microscopic channels, cortical bone is a dense solid mass. Trabecular bone, in contrast, appears as a lattice of rods, plates, and arches individually known as trabeculae.

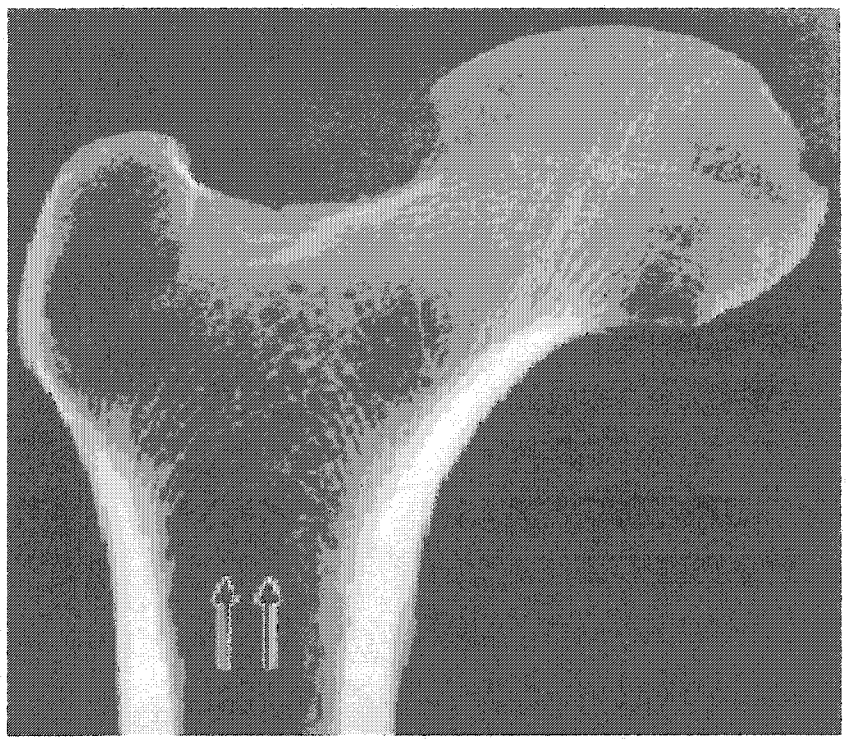

Figure 1-1. Bone section of proximal end of femur (Adapted from Jee, 2001).

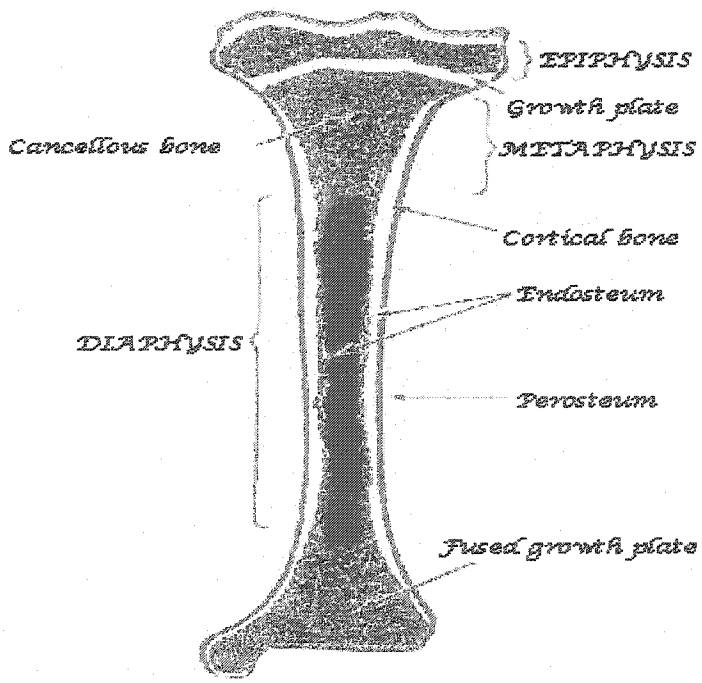

Figure 1-2. Schematic diagram of tibia (Adapted from Jee, 2001).

A typical adult long bone consists of a central cylindrical shaft, or diaphysis, and two roughly spherical ends, the epiphyses, which are connected to the diaphysis by two cone shaped regions, the metaphyses (Fig. 1-2). Whereas the diaphysis is primarily compact in structure, the epiphysis and metaphysis are mainly composed of interior trabecular bone with a shell of compact bone.

1.1.2 Bone Tissue Classification

Bone tissue is either classified in relation to the spatial orientation of the collagen fibers or the time of appearance during ontogenesis. In Table 1-1 we report the most generally accepted classifications to date: the classification according to the classical histology and that maintained by Marotti et al. (1996).

Classical Histology	Marotti et al., 1996
(A) Collagen fiber texture: Woven-fibered bone Parallel-fibered bone: Non-lamellar bone Lamellar bone	(A) Collagen fiber textures Woven-fibered bone: Non-lamellar bone Lamellar bone Parallel-fibered bone
(B) Time of appearance Primary bone: Woven-fibered bone Parallel-fibered bone Secondary bone: Lamellar bone	(B) Time of appearance Primary bone: Woven-fibered bone Parallel-fibered bone Lamellar bone Secondary bone: Lamellar bone

Table 1-1. Classification of bone tissue (Adapted from Marotti et al., 1996).

Woven-fibered bone is the first to appear in both phylogeny and ontogeny and for this reason it is also referred to as immature bone. In woven-fibered bone, the coarse bundles of collagen fibers are irregularly arranged and no correlation between these fibers

and osteocyte lacuna orientation is established. Parallel-fibered and lamellar bone consist of known collagen fiber orientation relative to the orientation of the major axis of the osteocyte lacuna (Marotti et al., 1996). Whereas parallel-fibered bone is found mainly in primary osteons and in several secondary osteons, lamellar bone, which is referred to also as mature bone, forms mainly as a consequence of bone remodeling, i.e., of the replacement of primary bone; it is present mostly in secondary bone and can also be found in primary osteons (Marotti et al., 1996).

Primary bone, which is referred to also as additional bone, only forms during skeletal growth and bone modeling and is present in all animal species having a bony skeleton. Secondary bone, also referred to as substitutional bone, is only found in those animal species whose skeleton undergoes bone remodeling and thus the basic difference between secondary and primary bones derives from the fact that secondary bone is always outlined by a cement line, which is not present in primary bone. Haversian systems or osteons have been classified as primary osteons and secondary osteons. While in primary osteons, the collagen framework forms a continuum with the surrounding fibrillar matrix, in secondary osteons the collagen framework is discontinued from the surrounding matrix by the cement line. In Table 1-2, we report the most generally accepted classifications to date for the Haversian systems: the classification according to the classical histology and that proposed by Marotti et al. (1996).

Classical Histology	Marotti et al., 1996
Primary osteons Woven-fibered bone Parallel-fibered bone	Primary osteons Woven-fibered bone Parallel-fibered bone Lamellar bone
Secondary osteons Lamellar bone: Longitudinal lamellae Transverse lamellae Alternate lamellae	Secondary osteons Woven-fibered bone Parallel-fibered bone Lamellar bone

Table 1-2. Classification of Haversian systems (Adapted from Marotti et al., 1996).

The histology classification given in Tables 1-1 and 1-2 is mostly based on the model of Gebhardt (1906). According to this model, all lamellae are fibrous layers that have the same collagen density and all collagen fibers are parallel to one another, the difference between successive lamellae consisting solely in the orientation of the fibers, which may vary through an angle of 0 – 90 °. This model is accepted by a majority of bone researchers (Lacroix, 1951; Weimann and Sicher, 1955; Pritchard, 1956; McLean and Urist, 1961; Ascenzi et al, 1965; Ascenzi and Benvenuti, 1986; Giraud-Guille, 1988; Weiner et al., 1997), is presented in histology textbooks, and has been supported lately by the fact that low magnification transmission electron microscopy does not appear to reveal any significant difference in collagen density between adjacent lamellae (view maintained by Mitch Schaffler, private communication).

The classical histology classification given in Tables 1-1 and 1-2 has been revised by Marotti and his co-workers in light of new findings based on recent polarized light, high magnification scanning electron microscopy (SEM) and high magnification transmission electron microscopy (TEM) studies (Marotti and Muglia, 1988; Marotti, 1990; Marotti, 1993; and Marotti et al., 1994a,b). According to Marotti (1996) both high

magnification SEM and transmitted light microscopy show that lamellar bone is made up of alternating collagen-rich (dense or also referred to as acellular lamellae – about 1.8 to 2 μm thick) and collagen-poor (loose or also referred to as cellular lamellae – about 4 μm thick) lamellae layers, all having a highly interwoven arrangement of these fibers.

Although the problem of bone classification in relation to the spatial orientation of the collagen fibers or the time of appearance during ontogenesis is a matter of much speculation and controversy and no satisfactory consensus has been reached among all bone researchers, the classification given in Tables 1-1 and 1-2 is the most generally accepted classification to date.

1.1.3 Microscopic Structure of Bone

Spaced throughout compact and cancellous bone are small cavities, or lacunae, connected by thin tubular channels called canaliculi. Entrapped bone cells, or osteocytes, and their long cytoplasmic processes occupy the lacuna and canaliculi. These cell processes within canaliculi communicate by gap junctions with processes of osteocytes lying in adjacent lacunae (Fig. 1-3). Some canaliculi open to extracellular fluid at the bone surfaces, thus forming an anastomosing network for nutrition and metabolic activities of the osteocytes (Fig. 1-3).

How canaliculi are oriented in three-dimensions has not been analyzed in detail. While a lot of photographic evidence of the cross-section of a lacuna and its canaliculi orientation can be found in the literature, there is very little quantification of the three-dimensional osteocyte lacuna architecture and canaliculi orientation. One exception is the work of Marotti (1979, 1996), which has characterized the lacuna and canaliculi

microstructure in cross, longitudino-radial and longitudino-tangential sections, respectively (Fig. 1-4).

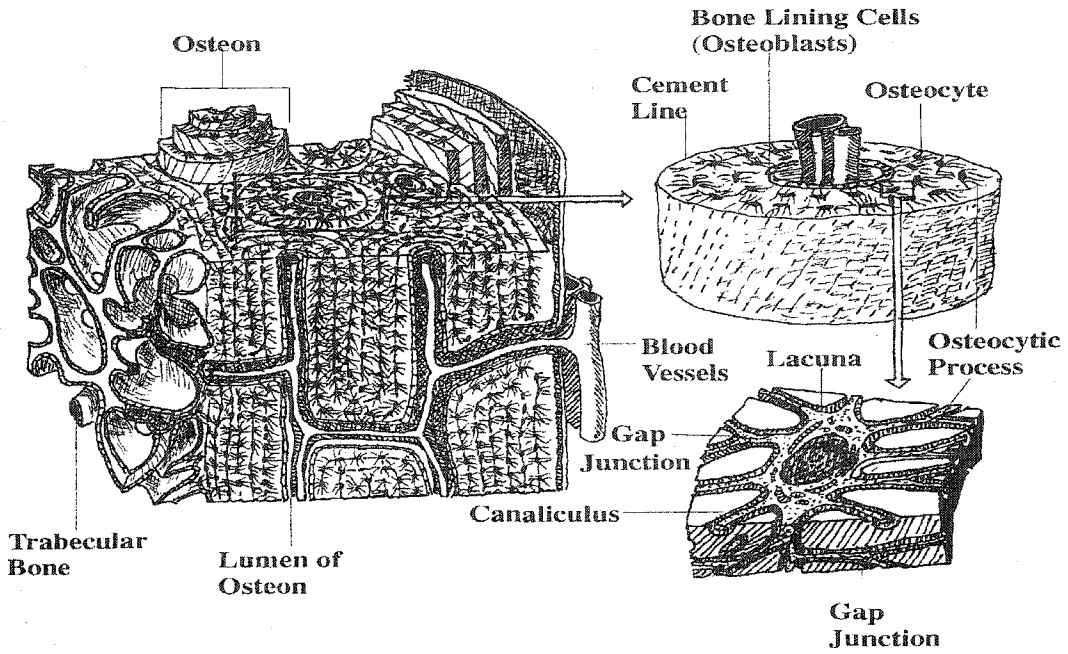

Figure 1-3. *Structure of compact bone (Adapted from Carola et al., 1990).*

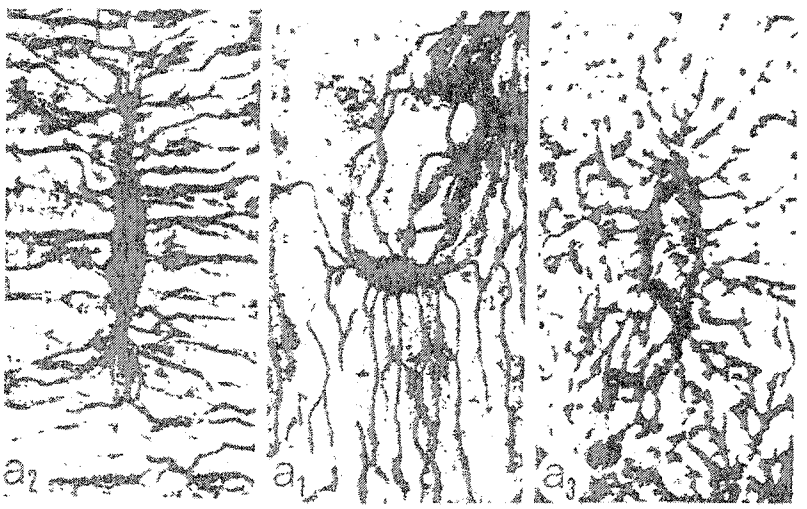

Figure 1-4. *Histological cross-section* (a_1), *longitudino-radial section* (a_2), *and longitudino-tangential section* (a_3) *showing the lacuna shape, size and canaliculi distribution from a human osteon with longitudinally arranged collagen fibers (Adapted from Marotti, 1979).*

All major activities take place on the surfaces of the mineralized matrix. These surfaces have been classified into four types: a) periosteal; b) Haversian or osteonal; c) cortical-endosteal; d) and trabecular-endosteal surfaces (Cowin, 1999). The periosteal surface is the outer boundary of adult bone. It is located between the outer circumferential lamellae and the periosteum. The periosteum is a specialized membrane, covering most of the exterior surface of the bone (Fig. 1-2) and it is made up of an inner layer of multiple layers of bone cells at different stages of differentiation and an outer dense layer of collagenous fibers and fibroblasts (Cowin, 1999). The cortical-endosteal surface is the interface between the mineralized matrix and the medullary canal. The trabecular-endosteum surface is made up of the surfaces of the rods, plates, and arches of trabeculae, which form the outer limits of the marrow cavities.

Further, there are four bone interfaces relevant to fluid flow in bone. The interfaces are structures of different thickness and permeability. These interfaces are: a) periosteum; b) cement lines; c) lacunae-canaliculi interface; and d) the cellular interface (Cowin, 1999). The cellular interface includes all the surfaces of the tubular cavities of bone that contain the vasculature, the osteonal canals and the Volkmann canals, as well as the endosteum and the inner layer of the periosteum (Cowin, 1999). While the first three interfaces are believed to be relatively impermeable, the last one shows very little hydraulic resistance to bone fluid flow.

1.2 Bone Porosity

There are three porosity compartments in cortical and trabecular bone: the vascular porosity, the lacunar-canalicular porosity, and the collagen-apatite porosity

(Cowin, 1999) (Fig. 1-3). A useful way to classify bone porosity is to categorize it as effective bone porosity (continuous or interconnected bone porosity) and non-effective bone porosity (discontinuous or isolated bone porosity). Based on the above classification the vascular porosity and the lacunar-canalicular porosity are effective bone porosities while the collagen-apatite porosity is a non-effective bone porosity. In the porous bone matrix, the fluid in these porosities is called bone fluid or interstitial fluid and is considered to have the viscosity of salt water (Cowin, 1999).

1.3 Fluid-Related Mechanisms of Bone Mechanosensation

The mechanism by which bone cells sense mechanical loading and decide the deposition or resorption of bone tissue has been the main objective of many recent studies. A number of possible mechanisms have been proposed to provide the link between mechanical loading and biological responses. One mechanism involves strain as a direct means for the mechanotransduction of bone cells and tissue. Other mechanisms involve straining as an indirect means of the mechanotransduction. Some research suggests that mechanically induced electrical signals such as strain-generated potentials (SGPs) provide the mechanotransduction signal to bone cells. Another mechanism emphasizes the role of fluid flow through the canaliculi and lacunae in producing shear stresses and causing cytoskeleton deformation at the cellular level membranes and thus activating biochemical responses in those cells (Cowin et al., 1991; Weinbaum et al., 1994; You et al., 2001).

1.3.1 Fluid Flow in Bone

Fluid flow in bone is possible only if at least part of the pore space is interconnected. When considering the permeability of bone, we immediately must think in terms of the force that makes the bone fluid flow. It is pressure gradients (e.g., due to mechanical loading) that make the bone fluid flow and it is believed that this fluid flow in the lacunar-canalicular porosity is involved in bone's mechanosensory system by applying a shearing stress to bone cell membranes or causing cytoskeleton deformation and thus activating biochemical responses in those cells that lead to the process of microstructural change (known as bone remodeling). This remodeling takes place on the surfaces of the mineralized matrix (surface remodeling) and includes both bone formation and bone resorption.

1.3.2 Strain Generated Potentials (SGPs)

Load-induced fluid flow has been measured indirectly using electrodes to record SGPs. SGPs are caused by matrix deformation and represent the voltage difference between the upstream and downstream sides of a specimen undergoing mechanical loading. This difference in voltage, in turn, occurs when fluid flow, due to mechanical loading, transports the positive portion of the electrical charged double layer that exists at the fluid solid interface (Salztein et al., 1987). Because SGPs can be directly measured in bone, they serve as an indirect measurement of interstitial fluid flow. Otter et al. (1992, 1994) and Qin et al. (2002) measured the SGPs due to mechanical loading (Fig. 1-5).

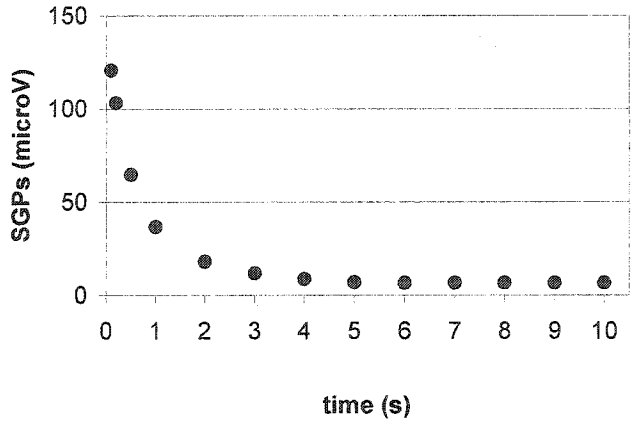

Figure 1-5. *SGPs decay to zero when a bone specimen is step-loaded (Adapted from Otter et al., 1992).*

1.4 Bone Mechanical Properties

Bone is found to exhibit anisotropic behavior with respect to both solid and fluid constituents (Ashman et al., 1984; Li et al., 1987; Ochoa et al., 1992; Nauman et al., 1997; Cowin, 1999; Kohles et al., 2001).

1.4.1 Stiffness of Solid Part

Hooke's law governs the behavior of the solid part of bone. For linear anisotropy, the following tensorial notations give the stress-strain relations:

$T_{ij}=C_{ijkl}E_{kj}$ In 3D space Eq. 1-1

$T_a=C_{ab}E_b$ In 6D space Eq. 1-2

where C_{ijkl} are the elasticity coefficients of the fourth rank tensor

C_{ab} are the elasticity coefficients of the second rank tensor

T_{ij} and T_a are the total stresses in the solid part given in 3D and 6D, respectively

E_{kj} and E_b are the total strains in the solid part given in 3D and 6D, respectively

Different material symmetries are characterized by a unique number of independent elasticity coefficients. For example, nine independent elastic constants (three Young's moduli: E_1, E_2 and E_3, three Poisson's ratios: ν_{12}, ν_{13} and ν_{23}, and three shear modulus G_{12}, G_{23} and G_{13}) would characterize orthotropic material symmetry; five independent elastic constants (two Young's moduli: E_1 and E_3, two Poisson's ratios: ν_{12} and ν_{13} and one shear modulus: G_{23}) would characterize transversely isotropic material symmetry; and two independent elastic constants (one Young's modulus: E and one Poisson's ratio: ν) would characterize isotropic material symmetry. The most general degree of anisotropy assumed for bone is that of orthotropic material symmetry (Ashman et al., 1984). Values for the nine elastic constants needed (C_{11}, C_{22}, C_{33}, C_{44}, C_{55}, C_{66}, C_{12}, C_{23}, C_{13}) to fully characterize the orthotropic behavior of the solid part of bone have been reported in the literature (Table 1-3),

where $C_{11} = (1 - \nu_{23}\nu_{32})/E_2E_3\Delta$; Eq. 1-3

$C_{22} = (1 - \nu_{13}\nu_{31})/E_1E_3\Delta$; Eq. 1-4

$C_{33} = (1 - \nu_{12}\nu_{21})/E_2E_1\Delta$; Eq. 1-5

$C_{44} = G_{23}$; Eq. 1-6

$C_{55} = G_{13}$; Eq. 1-7

$C_{66} = G_{12}$; Eq. 1-8

$C_{12} = (\nu_{21} + \nu_{31}\nu_{23})/E_2E_3\Delta$; Eq. 1-9

$C_{23} = (\nu_{32} + \nu_{12}\nu_{31})/E_1E_3\Delta$; Eq. 1-10

$C_{13} = (\nu_{31} + \nu_{21}\nu_{32})/E_2E_3\Delta$; and Eq. 1-11

$$\Delta = (1-\nu_{12}\nu_{21}-\nu_{23}\nu_{32}-\nu_{31}\nu_{13}-2\nu_{21}\nu_{32}\nu_{13})/E_1E_2E_3. \qquad \text{Eq. 1-12}$$

Reference	Lang (1970)	Van Buskirk and Ashman (1981)	Katz et al. (1984)	Reilly and Burstein (1975)	Zioupos et al. (1995)
C_{11}	19.7	20.0	21.2	17.0	13.69
C_{22}	19.7	21.7	21.0	17.0	13.69
C_{33}	32	30.0	29.0	29.6	24.88
C_{44}	5.4	6.56	6.3	3.6	4.92
C_{55}	5.4	5.85	6.3	3.6	4.92
C_{66}	3.8	4.74	5.4	3.4	4.14
C_{12}	12.1	10.91	11.1	10.2	5.42
C_{23}	12.6	11.45	11.7	9.8	8.58
C_{13}	12.6	11.53	12.7	9.8	8.58

Table 1-3. Elastic stiffness (in GPa) of cortical bone (Adapted from Sevostianov and Kachanov, 1999).

1.4.2 Bone Permeability

Darcy's law governs the flow of interstitial fluid. One critical parameter in Darcy's formulation is the permeability coefficient, κ. Some confusion occurs here with the word "permeability." In general, permeability refers to the ease with which fluid can flow through a porous medium. Different textbooks or publications use the word "permeability" but do not necessarily associate it with its unit of measurement, making it difficult for the reader to distinguish between the words of "permeability" and "hydraulic conductivity." Because of that and due to the difficulty of determining its value for bone, leading to estimations of permeability of the lacunar-canalicular porosity ranging over

several orders of magnitude (Wang et al., 1999), it is of great importance that one associates the permeability term with its units of measurements. Hydraulic conductivity or hydraulic permeability is associated with the units of length^4/(force x time). Hydraulic conductivity normalized by the viscosity is called the specific hydraulic conductivity or simply "permeability" and has the units of length^2. This is also called the intrinsic permeability, k, and accounts only for the porous structure and not the type of fluid flowing through it. Different branches of applied sciences and different poroelastic finite element codes traditionally use different measures of permeability (Tables 1-4 & 1-5).

Oil industry	Soil scientists	Dentistry researchers	Tissue mechanicians
Darcy unit	cm/sec	m/sec • kPa	m^2

Table 1-4. Permeability units used by different branches of applied science where 1 Darcy = $9.87 \cdot 10^{-13}$ m^2.

ABAQUS	DIANA
m/s	m^4/Ns

Table 1-5. Permeability units used by different poroelastic finite element codes.

1.4.2.1 Experimental Measurements of Bone Permeability

Several studies have measured the permeability of cortical and cancellous bone (e.g., Rouhana et al., 1981; Li et al., 1987; Grimm and Williams, 1997; Qin, 1997; Nauman at el., 1999; Kohles et al., 2001; Qin et al., 2002) (Table 1-6).

Literature reference	Porosity v_0	Permeability k (m^2)
Cortical Bone		
a) Vascular porosity		
Frost (1962)	0.6	
Morris et el. (1982)	0.015	
Johnson (1984)		$1\text{-}5 \times 10^{-14}$
Schaffler et al. (1988)	0.04	
Rouhana et al. (1981)		3.0×10^{-13}
Li et al. (1987)		5.0×10^{-15} (dominated by PV)
Qin, 1997		3.8×10^{-13} - 1.9×10^{-15} in vitro (dominated by PV)
Qin, 1997		1.8×10^{-14} in vivo (dominated by PV)
b) The lacunar-canalicular porosity		
Frost (1960)	0.023	
Morris et al. (1982)	0.042	
Baylink and Wergedal (1971)	0.035	
Cancellous bone	**Orientation**	**Permeability k (m^2)**
Kohles et al. (2001) Distal femur	Proximal – Distal Anterior - Posterior Medial - Lateral	$1.15 – 8.15 \times 10^{-10}$ $1.78 – 7.26 \times 10^{-10}$ $0.78 – 3.38 \times 10^{-10}$
Lim et al. (2000) Bovine, Vertebral body	Cephadal- caudal	$0.83 – 2.43 \times 10^{-10}$
Nauman at el. (1999) Human, Vertebral body Human, Proximal femur Bovine, Proximal tibia	Longitudinal Transverse Longitudinal Transverse Longitudinal Transverse	$33 – 128 \times 10^{-10}$ $16.9 – 54.9 \times 10^{-10}$ $8.5 – 46.7 \times 10^{-10}$ $0.1 – 2.3 \times 10^{-10}$ $21.5 – 41.9 \times 10^{-10}$ $0.9 – 15.7 \times 10^{-10}$
Grimm et al. (1997) Human, Calcanus	Medial - Lateral	$24.7 – 61.1 \times 10^{-10}$
Hui et al. (1996) Porcine, Femoral head	Longitudinal Transverse	$0.19 – 0.79 \times 10^{-10}$ $0.12 – 0.32 \times 10^{-10}$
Beaudoin et al. (1991) Bovine, Proximal tibia	Proximal – Distal	$40.4 – 113 \times 10^{-10}$
Ochoa et al. (1992) Human, Proximal tibia	Proximal – Distal Medial - Lateral	0.0105×10^{-10} 0.084×10^{-10} 0.0275×10^{-10}

Table 1-6. Permeability and porosity values for cortical and cancellous bone (Adapted in part from Zhang et al., 1998).

The values of permeability reported in the literature represent the permeability through lumped porosities and none of the techniques is able to differentiate between the permeability of the vascular porosity and the lacunar-canalicular porosity. To our knowledge, no one has reported experimentally measured values of the permeability for the lacunar-canalicular porosity, although Smit et al. (2002) have reported indirect lacunar-canalicular permeability measurements via finite element estimates. The difficulty in applying the traditional permeability measurement methods at that length scale (order 100 nm) is perhaps the main reason that this experimental work has not been done to date.

1.4.2.2 Microstructural Model that Calculates Bone Permeability

Permeability of the lacunar-canalicular porosity has been quantified analytically using a microstructural model developed to calculate shear stresses on bone cells (Weinbaum et al., 1994). This model accounts for interstitial fluid flowing through a gel-like fiber matrix in the canaliculus annulus and relates the permeability coefficient, k, (m^2) to: a) the number, n, of canaliculi crossing each face of a cuboidal periodic unit cell (CPUC); b) the length, L, (μm) of the CPUC; c) the canaliculus radius, b, (nm); d) the osteocyte process radius, a, (nm); e) the radius, a_0, (nm) of the transverse fibers in the channel between the cytoplasmic process and the wall of canaliculus; and f) the spacing, Δ, (nm) between the transverse fibers in the channel between the cytoplasmic process and the wall of canaliculus (Weinbaum et al., 1994; Fig. 1-6).

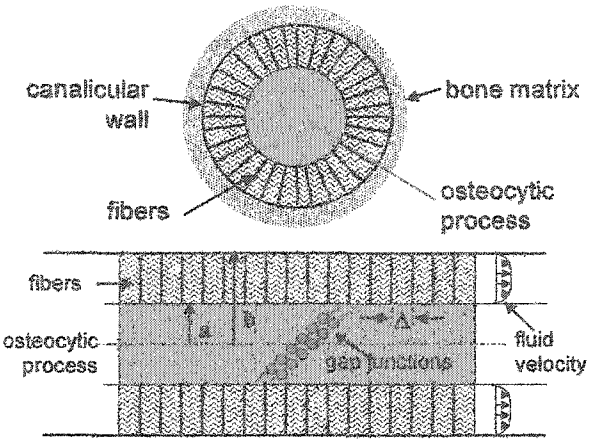

Figure 1-6. Idealized model of the cross section of canaliculi (Adapted from Weinbaum et al., 1994).

While credit goes to the above model for establishing the permeability in the lacunar-canalicular porosity, the model considers that the permeability in the lacunar-canalicular porosity is isotropic. Also, while it has been pointed out that some of the microstructural parameters employed in this model were not accurately known (Smit et al., 2002), recent studies have been designed to more accurately measure many of these microstructural parameters. You et al. (2004) measured the osteocyte process and canaliculi diameters in mature mice, reporting average values of 259 nm for the canaliculus diameter and 104 nm for the osteocyte process diameter. Wang et al. (2004) present findings from tracer studies that indicate the lacunar-canalicular pore spacing in mature rats lies in the range of approximately 6 to 10 nm; this range is consistent with the Squire et al. (2001) finding of a fiber matrix spacing of approximately 8 nm in the glycocalyx of endothelial cells. Histomorphometric comparative studies on the lacunar-canalicular network carried out by Remaggi et al. (1998) and Ferretti et al. (1999) for three types of bone tissue (woven, parallel-fibered, and lamellar) in shaft bones of several

species give mean values of lacunar axes length and number of canaliculi per lacunar perimeter length; however, they did not report the total number of canaliculi originating from each lacuna.

No study has as of yet examined the effect of the osteocyte lacuna shape, its size, and the three-dimensional canaliculi orientation to determine the degree of anisotropy of the permeability in the lacunar-canalicular porosity.

1.5 Poroelasticity Theory

Poroelasticity theory describes the interaction between the solid and fluid constituents of a porous medium, which is a solid body that contains pores, and lends itself perfectly for study of load-induced fluid movement in bone [refer to Cowin (1999) for complete coverage of this topic and its use in bone research]. Pores are void spaces, which must be distributed more or less frequently through the material if the latter is to be called porous. The pores in a porous system may be interconnected or non-interconnected. Fluid flow is possible only if at least part of pore space is interconnected (effective bone porosity). The stress-strain and strain-stress relations for isotropic linear poroelasticity are given as:

$$\sigma_{ij} + \alpha p\delta_{ij} = 2G\varepsilon_{ij} + [2G\nu/(1 - 2\nu)]\varepsilon_{kk}\delta_{ij} \qquad \text{Eq. 1-13}$$

$$2G\varepsilon_{ij} = \sigma_{ij} - [\nu/(1+ \nu)]\sigma_{kk}\delta_{ij} + \alpha[(1 - 2\nu)/(1 + \nu)]\, p\delta_{ij} \qquad \text{Eq. 1-14}$$

where G is the drained shear modulus, ν is the Poisson's ratio, α is the ratio of the fluid volume gained (or lost) in a material element due to the volume change of that element

when loaded at a small stress rate, p is the pore pressure (scalar value), σ_{ij} is the stress tensor (six components), and ε_{ij} is the strain tensor (six components) (Cowin, 1999).

There are a number of different approaches that lead to the development of the same basic equations for poroelasticity theory (Cowin, 1999). The most prominent approaches are the effective medium approach and the mixture theory approach. The mixture theory approach is based on diffusion models, while the effective medium approach employs a small but finite volume called the representative volume element (RVE) for development of constitutive equations of the porous medium (Cowin, 1999).

1.5.1 Previous Bone Poroelastic Finite Element Models

Only a few studies have used poroelastic finite element (FE) models to analyze cortical and cancellous bone (e.g., Qin, 1997; Manfredini et al., 1998; Smit et al., 2002; Steck et al., 2003). Qin (1997) and Smit et al. (2002) used isotropic poroelastic FE modeling to determine the isotropic permeability coefficient of the turkey ulna and the dog femur, respectively. Manfredini et al. (1998) verified the analytical pore pressure results of Zhang et al. (1994) via an isotropic poroelastic FE model. Steck et al. (2003) calculated the pore pressure and fluid velocities using a three-dimensional anisotropic poroelastic FE model, accounting for anisotropies in both the permeability and elasticity in the lacunar-canalicular porosity. Although the values of anisotropic permeability for the lacunar-canalicular porosity are incorporated in their model, as the authors acknowledge, they are only rough estimates derived from literature. In addition, the models do not include the vascular porosity.

1.6 Previous Theoretical Models Using a Poroelastic Formulation

A number of theoretical models previously mentioned (Weinbaum et al., 1994; Zeng at al., 1994; Zhang et al., 1994; Cowin et al., 1995; Zhang et al., 1998; Wang et al., 1999) have quantified interstitial fluid flow in bone using a poroelastic formulation. The above authors consider bone as a porous media and their solutions are based on Biot's poroelasticity theory and electro-kinetic theory. Weinbaum et al. (1994) predicted the SGPs and the fluid shear stress at the surface of osteocytic processes. Cowin et al. (1995) demonstrated that the lacunar-canalicular porosity could be the anatomical site source responsible for the SGPs. Detailed studies carried out by Zhang et al. (1994) and Zeng et al. (1995) on a one-dimensional poroelastic beam and an osteonal cylinder under cyclic loading, respectively, obtained the closed-formed solution of the pore pressures and SGPs generated in their models. Zhang et al. (1998) considered a specimen cut from an idealized long bone shaft under a suddenly applied uniform axial compressive stress of 18 MPa to produce strains of 0.1% along the long axis. Then, they estimated the peak pore pressures to be 19% in the vascular porosity and 12.3% in the lacunar-canalicular porosity. Wang et al. (1999) showed that the lacunar-canalicular pore pressure relaxes mainly through the vascular canals and that the pore pressure relaxation time is proportional to the square of the osteonal thickness and not to the bone specimen thickness, which is the case for specimens that do not contain vascular canals.

All the above theoretical models assume the osteocytic processes to be enclosed in straight cylindrical tubes. However, osteocytic processes have a sinuous trend (Marotti et al., 1992) and travel between lacunae and from lacunae to the other bone surfaces or osteonal canals through winding canaliculi channels. Therefore, for evaluation of the

effects of the canaliculi contortions on the permeability of the lacunar-canalicular porosity, it is of great importance to first provide a more complete characterization of the lacunar-canalicular network. A systematic three-dimensional analysis of an osteocyte lacuna and its canaliculi is lacking in the literature.

1.7 Confocal Laser Scanning Microscopy and its Application in Bone

To yield information on bone's inner structure various light microscopy techniques have been used. By conventional transmitted-light microscopy, specimens have to be very thin and translucent; otherwise image definition will be very poor. In many cases it is difficult to satisfy these requirements. These considerations have led to trailblazing changes in conventional microscopy and supplied a successful solution to the above problem.

Unlike the practice of even illumination in conventional microscopy, the Laser Scanning Microscopy (LSM) technique projects the light of a point light source (a laser) through a high Numeric-Aperture (NA) objective onto a certain object plane of interest as a nearly diffraction-limited focus (Fig. 1-7). However, if not for another "trick" the stray light produced outside the object plane, or the fluorescence of fluorescent specimens, would disturb the in-focus image of the object point of interest, resulting in a blurred image of poor contrast. The problem therefore is how to capture only the light coming immediately from the object point in focus, while obscuring the light coming from out-of-focus areas of the specimen.

The light reflected or the fluorescence light produced at the focus of the high-NA objective is projected onto a variable pinhole diaphragm by the same objective and a tube

lens. The focus inside the specimen and the pinhole are situated at optically conjugate points (confocal imaging). The advantage of this arrangement is the fact that essentially no other light than that coming from the object plane of interest can pass the narrow pinhole and be registered by a detector (Fig. 1-7). Unwanted light coming from other specimen areas is focused outside the pinhole, which passes only a small fraction of it. The smaller the pinhole, the less stray light or fluorescence from out-of-focus areas will get on the detector. The image point thus generated is largely free from blur caused by unwanted light.

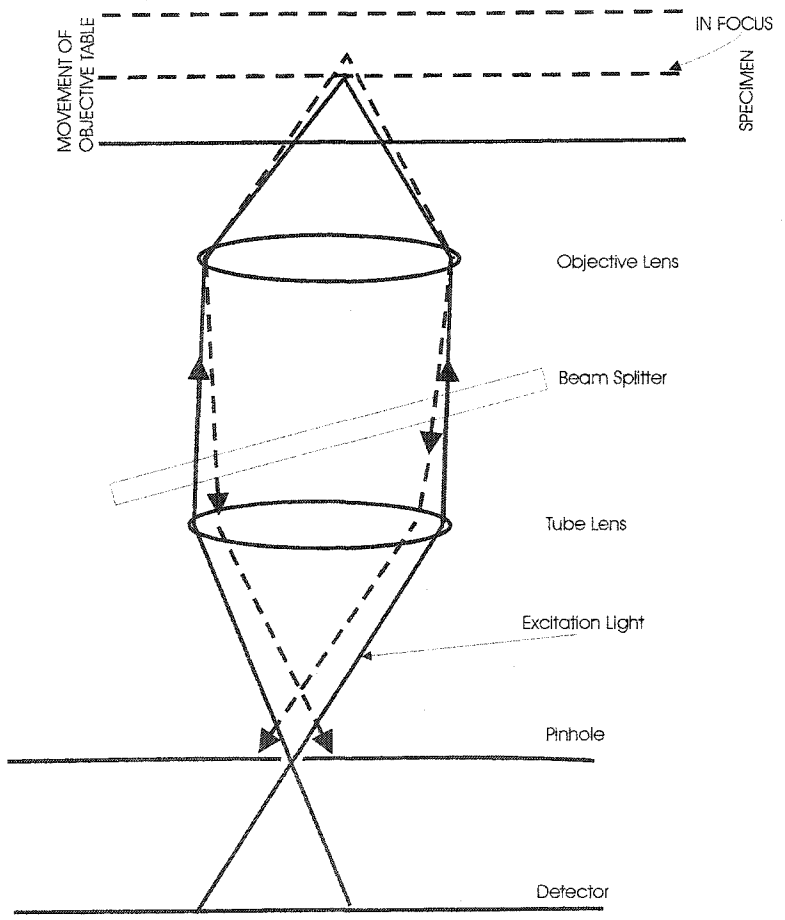

Figure 1-7. *Principles of confocal imaging (Adapted in part from Grotz et al., 1999).*

In order to obtain an image of the selected object plane as a whole, it is necessary to scan the object plane in a point-by-point, line-by-line raster by means of an XY light deflection system. The detectors convert the optical information into an electric signal. This allows the image of any object plane to be generated and stored within less than a second (Zeiss LSM 510). By a defined focusing (Z axis) movement it is possible to look at any object plane of interest. By scanning a succession of object planes in a specimen, a stack of slice images can be produced.

Confocal Laser Scanning Microscopy (CLSM) of hard tissues began in the mid 1980's, but it was not until the late 1990's when widespread application took place. CLSM has been validated using cortical bone specimens by correlating the morphology of identical areas with conventional light microscopy (Grotz et al., 1999). More recently, McCreadie et al. (2003) used the CLSM technique to obtain accurate measurements of osteocyte lacuna size and shape. Wang et al. (2004b) obtained accurate measurements of the areal osteocyte density, canalicular spacing and lacunar size via CLSM.

1.8 Clinical Significance

The forces exerted on the body are what keep muscles and bones in the body strong. If muscles and bones are not used, they become significantly weaker (during space flight, long term bed rest, etc.). The result can be bones with high risk of osteopenia (a condition characterized by loss of bone mass, decreased bone density, and enlargement of spaces), which can result in weaker bones that are more prone to fractures. Approximately 1.5 million fractures annually are attributable to osteoporosis in the USA alone, with treatment costs of at least 5-10 billion dollars per year (Riggs and

Melton, 1995). A better understanding of bone's mechanosensory system will assist in solving these critical clinical problems by developing treatments that maintain or create bone using bone's adaptive properties, thus sparing a lot of pain and money.

1.9 Overview of Chapters

Chapter 1 has emphasized the importance of more accurately determining the permeability of the lacunar-canalicular porosity. To accomplish this theoretically, a two-step analytical approach is presented in Chapter 2. We first estimated the total number of canaliculi emanating from each osteocyte lacuna based on recent published measurements from cortical bone and then we used the total number of canaliculi and their orientation to better model the local permeability of the lacunar-canalicular porosity (Chapter 2 is a manuscript in review, submitted to the *Journal of Biomechanics*). We next describe experiments that confirm and quantify the essential bone parameters used in our model. Measurements of the number of the canaliculi emanating per lacuna, the number of canaliculi intersected by the bone territory assigned to each individual osteocyte lacuna, the osteocyte lacuna axes length, the volumetric lacunae density, and the canaliculus annulus size in rat bone were obtained using different staining techniques and confocal laser scanning microscopy (Chapter 3, which is a manuscript that will be submitted to *Bone*). How the local anisotropic permeability of the lacunar-canalicular porosity (orthotropic symmetry) from Chapters 2 and 3 should be incorporated into poroelastic finite element models of human osteonal bone and whole rat tibia bone to solve for load-induced pore pressure and velocity fields is described in Chapter 4. We

finally conclude by summarizing our findings and providing some suggestions for future research (Chapter 5).

Chapter 2

Estimation of Bone Permeability Using Accurate Microstructural Measurements

Abstract

It is widely believed that interstitial fluid flow plays a role in bone's mechanosensory system by shearing bone cell membranes or causing cytoskeleton deformation and thus activating biochemical responses that lead to the process of bone adaptation. However, the fluid flow properties that regulate bone's adaptive response are poorly understood. In this paper, we present a two-step analytical approach to determine the degree of anisotropy of the permeability of the lacunar-canalicular porosity in bone. In the first step, we estimate the total number of canaliculi emanating from each osteocyte lacuna based on published measurements from parallel-fibered shaft bones of several species (chick, rabbit, cow, horse, dog, and man). In the second step, we determine the local three-dimensional permeability of the lacunar-canalicular porosity for these species by adapting a previously developed model. Our calculations show that osteocyte lacunar shape and size along with the canalicular distribution in three dimensions are parameters that determine the degree of anisotropy of the local permeability of the lacunar-canalicular porosity. We found that the number of canaliculi per osteocyte lacuna varies for different species, ranging from 41 for man to 115 for horse. Permeability coefficients were found to be different in three local principal directions, indicating local orthotropic symmetry of bone permeability in parallel-fibered cortical bone for all species examined. This two-step theoretical approach to determine the degree of anisotropy of the permeability of the lacunar-canalicular porosity will be useful for accurate quantification of interstitial fluid movement in bone.

Notation

a_l, b_l, c_l	semi-axes of the osteocyte lacunar ellipsoid
φ_i	angle increment along the arc length of the osteocyte lacunar ellipsoid
b	radius of a canaliculus
a	radius of an osteocytic process
$b - a$	canaliculus annulus -- space between the osteocytic process and the canalicular wall
q	ratio of the radius of the canaliculus, b, to the radius of the osteocytic process, a ($q = b/a$)
a_0	radius of the transverse fibers in the annulus between the osteocytic process and the canalicular wall
Δ	spacing between the fibers in the annulus between the osteocytic process and the canalicular wall
$N.Ca$	total number of canaliculi emanating from an osteocyte lacuna
$N.Lc/B.Ar$	number of lacunae per unit surface area of bone
CPUC	cuboidal periodic unit cell
L	length of the each side of the cuboidal periodic unit cell that encompasses an osteocyte lacuna and its canaliculi
T	mean surface area of bone tissue surrounding each osteocyte lacuna
PSA_{XY}	projected surface area of the osteocyte lacunar ellipsoid in the X-Y plane
PSA_{YZ}	projected surface area of the osteocyte lacunar ellipsoid in the Y-Z plane
T_{PSA}	sum of projected surface areas of the osteocyte lacunar ellipsoid in the X-Y and Y-Z planes

n_i number of canaliculi crossing each face of the cuboidal periodic unit cell perpendicular to the local axis i of the cuboidal periodic unit cell where i = 1, 2, 3 corresponds to the local X, Y, Z osteocyte lacunar axes, respectively

k_p Darcy permeability constant at the fiber matrix scale for fluid flow through the fiber matrix in the annulus surrounding the osteocytic process

α dimensionless length parameter [$\alpha = (b - a)/\sqrt{k_p}$] that is the ratio of two lengths, the width of the fluid annulus surrounding the osteocytic process, (b - a), and the thickness of the viscous layer that forms near the canaliculus wall, $\sqrt{k_p}$

$k_{\infty i}$ Darcy's permeability constants of the lacunar-canalicular porosity along axis i of the cuboidal periodic unit cell where i = 1, 2, 3 corresponds to the local X, Y, Z osteocyte lacunar axes, respectively, with no pericellular fiber matrix present

k_i Darcy's permeability constants of the lacunar-canalicular porosity along axis i of the cuboidal periodic unit cell where i = 1, 2, 3 corresponds to the local X, Y, Z osteocyte lacunar axes, respectively

2.1 Introduction

Several experimental studies have measured the permeability of cortical and cancellous bone, an important property that influences interstitial fluid flow through the bone pores (Rouhana et al., 1981; Li et al., 1987; Grimm and Williams, 1997; Qin, 1997; Nauman et al., 1999; Lim and Hong, 2000; Kohles et al., 2001). The values of permeability reported represent the permeability through lumped porosities; none of the techniques differentiates between the permeability of the lacunar-canalicular porosity and the vascular porosity or intertrabecular porosity. The characteristic lineal dimension of the vascular porosity and intertrabecular porosity is several orders of magnitude larger than that of the lacunar-canalicular porosity and thus these porosities act as a low pressure reservoir that interstitial fluid from the lacunar-canalicular porosity can flow into and out of (Cowin, 1999). To our knowledge, no one has reported experimentally measured values of the permeability for the lacunar-canalicular porosity (Sander and Nauman, 2003). The fact that the vascular porosity is intermingled with the lacunar-canalicular porosity and the difficulty in applying the traditional permeability measurement methods at the length scale of the lacunar-canalicular porosity (order 100 nm) are perhaps the main reasons that this experimental work has not been done to date.

Because the vascular porosity is at a low pressure, the lacunar-canalicular porosity appears to be the most important porosity for the consideration of mechanical and mechanosensory effects in bone. Osteocyte shear stresses and cytoskeleton deformation resulting from bone fluid flow in the lacunar-canalicular porosity have been proposed to be involved in bone's mechanotransduction mechanism (Hillsley and Frangos, 1994; Weinbaum et al., 1994; Klein-Nulend et al., 1995; You et al., 2001). An accurate

quantification of the permeability of the lacunar-canalicular porosity is needed not only to capture bone's true anisotropic behavior while performing finite element pore pressure and stress analyses, but also for further investigating permeability's role in the mechanotransduction mechanism and osteocyte nutrition.

A number of studies have used poroelastic finite element models to analyze the response of cortical bone to mechanical loading (e.g., Qin, 1997; Manfredini et al., 1999; Smit et al., 2002; Steck et al., 2003). Except for Smit et al. (2002), the models lump the vascular porosity and the lacunar-canalicular porosity together even though their permeabilities differ by several orders of magnitude. Also, except for the model of Steck et al. (2003) the models assume the bone permeabilities to be isotropic, probably due to the fact that there is no complete anisotropic poroelastic parameter dataset for the bone permeabilities. The values of anisotropic permeability for the lacunar-canalicular porosity employed by Steck et al. (2003) were only rough estimates derived from literature. The literature contains no reports on the degree of anisotropy of the permeability of the lacunar-canalicular porosity, a topic to be addressed here.

In order to obtain reasonable estimates of the permeability of the lacunar-canalicular porosity a microstructural model has been developed to quantify bone permeability and shear stresses on bone cells (Weinbaum et al., 1994; Cowin et al., 1995). While it has been pointed out that some of the microstructural parameters employed in this model were not accurately known (Smit et al., 2002), recent studies have been designed to more accurately measure many of these microstructural parameters. You et al. (2004) measured the osteocyte process and canaliculi diameters in mature mice, reporting average values of 259 nm for the canaliculus diameter and 104

nm for the osteocyte process diameter. Wang et al. (2004) present findings from tracer studies that indicate the lacunar-canalicular pore spacing in mature rats lies in the range of approximately 6 to 10 nm; this range is consistent with the Squire et al. (2001) finding of a fiber matrix spacing of approximately 8 nm in the glycocalyx of endothelial cells. Histomorphometric comparative studies on the lacunar-canalicular network carried out by Remaggi et al. (1998) and Ferretti et al. (1999) for three types of bone tissue (woven, parallel-fibered, and lamellar) in shaft bones of several species show that the shape of osteocyte lacunae resembles that of a triaxial ellipsoid in parallel-fibered and lamellar bone and that of a globular or lenticular shape in woven bone. For all animals the mean values of lacunar axes lengths and the number of canaliculi per lacunar perimeter length were measured; however, the total number of canaliculi originating from each lacuna and the orientation of the canaliculi were not quantified.

The purpose of this study was to use these recent lacunar and canalicular measurements to estimate the number of canaliculi emanating from each osteocyte lacuna and to estimate the local permeability coefficients of the lacunar-canalicular porosity in three dimensions. Determination of the local permeability coefficients will assist in quantifying interstitial fluid movement by determining the degree of bone fluid anisotropy in the lacunar-canalicular porosity.

2.2 Methods

Estimating the number of canaliculi emanating from each osteocyte lacuna

To estimate the total number of canaliculi (*N.Ca*) originating from each osteocyte lacuna along with the three-dimensional canalicular distribution, we used measurements from Remaggi et al. (1998) for parallel-fibered bone from six species. We used the parallel-fibered bone measurements and not the lamellar and woven bone measurements from Ferretti et al. (1999) because the parallel-fibered bone measurements were more complete. The key measurements from Remaggi et al. (1998) used were the osteocyte lacunar density, the mean values of the three axes of the osteocyte lacunar ellipsoid, and the number of canaliculi departing from the whole outline of the mid cross-sectional slice of the lacuna (Fig. 2-1).

We first represented the triaxial lacunar ellipsoid with the Cartesian equation for a general ellipsoid:

$$\left(\frac{x}{a_l}\right)^2+\left(\frac{y}{b_l}\right)^2+\left(\frac{z}{c_l}\right)^2=1, \qquad \text{Eq. 2-1}$$

where the lacunar semi-axes a_l, b_l, and c_l were taken from Remaggi et al. (1998) for six species: chick, rabbit, bovine, horse, dog, and man (only the species containing vascular canals were considered; frog shaft bone does not contain vascular canals and thus was not included in our study). Because these data were obtained from two-dimensional measurements, we developed two methods to estimate the three-dimensional density and distribution of canaliculi emanating from the lacunae: 1) a slicing method and 2) a surface area method.

With the slicing method, because the only canaliculi data provided by Remaggi et al. (1998) for all six species were the number of canaliculi per cross-sectional cut (the number of canaliculi per unit perimeter length), we "sliced" the lacunar ellipsoid sequentially perpendicular to the long axis of the ellipsoid and assumed canaliculi to be within the same plane of cut in order to estimate the three-dimensional canalicular distribution (Fig. 2-2). In this way the effective total perimeter length of the lacuna was estimated. Because the choice of the number of slices was somewhat arbitrary and directly affected the estimate of the number of canaliculi per lacuna (*N.Ca*), a low and high total lacunar perimeter length were estimated using a total of 5 slices (where each slice corresponds to a φ increment of 30°, Fig. 2-3) and 35 slices (where each slice corresponds to a φ increment of 5°), respectively. The lower slice number is an arbitrary minimum chosen to coarsely represent the lacunar shape and the higher slice number corresponds to approximately 0.5 μm thick slabs, the approximate diameter of a canaliculus (Knapp et al., 2002; You et al., 2004), and thus the maximum number of slices that could represent the lacunar shape. To obtain *N.Ca* for both the low and high estimates, the total perimeter lengths for all cross sections (all the slices perpendicular to the long axis of the lacuna, Figs. 2-2 and 2-3) were multiplied by the mean number of canaliculi per unit perimeter length reported by Remaggi et al. (1998) for each species.

With the surface area method, the total surface area of the triaxial ellipsoid representing the osteocyte lacuna was first calculated from the mean values of the lacunar axes provided by Remaggi et al. (1998) using Mathematica (Wolfram Research Inc., USA). The number of canaliculi per unit surface area was derived from the reported values of the mean number of canaliculi per unit perimeter length (Remaggi et al., 1998):

the number of canaliculi/10 μm was squared to give the number of canaliculi/100 μm^2, an estimation shown to be valid by Marotti et al. (1995). The total number of canaliculi per lacuna (*N.Ca*) was then calculated for each of the six species by multiplying the lacunar surface area by the estimated values of the number of canaliculi per unit surface area. To see how the surface area method compared to the high and low estimates using the slicing method, we determined how many slices were needed to give a *N.Ca* equaling the *N.Ca* estimated by the surface area method (while these findings will be reported in the Results section, it should be noted that the number of slices lay between 5 and 35, which means that the *N.Ca* calculated with the surface area method lies between the high and low estimates using the slicing method).

Estimating the local permeability constants of the lacunar-canalicular porosity

The estimation of the local permeability constants for the lacunar-canalicular porosity was based on the microstructural model of Weinbaum et al. (1994). This model accounts for interstitial fluid flowing through a fiber matrix in the canaliculus annulus and relates the permeability coefficient, k, (m^2) to the number, n, of canaliculi crossing each face of a cuboidal periodic unit cell (CPUC) that surrounds the osteocyte lacuna; the length, L, (μm) of the CPUC; the canaliculus radius, b, (nm); the osteocyte process radius, a, (nm); the radius, a_0, (nm) of the transverse fibers in the channel between the osteocyte process and the wall of the canaliculus; and the spacing, Δ, (nm) between the fibers in the channel between the osteocyte process and the wall of the canaliculus. Weinbaum et al. (1994) assumed the bone tissue was isotropic and thus the same number of canaliculi n crossed the surface of the CPUC in each principal direction. Expanding the Weinbaum et al. (1994) model to account for the three-dimensional distribution of the

canaliculi and thus an anisotropic number of canaliculi ($n = n_i$) crossing each face of the CPUC (Fig. 2-4), the permeability coefficients for the lacunar-canalicular porosity with no fiber matrix surrounding the osteocytes, $k_{\infty i}$, must first be calculated:

$$k_{\infty i} = \frac{n_i \pi a^4}{8L^2}(q^2 - 1)[\, q^2 + 1 - \frac{(q^2 - 1)}{\ln q}\,] \qquad \text{Eq. 2-2}$$

where a = the osteocyte process radius, q = the ratio of the radius of the canaliculus, b, to the radius of the osteocytic process ($q = b/a$), L = length of the CPUC, and i = 1, 2, 3 corresponds to the local X, Y, Z lacunar axes (Fig. 2-4), respectively. As developed in Weinbaum et al. (1994), the addition of the fiber matrix that surrounds the osteocyte decreases the permeability $k_{\infty i}$. To calculate the permeability coefficients of a fiber-filled lacunar-canalicular porosity in the three principal directions, k_i, we used the relationship between $k_{\infty i}$ and k_i from Weinbaum et al. (see Fig. 5 of that paper). First the dimensionless length parameter $\alpha = (b - a)/\sqrt{k_p}$ must be calculated, where $(b - a)$ is the fluid annulus surrounding the osteocytic process and $\sqrt{k_p}$ is the thickness of the viscous layer that forms near the canaliculus wall. As demonstrated in Weinbaum et al. (1994), k_p is the small-scale permeability constant for the fluid annulus if it is filled with a fiber matrix; it can be approximated to be $0.0572 a_0^2 (\Delta/a_0)^{2.377}$, where a_0 is the radius of transverse fibers in the annulus surrounding the osteocytic process and Δ is the spacing of the fiber matrix surrounding the osteocytic process.

The length of the cuboidal periodic unit cell (CPUC, Fig. 2-4) surrounding each lacuna was determined from the osteocyte lacunar density data from Remaggi et al. (1998) following the procedure of Cane et al. (1982). The mean surface area of bone

tissue surrounding each lacuna, the two-dimensional osteocyte territory, T, was calculated from the number of lacunae per mm^2 of bone, *N.Lc/B.Ar*, given by Remaggi et al. (1998):

$$T = \frac{1}{N.Lc/B.Ar}. \qquad \text{Eq. 2-3}$$

The CPUC length L was calculated as the square root of the 2-D territory:

$$L = \sqrt{T}. \qquad \text{Eq. 2-4}$$

This was a two-dimensional calculation because only the areal lacunar density was available (number of lacunae per mm^2 of bone). We assume that if a volume measurement were available (number of lacunae per mm^3 of bone) it would yield a similar *L*.

The number of canaliculi crossing each face of the cuboidal periodic unit cell surrounding the lacuna (n_1, n_2 and n_3, where 1, 2, 3 correspond to the local X, Y, Z lacunar directions, respectively) was determined from the number of canaliculi per lacuna (*N.Ca*) estimated with the surface area method, which was used because it lay between the high and low estimates obtained with the slicing method. Based on available cross, longitudino-radial and longitudino-tangential section images from the literature (Marotti, 1979; Marotti, 1995), we assumed that canaliculi run perpendicular to the major axis (the long axis) of the lacuna so that no canaliculi cross the cuboidal periodic unit cell in the direction of the long-axis of the osteocyte (the local Y direction) ($n_2 = 0$) (Fig. 2-5). To determine the number of canaliculi in the X- and Z-directions (n_1 and n_3), we assumed

that the canaliculi were distributed based on the surface geometry of the lacuna as measured by the lacunar projected surface area ratios (Fig. 2-6):

$$n_1 = \tfrac{1}{2}\frac{PSA_{YZ}}{T_{PSA}} * N.Ca, \quad n_3 = \tfrac{1}{2}\frac{PSA_{XY}}{T_{PSA}} * N.Ca \qquad \text{Eq. 2-5}$$

where n_1 and n_3 are the number of canaliculi crossing each face of the cuboidal periodic unit cell perpendicular to the X and Z axis, respectively; PSA_{YZ} and PSA_{XY} are the projected surface areas of the lacunar ellipsoid in the X and Z directions, respectively; T_{PSA} is the sum of PSA_{YZ} and PSA_{XY}; and $N.Ca$ is the total number of canaliculi emanating from a lacuna obtained by the surface area method.

Other microstructural measurements used in determining the local lacunar-canalicular permeability constants were the radius of the osteocytic process, a, (range: 25-205 nm; average 52 nm) and the radius of the canaliculi, b, (range: 40-355 nm; average 129.5 nm), both experimentally measured in mice (You et al., 2004); the radius of transverse fibers in the annulus between the osteocytic process and the canalicular wall, a_0, (range: 0.6-1 nm) (Cowin et al., 1995); and the spacing of the proteoglycan fiber matrix surrounding the osteocytic process, Δ, (range: 6 nm < Δ < 10 nm) (Squire et al., 2001; Wang et al., 2004). The canaliculus annulus, the space between the osteocytic process and the canalicular wall (b - a) was varied to determine the sensitivity of the permeability coefficients to this parameter. A small, medium, and large annulus were used based on the minimum, average, and maximum values for canaliculus radius b and osteocyte process radius a measured by You et al. (2004): a = 25 nm, b = 40 nm (small annulus); a = 52 nm, b = 129.5 nm (medium annulus); and a = 205 nm, b = 355 nm (large annulus). To determine the effects of the radius of the fibers (a_0) on the permeability

coefficients, values of 0.6, 0.7, 0.8, 0.9, and 1.0 nm were used; and to determine the effects of the spacing of the proteoglycan fiber matrix (Δ) values of 7, 8, and 9 nm were used.

2.3 Results

For the total number of canaliculi per osteocyte lacuna ($N.Ca$), the slicing method gave a low and a high bound, while the surface area method estimations lay between these bounds, ranging from 41 for man to 115 for horse (Table 2-1). The mean length L of the CPUC, which is the center-to-center length between lacunae, ranged from 23 to 50 μm in the six species studied by Remaggi et al. (1998) (Table 2-2).

The highest permeability coefficient was found along the minor (Z) axis of the osteocyte lacuna, with the intermediate (X) axis slightly lower. Considering the domains indicated in Figures 2-5b and 2-5c as representative volume elements over which the permeability values were averaged, one can see that the permeability coefficient was zero along the major (Y) axis of lacuna (the long axis of the lacuna) because no canaliculi cross the periodic unit cell boundary in the Y direction. The permeability coefficients were very sensitive to canalicular and osteocytic process dimensions, varying almost three orders of magnitude (from order 1×10^{-22} m^2 to 1×10^{-19} m^2) for the small, medium, and large annulus configurations (Figs. 2-7, 2-8). The permeability coefficients were less sensitive to fiber matrix spacing, demonstrating approximately a 50% increase in permeability for $\Delta = 8$ nm and a 60% increase in permeability for $\Delta = 9$ nm compared to the permeability calculated with $\Delta = 7$ nm (Fig. 2-8). Varying the radius of the fiber

matrix a_0 had little effect on the permeability calculations, resulting in a maximum difference of about 3% in permeability values.

The difference between the two nonzero values of permeability indicated that deviation from transverse isotropy in the three local lacunar directions was present in all species (Table 2-3).

2.4 Discussion

The purpose of this study was to first estimate the number of canaliculi emanating from osteocyte lacunae (*N.Ca*) in different animal species, and then to use the three-dimensional distribution of these canaliculi along with recent measurements of canaliculi and osteocyte process size and fiber matrix estimations to calculate the local permeability coefficients of the lacunar-canalicular porosity in three dimensions. The results provide the most accurate calculation to date of the permeability of the lacunar-canalicular porosity and for the first time the permeability coefficients in three local directions of the osteocyte lacuna are estimated.

The results indicate that *N.Ca* is animal dependent and ranges from 41 to 115 depending on the species (Table 2-1). The values of *N.Ca* reported in this study calculated using the surface area method are similar to the range of values reported in the literature (Atkinson and Hallsworth, 1982). While the surface area method is probably a more precise estimate of *N.Ca*, the slicing method is useful in determining a range of canaliculi that could be supported by a lacuna of a certain volume.

The values of permeability coefficients estimated in this parametric study are of the same order of magnitude as those used in other studies that utilized the isotropic

model of Weinbaum et al. (1994) (Zhang et al., 1998; Wang et al., 1999). The lacunar-canalicular permeability value obtained in the dog femur via a finite element method procedure by Smit et al. (2002), $k = 2.2 \times 10^{-22}$ m^2, falls within the range of permeability values estimated in this study for a small annulus with $\Delta = 7$ nm and $a_0 = 0.6$ nm. Further, to obtain that permeability, the dog lacuna must have approximately 28 canaliculi crossing each face of the cuboidal periodic unit cell along the Z-axis. This number is very similar to the number of canaliculi crossing each face of the cuboidal periodic unit cell along the Z-axis estimated in our study ($n_3 = 27$ canaliculi). Our permeability estimates are several orders of magnitude smaller than those used by Steck et al. (2003), who used permeability values based on work by Dillaman et al. (1991) ($k_{transverse\ to\ bone\ long\ axis} = 1.0 \times 10^{-11}$ m^2 and $k_{parallel\ to\ bone\ long\ axis} = 1.0 \times 10^{-12}$ m^2). The permeabilities reported in Dillaman et al. (1991) as well as the permeabilities from experimental measurements by Rouhana et al. (1981) (~3×10^{-13} m^2) and Li et al. (1987) (~5×10^{-15} m^2) are several orders of magnitude larger than the permeabilities reported in the present study because these previous values represent a lacunar-canalicular porosity and vascular porosity lumped measurement, rather than a lacunar-canalicular porosity measurement alone.

Important parameters that affect the lacunar-canalicular permeability calculation are the canalicular and osteocyte process dimensions, the cuboidal period unit cell length, and the fiber matrix spacing and radius dimensions. The canalicular and osteocyte process dimensions, which determine the annulus through which the interstitial fluid flows (b - a), had the largest effect on the permeability coefficients: permeabilities calculated with the three fluid annulus sizes resulted in values spanning almost three

orders of magnitude for all species (Fig. 2-7). Varying the fiber matrix spacing (Δ) (Fig. 2-8) and the fiber matrix radius (a_0) had a much lower effect on the permeability of the lacunar-canalicular porosity.

Some limitations of this study are that the values used for the canalicular and osteocyte process dimensions were from mice; similar measurements in other species would be more appropriate. Because the canalicular and osteocyte process dimensions have such a large influence on the permeability calculations, to further refine the permeability coefficients it is necessary to more accurately determine the fluid annulus space. Further refinement of the fiber matrix spacing and radius would also improve the permeability calculations. Another limitation is that the cuboidal period unit cell length L was determined from the surface area of bone tissue surrounding each osteocyte lacuna. Volume measurements of bone tissue surrounding each lacuna would be more appropriate to determine this length.

Another limitation of our study is that in accordance with the microstructural model of Weinbaum et al. (1994), we considered the case of straight canalicular channels that pass from one face of the ellipsoidal lacuna directly to the opposing face of the cuboidal period unit cell. Canaliculi were idealized as straight tubes because accurate measurement of the channel contortions is very difficult (Qin et al., 2002). Osteocytic processes exhibit tortuosity (Marotti et al., 1992), traveling between adjacent lacuna and from lacuna to the bone surfaces through winding canaliculi. A few of these canaliculi, specifically the ones originating from the lacuna margins (tip of the major axis of the lacunar ellipsoid), are noted to travel along the major axis of the lacuna for a short distance (Marotti, 1979; Marotti, 1996) and then tend to turn almost perpendicular to that

axis (Fig. 2-5b, 2-5c). This study does not incorporate the effects of canaliculi tortuosity, and it bases the three-dimensional distribution of the canaliculi on the projected surface areas of the lacunar ellipsoid (Fig. 2-6); these limitations could be addressed in the next refinement of the model. In addition, this study has highlighted a need to better evaluate the three-dimensional distribution of canaliculi; thus we are currently using confocal microscopy images to provide such measurements. We do think, however, that accounting for the effects of tortuosity will affect the values reported by a factor that is less than an order of magnitude, perhaps a factor of 3.

Despite the above limitations, the findings of this study demonstrate that osteocyte lacuna shape and size, and the three-dimensional distribution of canaliculi are parameters that determine the degree of anisotropy of the local permeability of the lacunar-canalicular porosity. The findings of this study can be used to build anisotropic poroelastic finite element models that include both the vascular porosity and the local permeability values of the lacunar-canalicular porosity based on the orientation of the osteocyte lacunae in the bone matrix. Because a correlation has been established between the major axis of the osteocyte lacuna ellipsoid and the orientation of the collagen fibers (Marotti, 1996; Ferretti et al., 1999), knowing the collagen orientation would help to incorporate the local permeability estimates determined in this study into finite element models to solve for load-induced pressure and velocity fields in bone subjected to mechanical loading.

	Chick	Rabbit	Cow	Horse	Dog	Man
Low estimate of *N.Ca* using slicing method	18	28	26	42	27	18
High estimate of *N.Ca* using slicing method	104	159	150	252	161	106
N.Ca using surface area method	54	60	85	115	81	41
corresponding number of slices	17	11	17	17	17	11

Table 2-1. *Total number of canaliculi per osteocyte lacuna (N.Ca) estimated using the low and high estimates of the slicing method as well as the surface area method based on data from Remaggi et al. (1998).*

	Chick	Rabbit	Cow	Horse	Dog	Man
L (μm)	23	33	37	31	50	43

Table 2-2. *Mean length L between lacunae (μm) based on data from Remaggi et al. (1998).*

	Chick	Rabbit	Bovine	Horse	Dog	Man
k_1/k_3	5.0/10	3.9/10	3.9/10	3.8/10	5.0/10	5.0/10

Table 2-3. *Ratios of the non-zero permeability coefficients; k_1 and k_3 represent the local permeability coefficients in the X and Z directions, respectively. These are the only two non-zero permeability coefficients because all canaliculi are assumed to cross the cuboidal periodic unit cell along the X and Z axes. $k_2 = 0$ because of the assumption that no canaliculi cross the periodic unit cell in the Y direction (the direction of the long axis of the lacuna).*

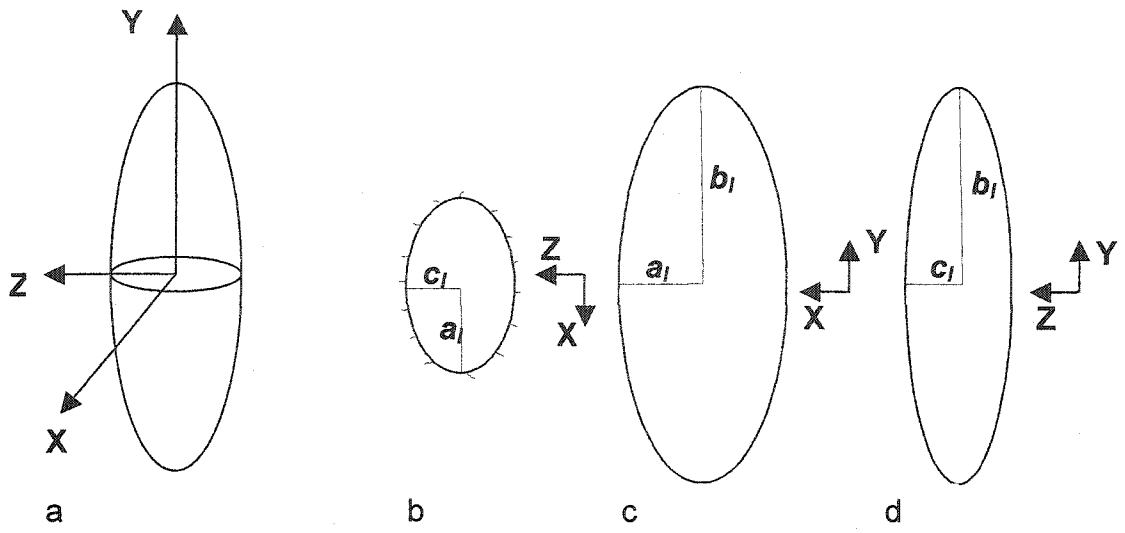

Figure 2-1. *(a) The triaxial ellipsoid used to represent an osteocyte lacuna and the semi-axes a_l, b_l, c_l of the lacuna as reported by Remaggi et al. (1998) in (b) the local X-Z plane, (c) the local X-Y plane, and (d) the local Y-Z plane. The lacunar cross-section where canaliculi distribution was measured in Remaggi et al. (1998) as the number of canaliculi per 10 μm lacunar perimeter length is shown in (b).*

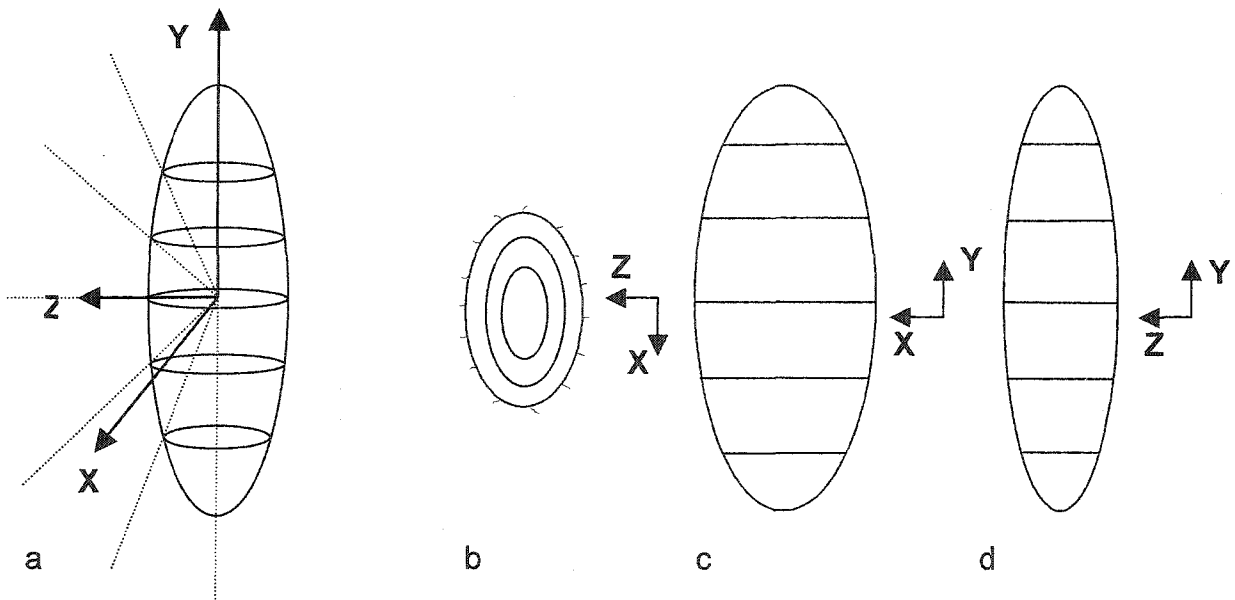

Figure 2-2. *With the slicing method, the osteocyte lacunar ellipsoid is sliced into cross-sectional cuts perpendicular to the long axis of the lacuna (X-Z planar cuts) to estimate the lacunar perimeter length. (a) The case shown represents the low estimate of the lacunar perimeter length (5 slices, cutting angle increment = 30°). The 5 cuts are also illustrated in (b) the X-Z plane, (c) the X-Y plane, and (d) the Y-Z plane.*

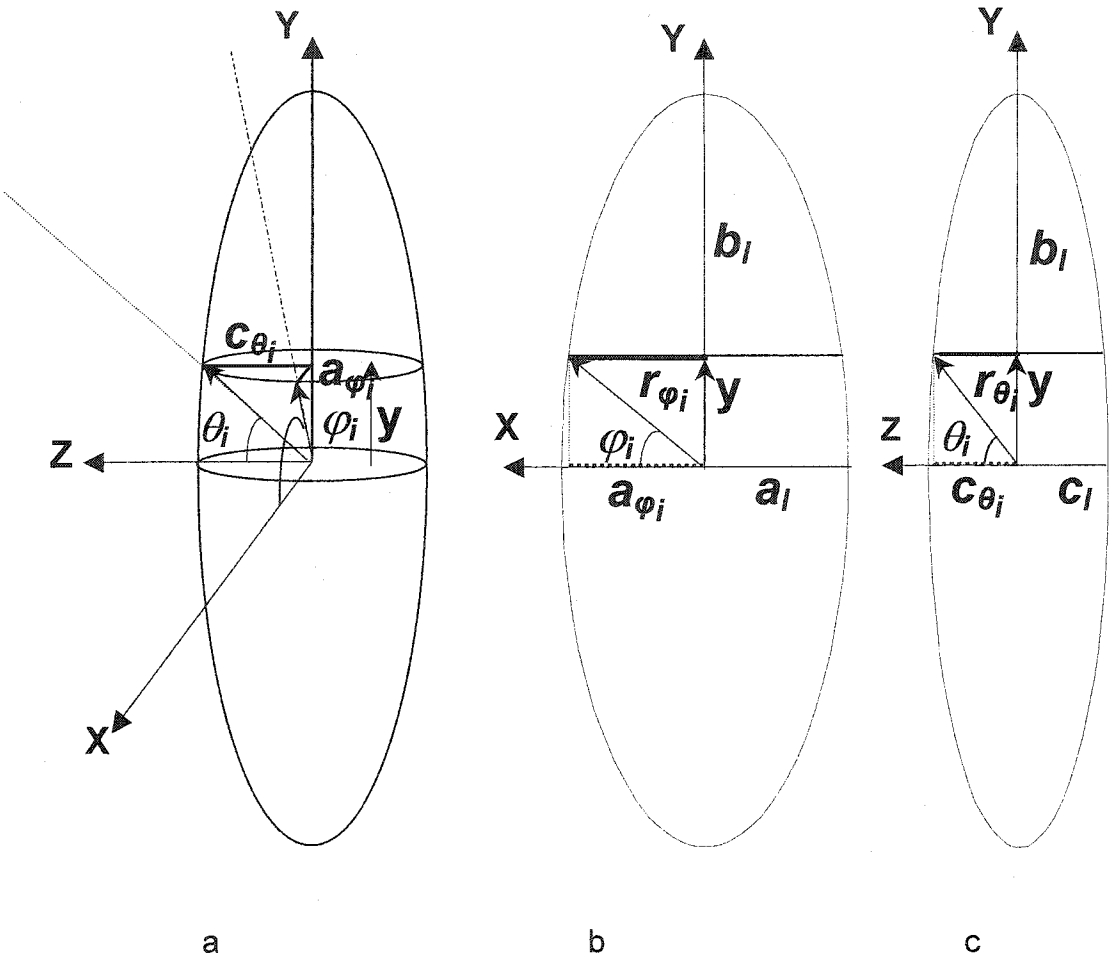

Figure 2-3. *Schematic drawing illustrating the determination of the perimeter length for slices of the osteocyte lacunar ellipsoid. The case shown is for the X-Z plane slices shown in Fig. 2-2. (a) Each cross-sectional cut, obtained as a result of the slicing, is represented by a lacunar ellipse with a new set of semi-axes, a_{φ_i} and c_{θ_i}. For each angle increment φ_i in the X-Y plane along the arc length of the lacunar ellipsoid the radius is* $r_{\varphi_i}^2 = \frac{a_l^2(1-e_l^2)}{1-e_l^2\cos^2(\varphi_i)}$, *where the eccentricity e_l is obtained from* $e_l^2 = 1 - \frac{a_l^2}{b_l^2}$ *and a_l and b_l are the semi-axes of the lacunar ellipse in the X-Y plane shown in (b) (Weisstein, 2004). The angle increment φ_i is known (in this example it is 30°), so r_{φ_i} can be calculated and then the semi-axis a_{φ_i} of the lacunar ellipse at the cross-sectional slice can be calculated: $a_{\varphi_i} = r_{\varphi_i}\cos(\varphi_i)$. To calculate the second semi-axis of the lacunar ellipse at the cross-sectional slice, c_{θ_i}, an additional step must be included because the angle increment θ_i in theY-Z plane is not equal to φ_i. The vertical distance of the cross-sectional slice from the center of the lacunar ellipse, y, must first be calculated: $y^2 = r_{\varphi_i}^2 - a_{\varphi_i}^2$. Then using the geometry in (c) the following equations will yield c_{θ_i}: $r_{\theta_i}^2 =$*

$\frac{c_l^2(1-e_2^2)}{1-e_2^2\cos^2(\theta_i)}$, *where the eccentricity* e_2 *is obtained from* $e_2^2 = 1 - \frac{c_l^2}{b_l^2}$ *and* b_l *and* c_l *are the semi-axes of the lacunar ellipsoid shown in (c);* $c_{\theta_i} = r_{\theta_i}\cos(\theta_i)$; *and* $y^2 = r_{\theta_i}^2 - c_{\theta_i}^2$ *(Weisstein, 2004). After determining the elliptical slice semi-axes* a_{φ_i} *and* $c_{\theta i}$, *the lacunar perimeter length,* Pxz_{φ_i}, *for each slice was estimated based on Euler's ellipse formula:* $Pxz_{\varphi_i} = 2\pi[1/2(a_{\varphi_i}^2 + c_{\theta_i}^2)]^{1/2}$ *(Weisstein, 2004). The total perimeter length for all slices cut in the X-Z plane,* $T_{PL_{XZ}}$ *is then the sum of the lacunar perimeter lengths of each individual slice:* $T_{PL_{XZ}} = \sum_{i=1,n} P_{XZ\varphi_i}$ *where n is the total number of slices.*

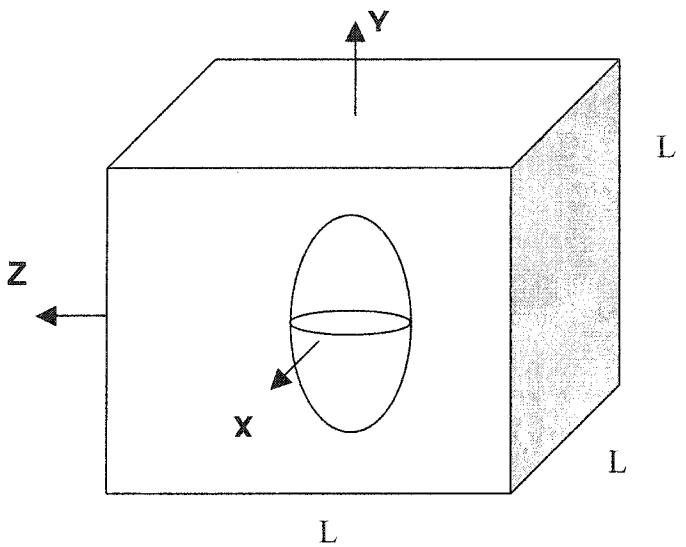

Figure 2-4. *The cuboidal periodic unit cell (CPUC) used to model the osteocyte lacuna and the surrounding canaliculi emanating from it. X is the intermediate axis of the lacuna; Y is the major axis of the lacuna; and Z is the minor axis of the lacuna in the local coordinate system. Canaliculi are not shown for simplification. Not drawn to scale.*

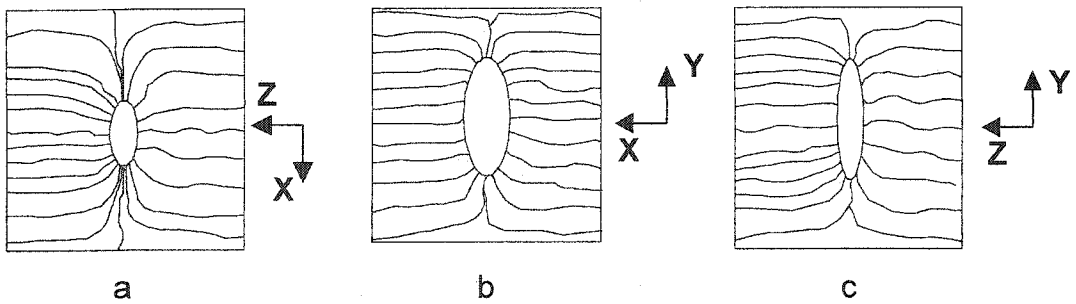

Figure 2-5. *Schematic illustration of canaliculi, which run almost perpendicular to the major axis (Y-axis) of the osteocyte lacuna shown in: (a) the X-Z plane, (b) the X-Y plane, and (c) the Y-Z plane. Not drawn to scale.*

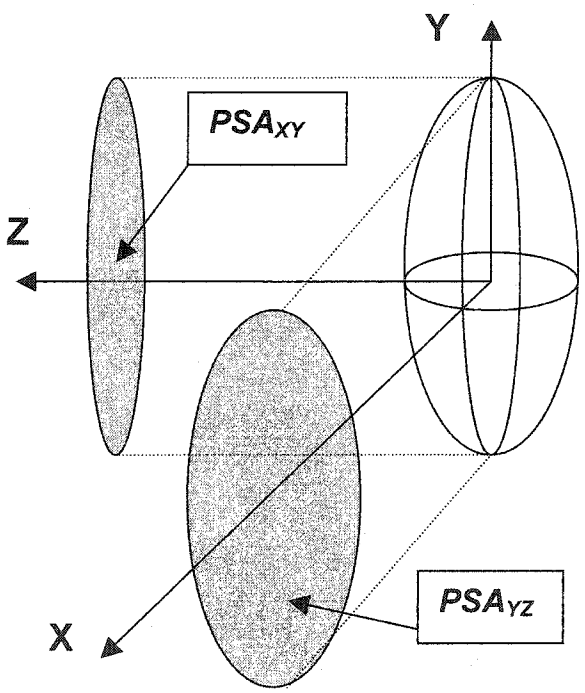

Figure 2-6. *Projected surface areas of the osteocyte lacuna in the local X and Z directions (PSA_{YZ} and PSA_{XY}) were used to determine the distribution of canaliculi.*

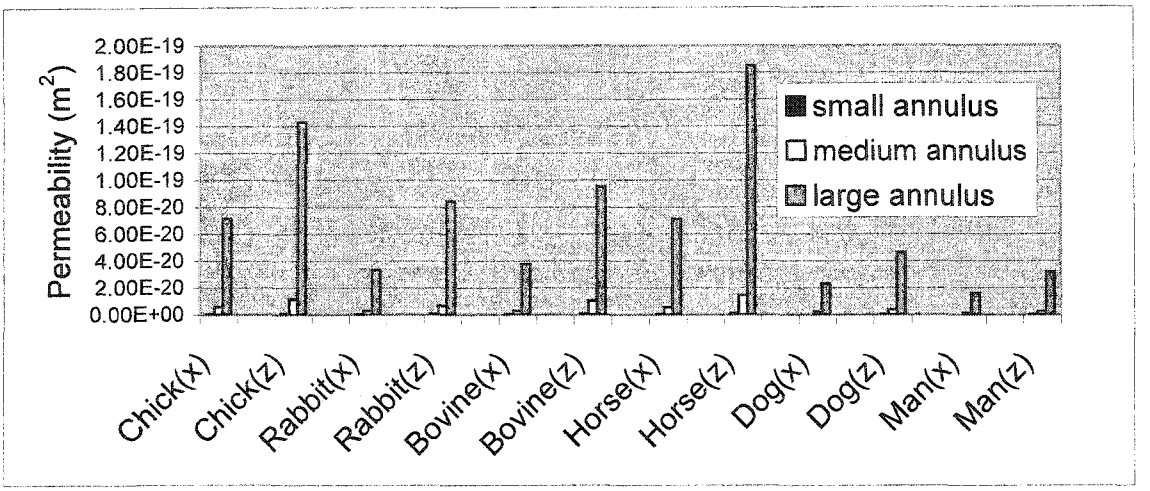

Figure 2-7. *Lacunar-canalicular permeability components shown along the X and Z axes calculated using the surface area method to estimate N.Ca. Small annulus: osteocyte process radius a = 25 nm, canaliculi radius b = 50 nm; medium annulus: a = 52 nm, b = 129.5 nm; large annulus: a = 205 nm, b = 355 nm. Fiber spacing Δ = 7 nm and fiber radius a_0 = 0.6 nm.*

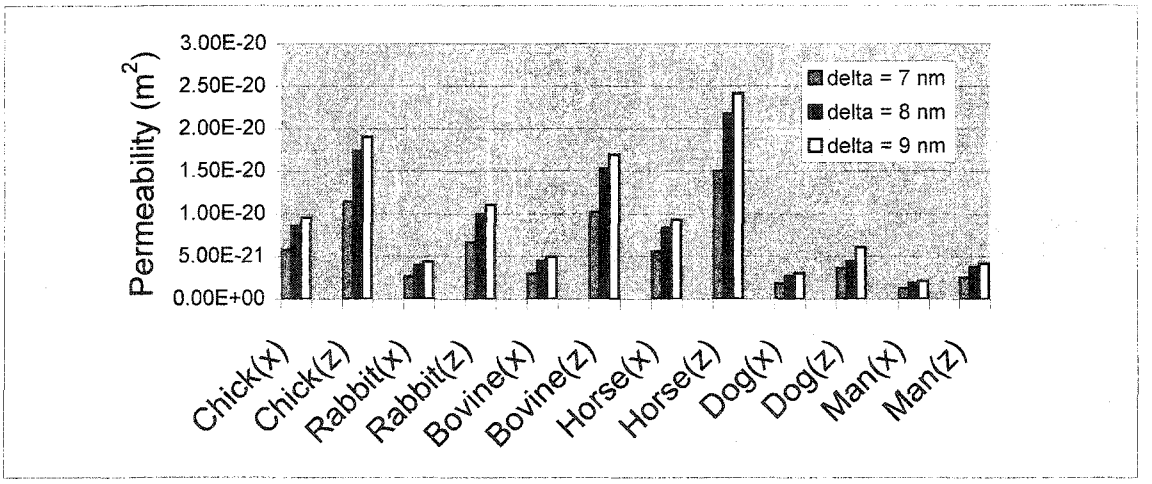

Figure 2-8. *Sensitivity of the permeability coefficients to the fiber spacing (range: Δ = 7 - 9 nm) with a fiber radius of a_0 = 0.6 nm and a medium annulus.*

Chapter 3

3-D Characterization of Osteocyte Lacunae and Canaliculi as Revealed by Confocal Laser Scanning Microscopy

Abstract

For a better understanding of interstitial fluid movement through the bone porosities, it is of first importance to provide a complete three-dimensional characterization of bone's microstructure. In this study, for the first time, confocal microscopy is used to measure volumetric values of osteocyte lacunar density, osteocyte lacunar axis lengths, the number of canaliculi emanating from each lacuna, the canaliculi distribution in three directions, along with the width of the canaliculus annulus. To accomplish this, two different stains were used: basic fuchsin and phalloidin. Basic fuchsin staining was used to make osteocyte lacuna and canaliculi visible, and phalloidin staining was used to make the osteocyte processes visible. In male Sprague Dawley rats, the number of lacunae per unit volume was found to be 80,600/mm^3. This volumetric lacunar density corresponds to a mean volume of 1.24 x 10^{-5} mm^3 of bone matrix associated with an individual osteocyte lacuna, which gives a length of 23.2 ± 0.7 μm for a cuboidal periodic unit cell surrounding the lacuna. The microscopic observations using confocal microscopy as well as the results of the morphometric analysis demonstrate that osteocyte lacunae of male Sprague Dawley rats resemble triaxial ellipsoids with major, intermediate, and minor axes values of 17.6 ± 0.3 μm, 6.1 ± 0.3 μm, and 4.0 ± 0.2 μm, respectively. Our measurements also show that the number of canaliculi emanating per lacuna and the number of canaliculi intersected by all faces of a cuboidal unit cell representing the bone matrix assigned to each individual lacuna is 52.5 and 116, respectively. The number of canaliculi added from branching was found to be approximately 63. Further, our observations revealed that the highest averaged number of canaliculi intersected by the faces of the cuboidal

periodic unit cell was found to be along the minor axis of the triaxial osteocyte lacuna, with the second highest and the lowest along the intermediate and the major axes, respectively. Finally, canaliculi and osteocyte process diameters were found to be 444.8 ± 26.7 nm and 253.4 ± 77.0 nm, respectively, giving an average width of canaliculus annulus of 95.6 nm. The experimental technique used to provide the complete three-dimensional characterization of the osteocyte lacunae and canaliculi will be very useful for accurate quantification of interstitial fluid movement in bone.

3.1 Introduction

Recently the functions of bone mechanosensation and mechanotransduction have been assigned to osteocytes and their cytoplasmic processes. Fluid permeation through the lacunar-canalicular porosity, the porosity that houses the osteocytes and their processes, is believed to be involved in bone's mechanosensory system by shearing osteocyte cell membranes and causing cytoskeleton deformation and thus activating biochemical responses in osteocytes that lead to the process of bone adaptation (Reich et al., 1990; Weinbaum et al., 1994; Cowin, 1995; Klein-Nulend et al., 1995; You et al., 2001). It is hypothesized that the actions of bone remodeling are closely related to the number of osteocytes present (Mullender et al., 1996b). It has also been pointed out that to more accurately quantify bone permeability, it is important to have accurate measurements of osteocyte lacunar density, canalicular annulus width and the three-dimensional distribution of canaliculi (Smit et al., 2002; Beno et al., 2005). Although it is of great concern to provide a more complete characterization of the lacunar-canalicular microstructural parameters, there is currently no systematic three-dimensional analysis of osteocyte lacunae and canaliculi structure in the literature.

While several studies have measured the osteocyte lacunar density per unit area (Cane et al., 1982; Remaggi et al., 1998; Feretti et al., 1999; Vashishth at al., 2000; Wang et al., 2004a), there has been little analysis of lacunar density per unit volume. One exception is the work of Mullender et al. (1996a,b), although their three-dimensional lacunar density values are based on mathematical relationships derived by Sisson and O'Connor (1997) that relate areal lacunar density to volumetric lacunar density. These mathematical relationships assume the osteocyte lacunae to have a perfect ellipsoidal or

spheroidal shape and their validity depends on the knowledge of the shape, size of the osteocyte lacunae and section thickness of the sample. To our knowledge, to date, no one has reported experimentally measured values of the volumetric osteocyte lacunar density, a topic to be addressed here.

Various microscopy techniques such as microradiography, light microscopy and transmission electron microscopy have been previously utilized to quantify the three-dimensional osteocyte lacuna size and shape. These techniques have been used to make two-dimensional measurements of osteocyte lacunar axis lengths and osteocyte sectional area, and then stereology has been used to estimate the lacunar three-dimensional volume (Baud, 1962; Boyde, 1972; Meunier et al., 1973; Meunier et al., 1973; Boyde, 1976; Jowsey et al., 1975). However, for the principles of stereology to be appropriately applied, the three-dimensional ellipsoid osteocyte lacuna orientation must be known with respect to the plane of the histologic section. It has been demonstrated that osteocyte lacunae of the same size may show differences of 55 to 84% between their section areas, depending on how they are sectioned and may show differences of about 24 and 35% between the long and intermediate axes, respectively, if they are sectioned at an angle of 26° from the long axis of the osteocyte lacuna (Marotti, 1981; Marotti et al., 1985). Thus two-dimensional bone sections can easily lead to misinterpretation and misquantification of the microstructural parameters such as lacunar size. To avoid misleading results a method that utilizes transmitted polarized light to first establish correlation between the osteocyte lacunae and collagen fiber orientation has been used so that reliable sectioning of osteocyte lacunae can be performed (Marotti, 1981). This method is helpful especially when applied to bone types such as parallel-fibered and lamellar bone that have a known

collagen fiber orientation relative to the orientation of the major axis of the osteocyte lacuna (Marotti et al., 1996). Although credit goes to this method for establishing the grounds for obtaining more accurate measurements of osteocyte lacuna and also for trying to shed some light on the seriously questioned osteocyte osteolysis (Cane et al., 1982), this method is limited to two-dimensional information and requires assumptions about the shape of the osteocyte lacuna to calculate its volume. Also, application of this method is tedious in that it requires the extra step of collagen fiber orientation assessment, which is a subject of much controversy and different interpretations (Gebhardt, 1906; Smith, 1960; Ascenzi et al., 1965; Frasca et al., 1977; Marotti, 1979; Marotti et al., 1985; Ascenzi and Benvenuti, 1986; Marotti et al., 1996; Giraud-Guille, 1988; Weiner et al., 1997). For example, application of this method is not helpful for woven-fibered bone because it consists of irregularly arranged bundles of collagen fibers with no established correlation between the fibers and the osteocyte lacunae orientation.

Little evidence is available in the literature regarding microstructural bone parameters such as canalicular density and distribution. A few studies have used reflected polarized light and scanning electron microscopy (SEM) to quantify the number of canaliculi departing from the whole outline of the sectional area of the osteocyte lacuna (Marotti, 1995; Remaggi et al., 1998; Ferretti et al., 1999) or the number of canaliculi departing from the vascular wall (the lacunar wall facing the osteonal canal) and from the peripheral wall (the lacunar wall facing the cement line) (Marotti et al., 1985; Remaggi et al., 1998); however, the total number of canaliculi originating from the osteocyte lacuna has not been quantified. The technical difficulties involved with sectioning the same lacuna and then counting the total number of canaliculi emanating

from it is perhaps one of the reasons that this experimental work has not been done to date. In our previous study (Beno et al., 2005), we estimated the total number of canaliculi emanating per lacuna along with the three-dimensional distribution of the canaliculi based on two-dimensional information. Measuring the canalicular distribution will be addressed here.

A powerful practical alternative to conventional light microscopy and SEM is confocal laser scanning microscopy (CLSM). CLSM permits "optical sectioning" through opaque materials, which generates excellent three-dimensional images and provides very good details of bone microstructure. CLSM has been validated on cortical bone specimens by correlating the morphology of identical areas with conventional light microscopy (Grotz et al., 1999). Recent application of CLSM has proven to be a very useful technique in determining accurate measurements of osteocyte lacuna size and shape (McCreadie et al., 2003) not only because it is a three-dimensional technique but also because it does not require assumptions to be made regarding the shape of the osteocyte lacuna. In addition, in CLSM osteocyte lacunae and canaliculi can be seen with high contrast (Wang et al., 2004b). Further, CLSM can be applied to all types of bone regardless of the collagen fiber orientation because it does not call for that assessment and avoids it all together. Therefore, for the above stated reasons, in this study we utilized CLSM to measure a) the areal and volumetric osteocyte lacunar density; b) the osteocyte lacuna axis lengths; c) the number of canaliculi emanating from each osteocyte lacuna; d) the canalicular distribution in three-dimensions; and e) the canaliculus annulus width. This study was designed to extract these microstructural bone parameters directly from stacks of slice images and not from two-dimensional images, as

has been the practice in the past. These measurements will assist in calculating the most accurate local permeability coefficients in the lacunar-canalicular porosity, which is important in providing a complete material property dataset to build accurate poroelastic finite element (FE) models. These FE models can solve for load-induced pressure and velocity fields without having to make any simplifications or justifications due to the lack of this information.

3.2 Materials and Methods

Bone section preparation

Bone samples were taken from the left tibia of ten- to eleven-week-old male Sprague Dawley rats (n = 6, 300-320g). Cortical bone was cut from the mid-diaphysis in 4-mm blocks (Fig. 3-1) and placed immediately in 10% formalin for 24 hours. After fixation, the blocks were rinsed in running water overnight and then either basic fuchsin staining (protocol provided by Mitchell B. Schaffler, Ph.D., Mount Sinai School of Medicine, New York, see Appendix) or phalloidin staining was performed. The basic fuchsin stained blocks were first embedded in PMMA and then thin sections (0.3-0.4 mm thick) were cut using a diamond blade saw (Buehler, Lake Bluff, IL). The phalloidin stained blocks were stained with phalloidin (Molecular Probes, Eugene, OR) for one hour and then were cut into thin cross-sections 0.3-0.4 mm thick without undergoing the embedding process. Then, all sections were ground down to approximately 100-μm thick using decreasing Carbimet paper discs (800-1200 grit; Buehler, Lake Bluff, IL). Longitudino-radial, cross-sectional (transverse), and longitudino-tangential sections of

approximately 100-μm thick were obtained from the basic fuchsin blocks and cross-sectional (transverse) sections were obtained from the phalloidin stained blocks. While the purpose of the basic fuchsin staining was to penetrate and to make osteocyte lacunae and canaliculi visible, the phalloidin stain makes actin filaments visible and thus makes the osteocyte body and its processes visible since they contain actin (Tanaka-Kamioka et al., 1998).

3D confocal laser scanning microscopy measurements

The sections were viewed, scanned, and analyzed under 3-D confocal microscopy (Zeiss LSM 510) by one investigator. For consistency and due to the relatively large sectional area of the samples, all measurements were performed at the anterior corner-sampling region for all samples (Fig. 3-1). We measured several microstructural parameters of the lacunar-canalicular porosity using the following protocols:

1. Measurement of osteocyte lacunar density and length of cuboidal unit cell of bone matrix surrounding the osteocyte lacuna: For each animal confocal scans of the sampling region were performed using a 63x objective lens, and a z-stack (3-D reconstruction of the collection of the scanned images at different focal depths) was obtained (volume scanned was ~ 538,871 μm^3). Then, the osteocyte lacunae were point counted directly from the z-stack (Fig. 3-2) and the volumetric lacunar density (number of lacunae per bone volume, *N.Lc/B.V*) was determined for each sample. The following criterion was used for counting the osteocyte lacunae: all lacunae were accounted for, including any partially sectioned lacunae at the top surface of the z-stack but excluding any lacunae partially sectioned by the bottom surface. To determine the areal lacunar

density (number of lacunae per bone area, *N.Lc/B.Ar*), all the partially sectioned lacunae at the top surface of the z-stack were point counted from the z-stack file.

The size of the cuboidal periodic unit cell (CPUC, Fig. 3-3), which is a measure of the average volume of bone matrix surrounding each lacuna, was determined from the osteocyte lacunar density data obtained in our study following the procedure of Cane et al. (1982). The mean volumetric bone matrix territory surrounding a lacuna, the three-dimensional osteocyte territory, *T*, was calculated from the number of lacunae per mm^3 of bone, *N.Lc/B.V*:

$$T = \frac{1}{N.Lc/B.V}. \qquad \text{Eq. 3-1}$$

The CPUC length *L* is then calculated as the cubic root of the 3-D territory:

$$L = \sqrt[3]{T}. \qquad \text{Eq. 3-2}$$

In contrast to all previous studies where two-dimensional calculations were possible (Beno et al., 2005) because only the number of lacunae per mm^2 of bone were available (Remaggi et al., 1998; Ferretti et al., 1999), this is a three-dimensional calculation because volume measurements were performed (number of lacunae per mm^3 of bone).

For both the osteocyte lacunar density and the length of the cuboidal periodic unit cell, the mean ± SD was calculated for the six animals.

2. Measurement of osteocyte lacunar axis lengths: Confocal scans were performed using a 543 nm wavelength with 20% adjusted laser line intensity from an HeNe1 laser with a 63x oil immersion lens, and using a pinhole set to 1 Airy unit. Z-

stacks were obtained for all lacunae. Only lacunae that were not missing any portion of their volume were considered. Our job was simplified by the fact that the long axis of most of the lacunae was parallel to the long axis of the tibia, so that z-stacks taken from transverse sections could easily be used to estimate the lengths of the lacunar axes. Looking through the z-stack slices (x-y-slices -- the gallery file) at different depths allowed us to pick the greatest x and y pair in the x-y slices and looking through their 3-D projection (z-stack file) allowed us to measure the distance between the top and the bottom tips of the lacuna. The greatest x and y pair from the x-y slices were chosen to represent the minor and the intermediate measured lengths of the osteocyte lacuna axes and the distance between the top and the bottom tips of the lacuna was chosen to represent the measured length of the major axis of the osteocyte lacuna. Measurements for the osteocyte lacuna lengths from the gallery file and the projection file were performed on 4 lacunae from each animal (24 total lacunar measurements), and the mean ± SD lengths for the three lacunar axes were determined. To match the notation from our previous theoretical work (Beno et al., 2005), the major lacunar axis was taken as the 2-direction, with the intermediate axis as the 1-direction, and the minor axis as the 3-direction (Fig. 3-3).

3. Measurement of number of canaliculi emanating from each lacuna (N.Ca):

N.Ca is defined here as first order canaliculi and accounts for the canaliculi originating from the lacuna margins (tip of the major axis of the lacunar ellipsoid) as individual canaliculi rather than a single canaliculus of a large diameter that branches in the immediate vicinity of the lacunar wall (Pawlicki, 1974, 1975; Johnson and Highinson, 1983). To count the *N.Ca* emanating per osteocyte lacuna we performed confocal scans

of very small volume (~1,080 μm^3) that included the entire osteocyte lacuna. These scans were performed on transverse and longitudinal sections and were obtained using a Plan-Apochromat 63x/1.4 Oil DIC HeNe1 objective lens with a light path of LP 650 nm at 20% adjusted laser line intensity and a pinhole size set to the optimal interval (resulting in a 0.37 μm optimal slice). To produce images that exhibited no red (over-saturated) or blue (under-saturated) pixels, the detector gain and the amplifier offset were set to 724 and 0.084, respectively; and since the signal was very strong to avoid amplifying the noise along with the signal, the amplifier gain was kept at 1. To facilitate counting of the *N.Ca* emanating per lacuna a sequence of projections was computed by the Zeiss LSM 510 software, with the z-stack being rotated by 5.625° (64 projections over 360°) from image to image, thus enabling very accurate counts of these canaliculi. Canaliculi emanating per osteocyte lacuna were point counted directly from the longitudinal-radial and longitudinal-tangential stacks (Fig. 3-4) on 8 lacunae from each animal (48 total measurements) and the mean ± SD was determined for the six animals.

4. Measurement of the 3-D distribution of canaliculi (n_i): A measurement necessary for the microstructural model we have previously used to calculate the permeability of the lacunar-canalicular porosity (Beno et al., 2005) is the distribution of canaliculi in three directions, specifically the number of canaliculi penetrating the six faces of the cuboidal periodic unit cell (CPUC, Fig. 3-3). To count the number of canaliculi penetrating each face of the CPUC confocal scans of an osteocyte lacuna and its surrounding territory were performed and z-stacks of side length L were reconstructed (Fig. 3-5). The scanned volume or z-stack represented the CPUC employed in our previous study (Beno et al., 2005). The side length of the scanned volume, which was

calculated from the volumetric lacunar density as described above, was found to be L = 23.2 μm (volume of scan was approximately 12,487 μm^3). These scans were performed using the same magnification and settings used in the previous section, and every effort was made to locate the osteocyte lacuna at the center of the scanned volume. To avoid any ambiguity in counting due to canalicular branching, change of canalicular direction, as well as the lower resolution in the in-depth direction of the sample (a limitation of CLSM), counts of canaliculi intersected by each face of the CPUC were made inside squares of side length L = 23.2 μm that represented the six faces of the CPUC and were located at the edges of the CPUC (Fig. 3-6). To facilitate the counting, as in the previous section, a sequence of projections was computed with the z-stack rotated by 5.625° from image to image, by full turn about the vertical axis, thus enabling accurate counts of canaliculi intersected by each face of the CPUC (Fig. 3-6A). Since full rotation about the vertical axis allows for counts only at four faces of the CPUC (faces parallel to the axis of rotation), a second confocal scan on the same CPUC, a 90° z-stack scan relative to the first one, was performed (Fig. 3-6B). This provided exposure of the remaining two faces of the CPUC and permitted counts of the canaliculi crossing these two faces, thus enabling counts of canaliculi intersected by all faces of the CPUC. The average number of canaliculi penetrating each face in the three-principal directions of the CPUC were determined (n_1, n_2 and n_3, where 1, 2, and 3 correspond to the osteocyte lacuna axes and the principal directions of the CPUC). Then the mean ± SD of n_1, n_2, and n_3 was calculated for six lacunae (one from each animal).

5. Measurement of osteocyte canaliculus annulus width: The canaliculus annulus is the space between the canaliculus wall and the osteocytic process. To obtain the width

of the canaliculus annulus we measured the canaliculus and osteocyte process diameters. Measurements were performed directly from the gallery files of the scanned confocal images. All scans were performed using the same magnification and settings used to measure the number of canaliculi emanating from each lacuna and crossing the faces of the cuboidal cell as described above. We assumed the phalloidin and the basic fuchsin stains outline the outermost boundaries of the osteocytic processes and canaliculi, respectively. The canaliculus diameter was measured for 10 canaliculi per animal (a total of 60 measurements), while for the osteocyte process diameter 42 measurements were taken. The mean diameters were calculated and then the mean osteocyte process radius was subtracted from the mean canaliculus radius to obtain the average canaliculus annulus width.

3.3 Results

Confocal images of high magnification (63x) revealed that osteocyte lacunae and interconnecting canaliculi could be highly visualized in the mid-diaphysis of the rat tibia (Fig. 3-2). In the fully mineralized bone sections basic fuchsin provided sufficient intensity for up to 50 μm depth of sequential imaging for the osteocyte lacunae scans and up to 35 μm depth for the canaliculi scans, which required more detail. The mean ± SD volumetric and areal lacunar densities measured in this study were found to be 80,600 ± 7,980/mm^3 and 1,200 ± 74.0/mm^2, respectively. The volumetric lacunar density corresponds to a mean volume of 1.24 x 10^{-5} mm^3 mean volume of bone matrix associated with an individual osteocyte lacuna, which gives a length of 23.2 ± 0.7 μm for

the cuboidal periodic unit cell. Our microscopic observation under CLSM as well as the results of the morphometric analysis demonstrate that osteocyte lacunae of male Sprague Dawley rats resemble triaxial ellipsoids with major (2), intermediate (1), and minor (3) axes values of 17.6 ± 0.3 μm, 6.1 ± 0.3 μm, 4.0 ± 0.2 μm, respectively.

The number of canaliculi directly emanating from each lacuna (*N.Ca*) was found to be 52.5 ± 2.2. We have termed these canaliculi first order canaliculi; whereas we have termed the canaliculi that penetrate the six faces of the cuboidal periodic unit cell second order canaliculi, which were measured to be 116 per lacuna. Second order canaliculi include both first order canaliculi plus any canaliculi added by branching between the lacuna and the face of the unit cell. The number of canaliculi added from branching can be determined by the difference between the number of second and first order canaliculi, and was calculated to be 63.5 for the rat bone.

For the canalicular distribution in three directions, the highest number of canaliculi penetrating each face of the cuboidal periodic unit cell was found to be along the minor axis (3-axis) of the osteocyte lacuna, with the second highest running along the 1-axis (the intermediate axis), and the lowest running along the major or long axis (2-axis) of the lacuna (Table 3-1). This finding indicates that orthotropy is the local symmetry possessed by the osteocyte canaliculi of rat tibial cortical bone. The degree of orthotropy is given by the canaliculi ratios (Table 3-1).

Canaliculi and osteocyte processes diameters were found to be 445 ± 26.7 nm and 253 ± 77.0 nm, respectively. From these data, the average width of the canaliculus annulus is 96 nm.

3.4 Discussion

The purpose of this study was to measure microstructural bone parameters including volumetric osteocyte lacunar density, triaxial ellipsoid lacuna axis lengths, the number of canaliculi emanating from an osteocyte lacuna, the distribution of canaliculi in three-directions, and the width of the osteocyte pericellular annulus. The protocols developed here using confocal microscopy provide a systematic three-dimensional analysis of osteocyte lacunae and canaliculi that for the first time extracts these parameters directly from volumetric measurements.

The measured areal osteocyte lacunar density (1,200/mm^2) is very similar to the osteocyte density reported by Li et al. (1991) (1,020/mm^2) and the osteocyte lacunar density reported by Wang et al. (2004a) (1,248/mm^2) for the same species and approximately from the same bone location. Our experimentally measured value of the volumetric osteocyte lacunar density *(N.Lc/B.V)* is about 14% less than the mathematically calculated *N.Lc/B.V* value reported in Mullender et al. (1996b) (93,200/mm^3). Although a direct comparison between these two volumetric values would not be appropriate because they reflect the *N.Lc/B.V* from different bone locations, this finding is consistent with the Cane et al. (1982) finding that the lacunar density is higher in bone locations with a higher turnover rate (rat femoral head used in Mullender et al. (1996b)) than in bone locations with a lower turnover rate (rat tibia used in this study). The mean length of the periodic unit cell calculated here (23.2 μm) is similar to the range of the values reported previously for other species (Beno et al., 2005).

The mean lengths of the three principal axes of the ellipsoidal osteocyte lacuna measured (6.1 μm, 4.0 μm, and 17.6 μm) are similar to the range of values reported in the

literature for different animals (Marotti, 1981; Remaggi et al., 1998; and Ferretti et al., 1999) and compare most closely to the values reported for chick (10 μm, 4 μm and 20 μm) (Remaggi et al., 1998).

The results indicate that the number of canaliculi emanating from each osteocyte lacuna (*N.Ca)* measured in this study (~53 canaliculi) falls within the range of the reported values in the literature (Atkinson and Hallsworth, 1982; Beno et al., 2005) and compares most closely to the *N.Ca* emanating from chick lacunae calculated in our previous study. This finding is in consistent with the finding that the *N.Ca* is directly related to the size of the osteocyte lacuna (Marotti et al., 1995; Beno et al., 2005).

The degree of orthotropy of the second order canaliculi we found (Table 3-1) is somewhat different from the degree of orthotropy of the canaliculi calculated in our previous study. However, the ratios reported previously (Beno et al., 2005) pertain to first order canaliculi ratios rather then the second order ratios reported here. The high number of branching of the first order canaliculi and the high number of osteocyte processes joining adjacent osteocyte processes at right angles observed previously (Johnson and Highison, 1981) and evident in this study (Fig. 3-7) are the reasons for these differences in the degree of orthotropy.

The average width of the canaliculus annulus (~95 nm) is similar to the average width of the pericellular annulus reported in the literature for BalB/cByJ female mice (~78 nm, You et al., 2004). This pericellular annulus is an important parameter that contributes to the permeability of the lacunar-canalicular porosity.

A limitation of this study relates to making actual length measurements (the lacunar axis lengths, the osteocyte process width, and the canalicular annulus width). It

was assumed that the phalloidin and the basic fuchsin stains outline the outermost boundaries of the osteocyte processes and canaliculi, respectively. Evidence to confirm the above assumption has yet to be found. Also, the choice of settings used in confocal laser scanning microscopy for the detector gain, the amplifier offset, and the amplifier gain has a slight effect on the size of canaliculi, osteocytic process, and lacunar axis length measurements. Quantification of this effect, by setting these parameters to their maximum and minimum positions respectively, remains to be done. However, since the settings used for both staining sets were the same and since the difference between the canaliculus radius and osteocytic process radius gives the value of the canaliculus annulus, one would conclude that our measured value for the canaliculus annulus size is not affected by the choice of the settings used and therefore is an accurate measurement. We must add that the settings chosen produced the best sets of confocal laser scanning microscopy images. To obtain very accurate measurements for canaliculi and osteocytic process dimensions via confocal laser scanning microscopy, correlation of the morphology of identical areas with objects of known size must be performed first.

Also, due to the high cost of confocal scanning only observed values on 6 lacunae for the canaliculi distributions in three directions are reported. Further quantification of these values awaits future studies.

Despite the above limitations, the findings of this study provide three-dimensional microstructural bone parameters that can be used to calculate the accurate local permeability coefficients of the lacunar-canalicular porosity. Determination of the total number of canaliculi supported by each lacuna is critical to better understand the involvement of interstitial fluid flow in bone's mechanotransduction mechanism and

osteocyte nutrition. The findings of this study can also be used to provide the orthotropic material dataset that can be used to build anisotropic poroelastic finite element models that can solve for load-induced pressure and velocity fields in cortical bone.

n_2	n_1	n_3	$\frac{n_2}{n_1}$	$\frac{n_1}{n_3}$	$\frac{n_2}{n_3}$
13.3 ± 2.7	16.7 ± 2.1	27.8 ± 3.3	$\frac{8}{10}$	$\frac{6}{10}$	$\frac{5}{10}$

Table 3-1. *Mean ± SD number of the canaliculi penetrating each face of the CPUC perpendicular to the osteocyte lacuna axes and their ratios, respectively.*

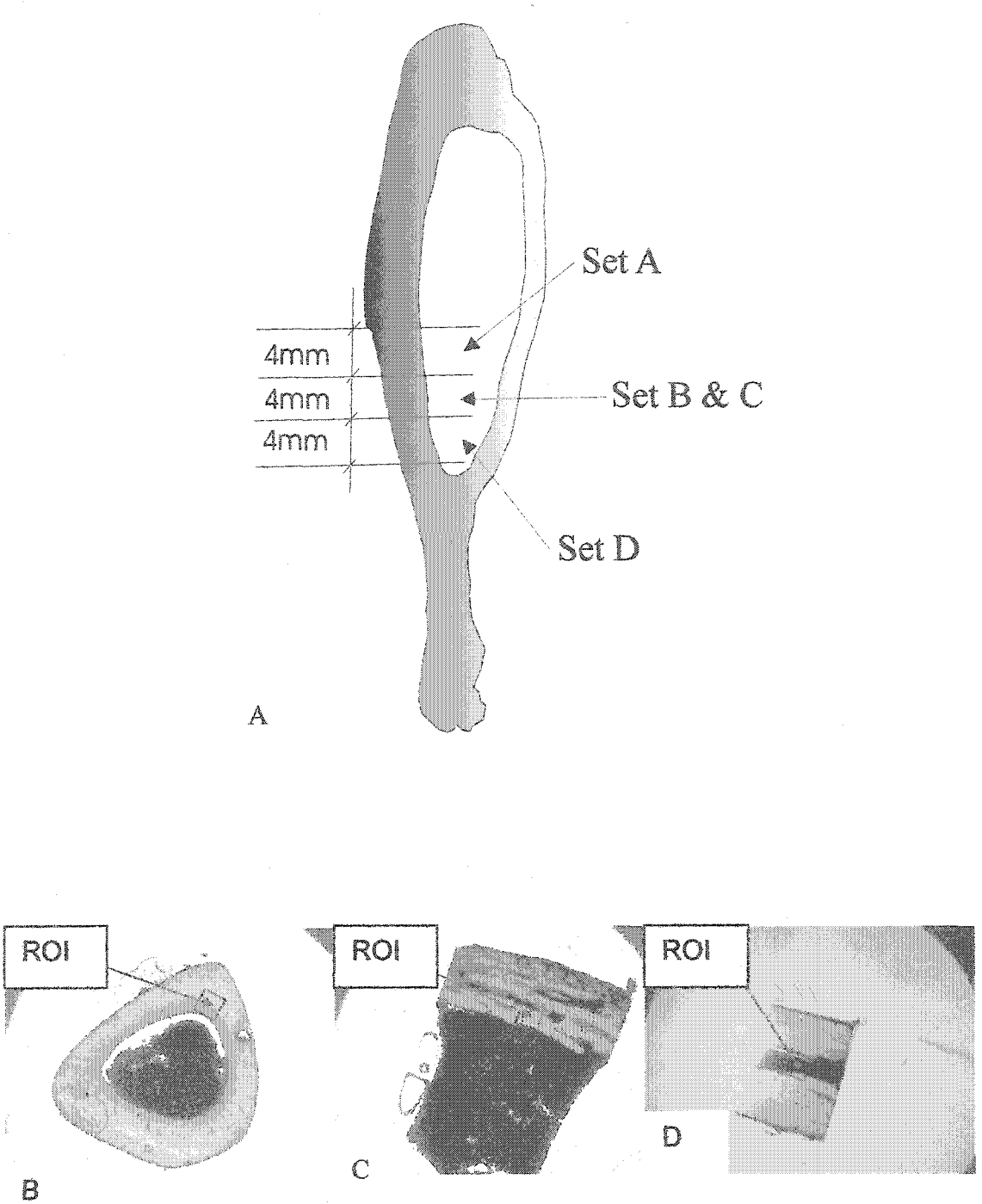

Figure 3-1. (A) Bone sections were taken from the tibia mid-diaphysis. While Set A and Set B & C were stained with basic fuchsin, Set D was stained with phalloidin. Location of the region of interest where confocal images were taken in the: (B) cross-sectional (transverse) plane, (C) longitudinal-radial plane, and (D) longitudinal-tangential plane.

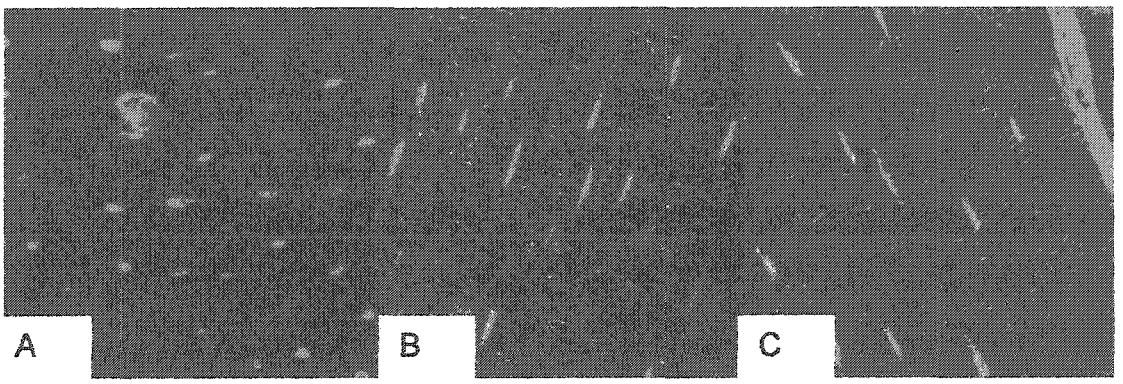

Figure 3-2. Confocal images (63x oil) showing the lacunar-canalicular network in: cross-sectional plane (A), in longitudinal-radial plane (B), and in longitudinal-tangential plane (C). Edge length is 146.2 μm.

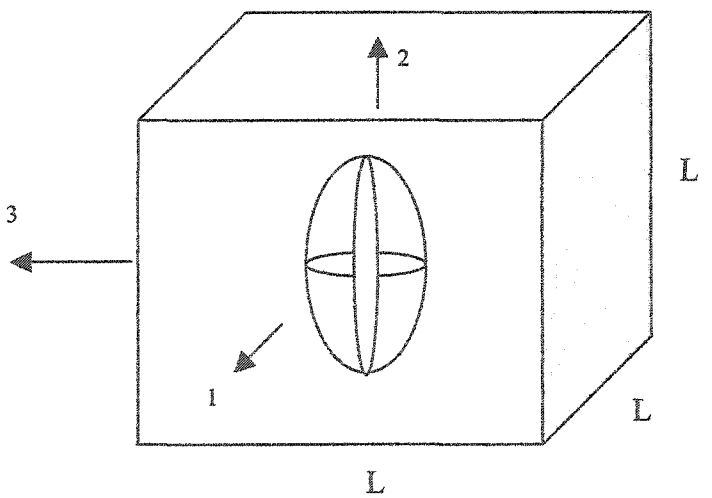

Figure 3-3. The cuboidal periodic unit cell (CPUC) used to represent the mean volumetric bone matrix territory associated with each individual lacuna. 1 is the intermediate axis, 2 is the major axis, and 3 is the minor axis of the osteocyte lacuna. Not drawn to scale.

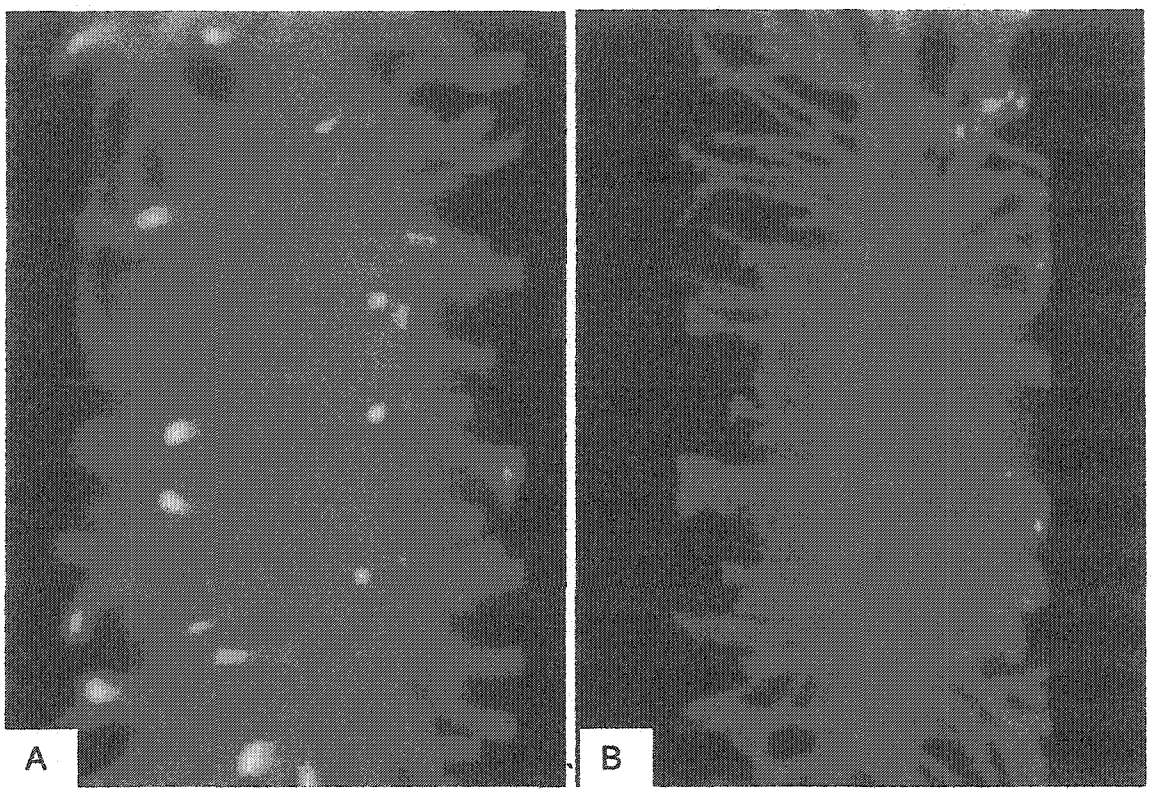

Figure 3-4. *Confocal scans (63x oil) showing a stained osteocyte lacuna and its canaliculi departing from the lacuna body in: (A) longitudinal-radial, and (B) longitudinal-tangential sections.*

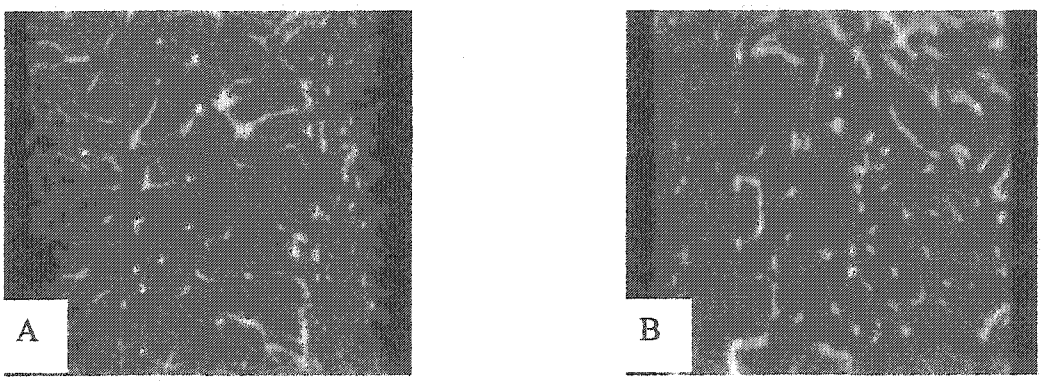

Figure 3-5. *Confocal scans (63x oil) of the cuboidal periodic unit cell (CPUC) (side length ~ 23.2 μm) with the osteocyte lacuna located at the center and its canaliculi intersected by the CPUC faces. In (A), the major axis of the osteocyte lacuna is in the vertical direction; and in (B), the major axis of the osteocyte lacuna is in the horizontal direction.*

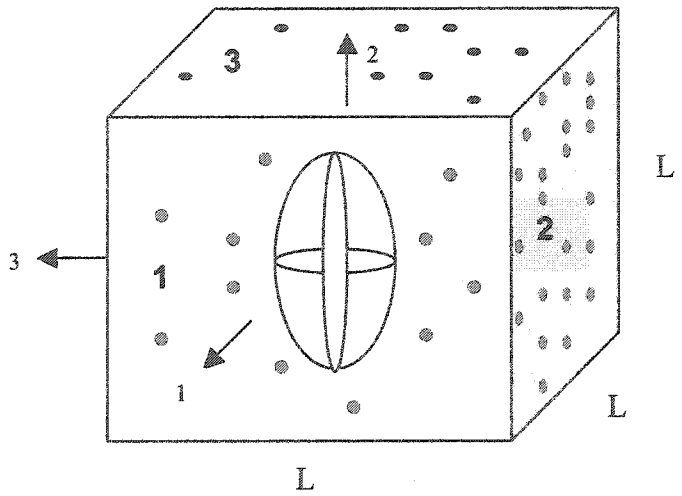

Figure 3-6. *Schematic drawing illustrating the technical procedure used to determine the local canalicular distribution in three-dimensions. Black (on faces 3 and 6), blue (on faces 1 and 4) and red (on faces 2 and 5) dots represent the number of canaliculi intersected by each face of the cuboidal periodic unit cell (CPUC) along the major, intermediate, and minor axes of the triaxial ellipsoidal osteocyte lacuna, respectively. Notation: The intermediate axis of the osteocyte lacuna intersects Faces 1 and 4, the minor axis intersects faces 2 and 5, and the major axis intersects faces 3 and 6 of the CPUC. Faces 4, 5 and 6 are not shown in the schematic drawing. Not drawn to scale.*

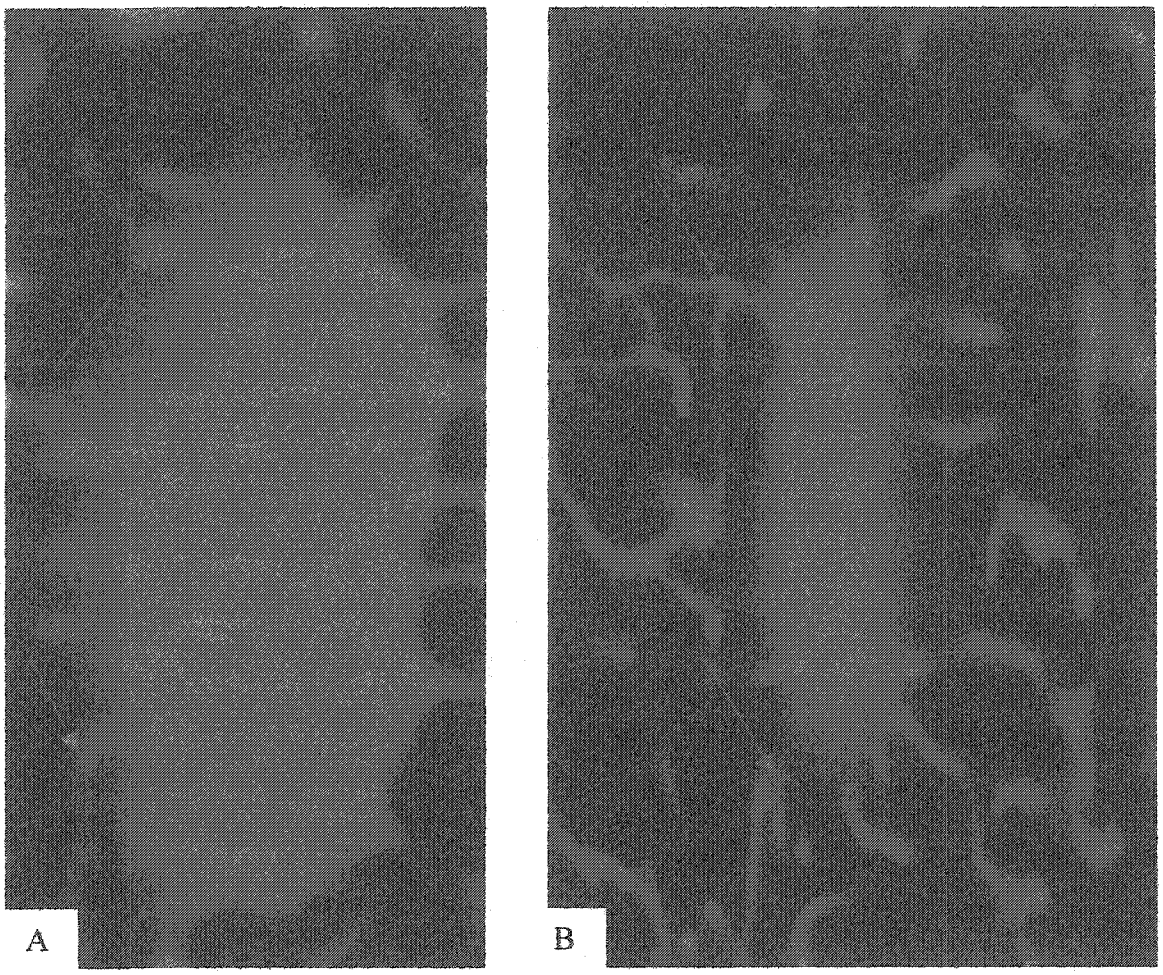

Figure 3-7. *(A) Arrows indicate canaliculi originating from the osteocyte lacuna (not from the lacuna apices) and changing their course of direction at right angles (90° or nearly 90° angles). (B) Arrows indicate branching of canaliculi.*

Appendix

PROCESSING PLASTIC SECTIONS

I. Gross-Dissection of Bones and place in formalin
II. Change solution to 70% Ethanol
III. Bulk Staining
  A. 1% Basic Fuchsin Stock
    i. 10 grams of Basic Fuchsin
    ii. 1000 mls of 100% Ethanol
      1. 80% Basic Fuchsin (80 mls from Basic Fuchsin Stock +20 mls of Distilled H20)
      2. 90% Basic Fuchsin (90 mls from Basic Fuchsin Stock + 10 mls of Distilled H20)
      3. 100% Basic Fuchsin (100% or 100 mls from Basic Stock)

        a. 1% Basic Fuchsin in 80% ETOH for 48 hours at 22C
        b. 1% Basic Fuchsin in 80% ETOH for 48 hours at 22C
        c. 1% Basic Fuchsin in 90% ETOH for 48 hours at 22C
        d. 1% Basic Fuchsin in 90% ETOH for 48 hours at 22C
        e. 1% Basic Fuchsin in 100% ETOH for 48 hours at 22C
        f. 1% Basic Fuchsin in 100% ETOH for 48 hours at 22C

IV. Rinse in 100% Ethanol and leave specimen in 100% ETOH for 1 hours to remove excess stain.
V. Change solution to Petroleum Ether. Two (2) changes within a 24 hour period
VI. Infiltration (Soft Methacrylate Preparation for cross-sections)
  A. Infiltration Solution I **(Stir~45 minutes)** 2 days for mouse bone
    i. Methyl Methacrylate
      1. 765.0 mls
    ii. Dibutyl Phthalate
      1. 135.0 mls

  Waste into container near the grinder.

  B. Infiltration Solution II **(Stir~3 hours)** (Freezer) 2 days for mouse bone
    i. Methyl Methacrylate
      1. 765.0 mls
    ii. Dibutyl Phthalate
      1. 135.0. mls
    iii. Benzoyl Peroxide*
      1. 8.75 grams

  Waste into HDPE container and put on top of vacuum in the hood.

C. Infiltration Solution III **(Stir~3 hours)** (Freezer) 2 days for mouse bone
   i. Methyl Methacrylate
      1. 765.0 mls
   ii. Dibutyl Phthalate
      1. 135.0 mls
   iii. Benzoyl Peroxide*
      1. 17.5 grams

Waste into HDPE container and put on top of vacuum in the hood.

D. Embedding Solution** **(Stir~3 hours)** (Freezer)
   i. Methyl Methacrylate
      1. 765.0 mls
   ii. Dibutyl Phthalate
      1. 135.0 mls
   iii. Benzoyl Peroxide*
      17.5 grams

Note: *Benzoyl Peroxide should be place in the oven at (37-40) C until dry (~2-3 hrs). Ready to use when dry.

Note: **Embedding Solution should stir continuously for ~ 2-3 hours. Place in sunlight of leave at room temperature; shake occasionally until solutions show signs of polymerization (about the thickness of honey). Store in freezer. Stable for several months at –20C.

Chapter 4

Finite Element Modeling Considerations For Future Work

4.1 Introduction

Several studies have used poroelastic finite element models to analyze the response of cortical bone to mechanical loading (e.g., Qin, 1997; Manfredini et al., 1999; Smit et al., 2002; Steck et al., 2003). Except for Smit et al. (2002), the models lump the vascular porosity and the lacunar-canalicular porosity together even though their permeabilities differ by several orders of magnitude. Also, except for the model of Steck et al. (2003) the models assume the bone permeabilities to be isotropic, probably due to the fact that there is no complete anisotropic poroelastic parameter dataset for the bone permeabilities. How the local orthotropic permeability symmetry findings found in this work would be incorporated into finite element models of human osteonal bone and whole rat tibia bone to solve for load-induced pore pressure and velocity fields in cortical bone is the topic to be addressed here. These finite element models would enable us for the first time to determine the most accurate pore pressure and velocity fields in the lacunar-canalicular network of complex anatomical bone geometries undergoing mechanical loading. This chapter summarizes the modeling considerations needed to develop the most appropriate anisotropic poroelastic finite element double-porosity models of bone. The actual work proposed here would be addressed as part of future studies.

4.2 Poroelasticity Finite Element (FE) Modeling Applied to Bone

Bone can be modeled using the ABAQUS FE code as a porous medium (system) composed of two parts: the solid part (the mineralized bone matrix) and the fluid part (the bone interstitial fluid). Assuming that the constitutive response of the porous medium

consists of a simple bulk elasticity relationship for the fluid and the solid, together with the constitutive theory for the pore matrix, the effective stress (σ^*) can be defined as a function of the strain history (ε^*), temperature (θ), and other variables:

$\sigma^* = \sigma^*$ (ε^*, θ, other variables) in ABAQUS (V6.2, 2002, Hibbitt, Karlsson & Sorensen). Eq. 4-1

Other variables include the bone system values of porosity and permeability. These parameter values are defined in the ABAQUS FE code as follows: a) the porosity of the system, $\phi = V_v/V$, is the ratio of the volume of voids to the total volume; and b) the permeability is the relationship between the volumetric flow rate per unit area of the interstitial fluid through the system and the gradient of the effective fluid pressure. If permeability is given by length^2 (Darcy) unit, then it must be converted such that the appropriate value ($l \times t^{-1}$) is used in ABAQUS FE code (l = length, t = time). Also, depending on the case of material symmetry for the solid part, different material symmetries are characterized by a unique number of independent elasticity coefficients. For example, nine independent elastic constants (three Young's moduli: E_1, E_2 and E_3, three Poisson's ratios: ν_{12}, ν_{13} and ν_{23}, and three shear moduli G_{12}, G_{23} and G_{13}) would characterize orthotropic material symmetry; five independent elastic constants (two Young's moduli: E_1 and E_3, two Poisson's ratios: ν_{12} and ν_{13} and one shear modulus: G_{23}) would characterize transversely isotropic material symmetry; and two independent elastic constants (one Young's modulus: E and one Poisson's ratio: ν) would characterize isotropic material symmetry. The most general degree of anisotropy assumed for bone is that of orthotropic material symmetry (Ashman et al., 1984). Values for the nine elastic

constants needed to fully characterize the orthotropic behavior of the solid part of bone have been reported in the literature (Table 1-3 in Chapter 1).

In the following two sections (4.3 and 4.4) we describe the modeling considerations to calculate pore pressure and velocity fields via the ABAQUS FE code using models that employ the permeability estimates derived from Chapters 2 and 3 for the human osteon and whole rat tibia bone.

4.3 Finite Element Modeling of a Human Osteon

In this section we describe the steps involved in developing poroelastic finite element models of a human osteon with: 1) longitudinally, 2) transversely, and 3) alternately arranged preferential orientation of collagen fibers that include both the vascular porosity and the local permeability of the lacunar-canalicular porosity. These models are different from all the models reported previously in the literature not only because they are double-porosity models but also because they incorporate very accurate anisotropic lacunar-canalicular permeability coefficients (derived from Chapter 2). Because the vascular porosity is at a low pressure, to investigate the fluid response to mechanical loading, the lacunar-canalicular porosity appears to be the most important porosity for the consideration of mechanical and mechanosensory effects in bone. In order to determine the peak pore pressure and the velocity fields in the lacunar-canalicular porosity via an anisotropic poroelastic double-porosity finite element model, the following steps should be performed:

1) An idealized 3-D osteon consisting of the following average dimensions: a) outer radius, R_1 = 172 μm; b) inner radius, R_2 = 34.5 μm; and c) length, L = 516 μm (Fig. 4-1) or similar dimensions should be considered. These dimensions represent a model with a vascular porosity value of 0.04, a value that is well accepted in literature (Schaffler et al., 1988; Zhang et al., 1998). Similar dimensions may be considered; however, one should keep in mind that the model's vascular porosity value should not be violated.

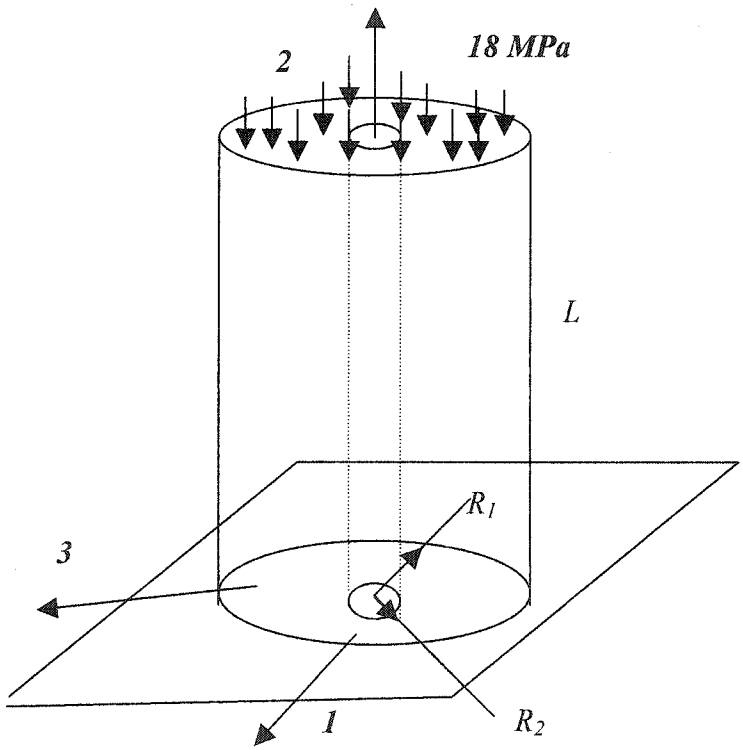

Figure 4-1. *Schematic representation of the human osteonal model. Note: R_1, R_2, and L represent the outer radius, inner radius, and the length of the osteon, respectively. Not drawn to scale.*

2) The bone tissue should be modeled as anisotropic with orthotropic material symmetry with respect to both the fluid and the solid part. Values for the nine elastic constants (three Young's moduli: E_1, E_2 and E_3, three Poisson's ratios: ν_{12}, ν_{13} and ν_{23} and the three shear moduli: G_{12}, G_{23} and G_{13}) needed to fully characterize the orthotropic behavior of the mineralized matrix of bone have been reported in Chapter 1 and for a more complete dataset one should refer to the literature. A lacuna pattern and the local permeability components estimated for human bone in Chapter 2 (orthotropic symmetry with two nonzero permeability values) should be incorporated in the model as shown below (Fig. 4-2A and B).

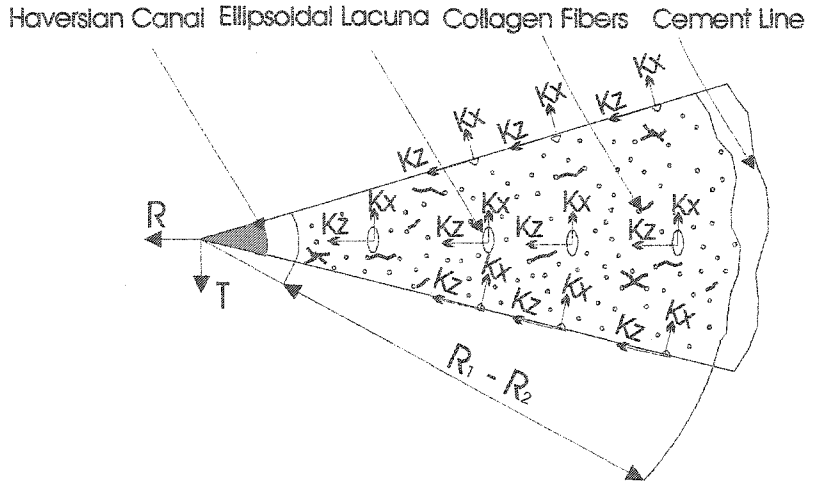

(A)

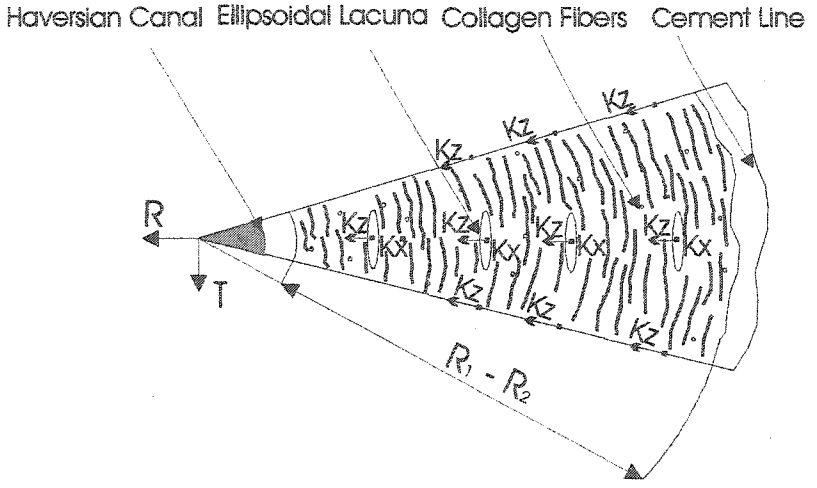

(B)

Figure 4-2. *Schematic illustration of a pie-shaped section of the cross-section of the idealized 3-D osteon (from Fig. 4-1) with (A) longitudinally and (B) transversely arranged preferential orientation of collagen fibers showing an assumed pattern of the elliptical osteocytes along with the corresponding local permeability components. It is assumed that the long axis (y-axis) of the osteocyte lacuna is parallel to the preferential orientation of collagen fibers. Note 1: The dots and the curvy lines in both (A) and (B) represent the collagen fibers. Note 2:* k_X, k_Y *and kz represent the local permeability coefficients calculated for human in Chapter 2 and to match that notation* k_X, k_Y *and kz correspond to* k_1 , k_2 *and* k_3 , *respectively* ($k_Y = k_2 = 0$, *see Chapter 2). Note 3:* R *and* T *stand for radial and tangential, respectively. Not drawn to scale.*

3) For alternately structured osteonal lamina, where the collagen fibers lie along a helical path characteristic of that path (Gebhardt, 1906; Ascenzi et al., 1965; Ascenzi and Benvenuti, 1986; Giraud-Guidlle, 1988) and assuming that the main axis of the osteocyte lacuna is aligned with the preferential length of the collagen fibers (Marotti, 1985) in each lamina, the local permeability components estimated for human bone in Chapter 2 can either be employed directly at each finite element (assuming the size of cuboidal periodic unit cell as the element size) or these estimates may be averaged over the whole osteonal domain. To accomplish this, volume averaging techniques and tensorial transformation laws should be employed first (Note: These models are three-dimensional models. See step 1 for their geometric dimensions).

4) To mimic physiological loading, the model should be cyclically loaded in compression along the long axis. The model should be subjected to a compressive load of 18 MPa along the long axis to produce functional strains of 0.1% (1,000 microstrain) (Zhang et al., 1998) and at various frequencies (e.g., 1.0 Hz, 2.0 Hz, 5.0 Hz, 10 Hz, and 20 Hz) (Wang et al., 1999). The following displacement and pore pressure boundary conditions should be implemented: a) the bottom of the model should be allowed only free translation in the 1 – 3 plane, and two nodes along the inner radius of the model at the bottom surface should be fixed with respect to all degrees of freedom; and b) the surface of the vascular porosity should be set to zero pore pressure magnitude to allow the interstitial fluid from the lacunar-canalicular porosity to flow into and out of the vascular canal (Cowin, 1999) (first load

case scenario). To implement an impervious boundary condition for the cement line, no pressure boundary conditions should be applied at the outer surface of the model. Then, fluid cannot flow across the cement line.

5) As a second load case scenario, to mimic the work of Wang et al. (1999), the outer surface of the model representing the cement line should be set to zero pore pressure magnitude to allow fluid permeation through the cement line as well. (Note: all other boundary conditions applied previously should be kept the same).

6) A coupled pore fluid diffusion and stress analysis should be performed using the ABAQUS FE code, where three-dimensional continuum 20-noded hexagonal elements with quadratic displacement field and linear pore pressure field should be employed (soil element type - C3D20RP).

7) The pore pressure should be requested as an output variable and then the velocity fields can be calculated. Both can be represented as three-dimensional vectors or by contour plots at different time increments.

4.4 Finite Element Modeling of Rat Tibial Cortical Bone

To determine the peak pore pressure and the velocity fields in the lacunar-canalicular porosity of a whole rat tibia cortical bone undergoing mechanical loading, the following steps should be performed to create an anisotropic double-porosity poroelastic finite element model:

1) Reconstruct the three-dimensional structure of the skeletally mature rat tibia from confocal cross-sectional slices (Fig. 4-3). For meshing purposes and to

facilitate incorporation of microstructural details such as the vascular porosity, one should set the length of the reconstructed tibia to be about 6.5 mm or similar dimension can be used (this dimension is used previously in Steck et al., 2003).

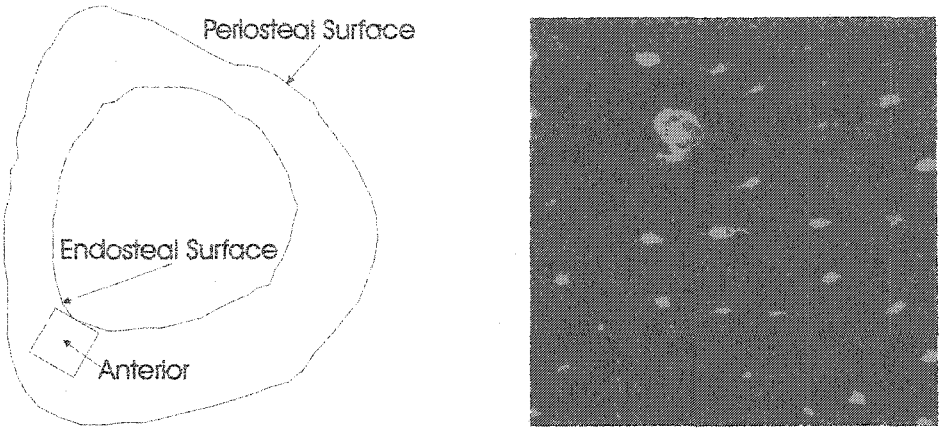

(A) Tibia cross-section (1x) (B) Basic-fuchsin staining (63x)

Figure 4-3. *(A) Schematic representation of the rat tibia cross-section. (B) Confocal image of the lacunar-canalicular network in cross-sectional plane taken from the anterior region of interest. Note: For simplification, no microstructural details such as the vascular canals and the lacunar-canalicular porosity are shown in (A). Not drawn to scale.*

2) The bone tissue should be modeled as anisotropic with respect to both the fluid and the solid part. The distribution of local canaliculi in three dimensions from Chapter 3 ($n_x = 16.7$; $n_y = 13.3$; and $n_z = 27.8$, where x, y and z are the principal axes of the cuboidal periodic unit cell and correspond to the 1, 2, 3 directions) will be used to first estimate the local permeability coefficients (orthotropic symmetry with three nonzero permeability coefficients) and then these coefficients should be incorporated in the model. Using the Weinbaum et al. (1994) model, we calculate the following local

permeability coefficients for rat bone: k_Z = 3.38e-20 m^2, k_X = 2.03e-20 m^2, and k_Y = 1.62e-20 m^2. Using the following rat bone parameters: osteocytic process and canalicular radii: 222.4 nm and 126.8 nm, respectively, cuboidal periodic unit cell length: 23.2 μm, pericellular fiber matrix spacing: 7.0 μm, and fiber radius: 0.6 nm. Since all the above bone parameters were experimentally measured in this study (see Chapter 3) except for the fiber matrix spacing and the fiber radius, we next calculated the permeability coefficients for the parametric values of fiber matrix spacing and fiber radius reported in literature (fiber matrix spacing values of 7.0 μm and 9.0 μm and fiber radius values of 0.6 nm and 1.0 nm). For a fiber matrix spacing value of 9.0 μm and fiber radius values of 1.0 nm and keeping all the other bone parameters the same, the permeability coefficients take the following values: k_Z = 7.60e-20 m^2; k_X = 4.57e-20 m^2; k_Y = 3.63e-20 m^2, respectively. Next, our confocal observations from Chapter 3 in the vicinity of the vascular canals revealed that the highest number of canaliculi corresponded to the direction towards the vascular canal, with the second highest tangential to it and the lowest one along the vascular canal. Such an observation for the bone matrix surrounding the vascular canal would require that the local k_Z be always perpendicular to the vascular canal, the local k_X be tangential to it and the local k_Y be along this axis (Fig. 4-4). However, further investigation is necessary to better establish the lacunae orientation pattern relative to the vascular canals. To accomplish this, confocal scanning at high magnification (63x), which reveals very good details of the lacunar-canalicular network (Fig.

4-3B) should be performed in such a way that these scans should cover the whole cross-section.

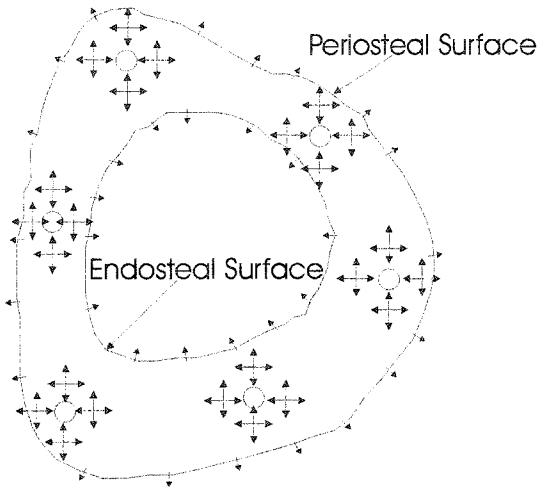

Figure 4-4. *Schematic representation of the rat tibia cross-section including the microstructural detail of the vascular canals (indicated by circles) along with the local permeability components of the lacunar-canalicular porosity. The double-headed arrows represent the k_Z and k_X components of lacunar permeability. Note: k_Y is perpendicular to the other two permeability coefficients (k_Y is not shown). The permeabilities of the endosteal and the periosteal surfaces is represented by the single arrows, respectively. Not drawn to scale.*

3) To mimic the ongoing experimental work by our group, the noninvasive applied loading in those experiments should be used. As a second load case scenario, to mimic the work performed by Steck et al. (2003) the model should be loaded in the medio-lateral direction in four point bending at a frequency of 2 Hz as well. The following displacement and pore pressure boundary conditions should be implemented: a) the bottom of the model should be allowed only free translation in the plane perpendicular to the axial load, and all nodes along the vascular canal at the bottom surface should be fixed with respect to all degrees of freedom for the axial compression load

case scenario (first load case scenario); b) the bottom and the top surfaces of the model should be fixed with respect to all degrees of freedom for the four point bending load case scenario; and b) all the vascular canal surfaces, for both load case scenarios, should be set to zero pore pressure magnitudes (Note: no impervious boundary conditions should be applied in this model since the rat tibia consists mostly of primary bone and does not have cement lines). The permeability values calculated in step 2 should be used throughout the model except for the periosteal and endosteal surfaces, where the values of $k = 10^{-15}$ m^2 (Li et al., 1987), and $k = 2 \times 10^{-12}$ m^2 (Knothe Tate et al., 1998) or similar values should be used for these surfaces, respectively (Steck et al., 2003). These periosteal and the endosteal permeabilities were obtained experimentally and represent permeabilities of interfaces defined as "relatively impermeable" (the periosteal interface) and "relatively permeable" (the endosteal interface) (Cowin, 1999). For the values of the nine elastic constants (three Young's moduli: E_1, E_2 and E_3, three Poisson's ratios: ν_{12}, ν_{13} and ν_{23} and the three shear moduli: G_{12}, G_{23} and G_{13}) needed to fully characterize the orthotropic behavior of the solid part (the mineralized matrix), these values can be obtained from Chapter 1 of this document or for a more complete dataset one should refer to the literature.

4) A coupled pore fluid diffusion and stress analysis should be performed using the ABAQUS FE code, where three-dimensional continuum 20-noded hexagonal elements with quadratic displacement field and linear pore pressure field should be employed (soil element type - C3D20RP).

5) As in the human osteonal models, the pore pressure should be requested first as an output variable and then the velocity fields can be calculated. Both can be represented as three-dimensional vectors or by contour plots at different time increments.

ABAQUS FE code should be used to develop and run the simulation analysis for both the human osteonal models and the whole rat tibia model. One would expect to encounter some difficulty with the implementation of the local permeability coefficients (fluid material properties). However, to overcome this problem, the local permeability coefficients for each element should be applied.

4.5 Expected Results

These FE models will be an improvement over what is currently in the literature not only because they will include both the vascular porosity and the lacunar-canalicular porosity but also because they will incorporate accurate anisotropic lacunar-canalicular permeability coefficients (derived from Chapters 2 and 3). Because the lacunar-canalicular porosity appears to be the most important porosity for the consideration of mechanical and mechanosensory effects in bone, these models would enable more accurate calculations of pore pressure and velocity fields in the lacunar-canalicular network of complex anatomical bone geometries than currently available in the literature.

Chapter 5

Concluding Remarks

5.1 Introduction

The purpose of this work was to better understand bone interstitial fluid flow, which is thought to play an important role in bone's mechanosensory system and bone metabolism. Some of the specific questions addressed were: What is the three-dimensional permeability of the lacunar-canalicular porosity in bone? What is the three-dimensional lacunar-canalicular microstructure? Much of the work focused on linking the three-dimensional bone microstructure to the three-dimensional permeability that could then be used in accurate poroelastic finite element models to solve for fluid pressures and velocities to quantify fluid flow during mechanical loading.

The background for this work was described in Chapter 1 and a two-step analytical approach to determine the degree of anisotropy of the permeability of the lacunar-canalicular porosity in bone was presented in Chapter 2. Chapter 3 described measurements performed using confocal microscopy that provide for the first time a complete three-dimensional characterization of bone's microstructure at the lacunar-canalicular level. Finally, incorporation of the permeability findings and demonstration of the modeling considerations to develop the most appropriate double porosity poroelastic finite element models were described in Chapter 4. The purpose of the present chapter is to summarize the accomplishments of this work, describe the limitations of the accomplishments, and suggest future studies.

5.2 Summary of the Accomplishments

The two-step analytical approach to determine the degree of anisotropy of the permeability of the lacunar-canalicular porosity in bone was presented in Chapter 2. In

the first step, this approach estimated the total number of canaliculi emanating from each osteocyte lacuna based on published measurements from parallel-fibered shaft bones of several species (chick, rabbit, cow, horse, dog, and man). Because the data were obtained from two-dimensional measurements, we developed two methods to estimate the three-dimensional density and distribution of canaliculi emanating from the lacuna: 1) a slicing method and 2) a surface area method. In the second step, the number of canaliculi distributed in three directions was used to determine the local three-dimensional permeability of the lacunar-canalicular porosity for these species by refining a previously developed microstructural model to both account for the anisotropic effect of the lacunar-canalicular porosity and also to include more recent, accurate bone microstructural parameters than previously used.

Our calculations in Chapter 2 show that osteocyte lacunar shape and size along with the canalicular distribution in three dimensions are parameters that determine the degree of anisotropy of the local permeability of the lacunar-canalicular porosity. We found that the number of canaliculi per osteocyte lacuna varies for different species, ranging from 41 for man to 115 for horse. Lacunar-canalicular permeability coefficients were found to be different in three local principal directions, indicating local orthotropic symmetry of bone permeability in parallel-fibered cortical bone for all species examined. Important parameters that affect the lacunar-canalicular permeability calculation are the canalicular and osteocyte process dimensions and the pericellular fiber matrix spacing dimensions. The canalicular and osteocyte process dimensions, which determine the annulus through which the interstitial fluid flows, had the largest effect on the permeability coefficients, which varied almost three orders of magnitude (from order 1×10^{-22} m^2 to 1×10^{-19} m^2)

for the small (15 nm), medium (77.5 nm), and large annulus (150 nm) configurations investigated. The permeability coefficients were less sensitive to pericellular fiber matrix spacing, demonstrating approximately a 50% increase in permeability for a fiber matrix spacing of 8 nm and a 60% increase in permeability for a spacing of 9 nm compared to the permeability calculated with a spacing of 7 nm.

Because of the lack of three-dimensional measurements of the lacunar-canalicular porosity in the literature, we next designed experiments to confirm and further quantify the essential bone parameters used in the theoretical model. Three-dimensional measurements of the volumetric lacunar density, osteocyte lacunar axis lengths, number of canaliculi emanating from each lacuna, number of canaliculi intersected by the bone territory assigned to each individual lacuna, and the canaliculus annulus size were performed using different staining techniques and confocal laser scanning microscopy. Our experimental measurements presented in Chapter 3 showed that osteocyte lacunae of male Sprague Dawley rats resemble triaxial ellipsoids with major, intermediate, and minor axes lengths of approximately 18 μm, 6 μm, and 4 μm, respectively. The number of canaliculi directly emanating from each lacuna was approximately 53, which falls within the range of reported values in the literature and compares most closely to the number of canaliculi emanating from chick lacunae calculated in our theoretical study presented in Chapter 2. The number of canaliculi intersected by all faces of the cuboidal periodic unit cell, which represents the bone matrix volume assigned to each individual lacuna, was found to be 116. The difference between the number of canaliculi emanating directly from the osteocyte lacuna (~53 canaliculi) and the number of canaliculi found

crossing the faces of the cuboidal unit cell surrounding the lacuna (116 canaliculi) demonstrates the large amount of canalicular branching observed in rat bone.

Our observations of rat bone using confocal microscopy also revealed that the highest number of canaliculi intersecting the faces of the cuboidal periodic unit cell was along the minor axis of the triaxial osteocyte lacuna, with the second highest and the lowest along the intermediate and the major axes, respectively. The degree of orthotropy of the canaliculi distribution measured in rat bone (Table 1 in Chapter 3) was somewhat different from the degree of orthotropy of the canaliculi distribution estimated for the six different species based on data from the literature (Table 3 in Chapter 2). The ratios reported in Chapter 2 were found from canaliculi that directly emanate from the lacuna (first order canaliculi), whereas the ratios measured in Chapter 3 were for canaliculi that have branched (second order canaliculi). The branching of first order canaliculi and the high number of the osteocyte processes joining adjacent osteocyte processes at right angles, which was evident in the confocal study, are the reasons for the differences in the degree of orthotropy. In light of our experimental observations for the canaliculi distribution in three dimensions in rat bone, the validity of our assumption in Chapter 2 that no canaliculi cross the cuboidal periodic unit cell in the direction of the long axis of the osteocyte lacuna in the species examined in our analytical approach is questionable without further experimental investigations. To confirm or revise the validity of this assumption, similar measurements of the lacunar-canalicular structure should be made in chick, rabbit, cow, horse, dog, and man using confocal microscopy.

Finally, in Chapter 4 we discussed how future work could incorporate the local orthotropic permeability findings into finite element models of human osteonal bone and

rat tibial bone, and we demonstrated the modeling considerations necessary to develop the most appropriate anisotropic poroelastic finite element models that can solve for load-induced pore pressure and velocity fields. These models will be an improvement over what is currently in the literature not only because they will include both the vascular porosity and the lacunar-canalicular porosity but also because they will incorporate accurate anisotropic lacunar-canalicular permeability coefficients (derived from Chapters 2, 3 and 4). Because the lacunar-canalicular porosity appears to be the most important porosity for the consideration of mechanical and mechanosensory effects in bone, these models would enable more accurate calculations of pore pressure and velocity fields in the lacunar-canalicular network of complex anatomical bone geometries than currently available in the literature.

5.3 Limitations and Future Studies

There are several limitations to this work. For the theoretical model presented in Chapter 2, a limitation is that the values used for the canalicular and osteocyte process dimensions were from mice; similar measurements in the other species used would be more appropriate (although it should be noted that the estimations of the rat canaliculus annulus width presented in Chapter 3 are very close to the mice measurements). Also in the analytical approach we assumed that canaliculi run perpendicular to the major axis (the long axis) of the osteocyte lacuna so that no canaliculi cross the cuboidal periodic unit cell in the direction of the long axis of the lacuna, as noted above. Our experimental three-dimensional confocal microscopy results from rats revealed that canaliculi do not run only toward and tangential to the vascular canals as concluded from two-dimensional

images in the literature but rather have a three-dimensional distribution (i.e., canaliculi cross the bone territory assigned to each individual lacuna along the long axis of the osteocyte lacuna as well). Thus, similar experiments in chick, rabbit, cow, horse, dog, and man using confocal microscopy should be performed to assess whether canaliculi have a similar distribution in those species.

Another limitation of our analytical study is that in accordance with the microstructural model of Weinbaum et al. (1994), we considered the case of straight canalicular channels that pass from one face of the ellipsoidal lacuna directly to the opposing face of the cuboidal unit cell. Canaliculi were idealized as straight tubes because accurate measurement of the channel contortions is very difficult. Osteocyte processes exhibit tortuosity, traveling between adjacent lacuna and from lacuna to the bone surfaces through winding canaliculi that may branch during their course. These limitations could be addressed in the next refinement of the model. We do think, however, that accounting for the effects of tortuosity will affect the values reported by a factor that is less than an order of magnitude, perhaps a factor of 3. The effect of canalicular branching on permeability awaits future studies.

The confocal microscopy portion of this study also has several limitations. One limitation relates to making actual length measurements (the lacunar axis lengths, the osteocyte process width, and the canalicular width). While it was assumed that phalloidin outlines the outermost boundary of the osteocyte processes and that basic fuchsin outlines the outermost boundary of the osteocyte lacunae and canaliculi, strong evidence to confirm the above assumptions has yet to be found. Also, the choice of settings used in confocal laser scanning microscopy for the detector gain, the amplifier

offset, and the amplifier gain will most likely have a slight effect on the size of canaliculi and osteocyte processes measurements, as well as the lacunar axis length measurements. Quantification of this effect, by setting these parameters to their maximum and minimum positions, remains to be done. However, since the settings used for both phalloidin and basic fuchsin stains were the same and since the difference between the canaliculus radius and osteocytic processes radius gives the value of the canaliculus annulus, one could conclude that our measured value for the canaliculus annulus size is not affected by the choice of the settings used and therefore is an accurate measurement. We must add that the settings chosen produced the best sets of confocal laser scanning microscopy images. In any case, to obtain very accurate measurements for length measurements using confocal laser scanning microscopy, correlation of the morphology of identical areas with objects of known size must be performed.

Finally, when using the microstructural measurements from Chapter 3 to calculate the lacunar-canalicular permeability for rat bone (Chapter 4) the microstructural model of Weinbaum et al. (1994) was also used. As described above, the model of Weinbaum et al. (1994) does not account for the effects of tortuosity of canaliculi, which was evident in the rat bone. In addition, our experimental results revealed that canaliculi exhibit extensive branching, whereas in the calculation we assumed that the same number of canaliculi pass from the lacuna to the edge of the cuboidal periodic unit cell. This suggests once again that the effects of canalicular branching and tortuosity on permeability must be accounted for in the next refinement of this model. We do think, however, that tortuosity and branching have an opposite effect on the permeability, with tortuosity decreasing the permeability and branching increasing the permeability. In light

of these findings we also suggest again that future confocal investigations should be carried out for other types of bone examined previously in our analytical study (chick, rabbit, cow, horse, dog, and man).

References For Chapter 1

ABAQUS Manuals-V.6.2. (2002). Pawtucket RI, U.S.A.: Hibbitt, Karlsson & Sorensen Inc.

Aarden, M.E., Burger, E.H., and Nijweide, P.J., 1994. Function of osteocytes in bone. Journal of Cellular Biochemistry. 55: 287-299.

Ardizzoni, A., 2001. Osteocyte lacunar size-lamellar thickness relationship in human secondary osteons. Bone. 28: 215-219.

Anderson, C.B., 1967. Mechanics of fluids. In: Baumeister. T. (Ed). Marks' Saturated Handbook for Mechanical Engineers. pp. 348-376.

Atkinson, P.J., and Hallsworth, A.S., 1982. The spatial structure of bone. Progress in Anatomy. 2: 179-199.

Atkinson, P.J., and Hallsworth, A.S., 1983. The changing pore structure of aging human mandibular bone. Gerodontology. 2: 57-64.

Ascenzi, A., Bonuci, E., and Bocciarelli, D.S. 1965. An electron microscopy study of osteon calcification. J Ultrastruct Res. 12: 287-235.

Ascenzi, A., and Benvenuti, A., 1986. Orientation of collagen fibers at the boundary between two successive osteonic lamellae and its mechanical interpretation. Journal of Biomechanics. 19: 455-463.

Ashman, R.B., Cowin, S.C., Van Buskirk, W.C., and Rice, J.C., 1984. A continuous wave technique for the measurement of the elastic properties of cortical bone. Journal of Biomechanics. 17: 249-361.

Baylink, D., and Wergedal. J., 1971. Bone formation and resorption by osteocytes. Cellular Mechanics for Calcium Transfer and Homeostasis. George Nichols, Jr., and R.H. Wasserman. Eds., Academic Press, New York-London, 257-289.

Beaudoin, A.J., Mihalko, W.M., and Krause, W.R., 1991. Finite element modeling of polymethylmethacrylate flow through cancellous bone. Journal of Biomechanics. 24 (2): 127-136.

Biot, M.A., 1941. General theory of three-dimensional consolidation. Journal of Applied Physics. 12: 155-164.

Cane, V., Marotti, G., Volpi, G., Zaffe, D., Palazzini, S., Remaggi, F., and Muglia, M.A., 1982. Size and density of osteocyte lacuna in different regions of long bones. Calcified Tissue International. 34: 558-563.

Carola, R., Harley, J.P., and Noback, C.R., 1990. Human Anatomy and Physiology, McGraw-Hill, New York.

Cowin, S.C., Weinbaum, S., and Zeng, Y., 1995. A case for bone canaliculi as the anatomical site of strain generated potentials. Journal of Biomechanics. 28: 1281-1296.

Cowin, S.C., 1999. Bone poroelasticity. Journal of Biomechanics. 32: 217-238.

Cowin, S.C., 2001. Bone Mechanics Handbook, 2nd edition.

Cowin, S.C., 2003. A recasting of anisotropic poroelasticity in matrices of tensor components. Transport in Porous Media. 50: 35-56.

DIANA. Livonia MI, U.S.A.: TNO DIANA North America Inc.

Dillaman, R.M., Roer, R.D., and Gay, D.M., 1991. Fluid movement in bone: Theoretical and Empirical. Journal of Biomechanics. 24: 163-177.

Ferretti, M., Muglia, M.A., Remaggi, F., Cane, V., and Palumbo, C., 1999. Histomorphometric study on the osteocyte lacuna-canalicular network in animals of different species. It. J. Anat. Embryol. 104: 121-131.

Fritton, S.P., Wang, L., Cowin, S.C., and Weinbaum, S., 1999. Tracer transport in lacunar-canalicular system under cyclic loading within osteonal bone, Proceedings of the 1999 Bioengineering Conference, ASME-BED. 42: 491-492.

Frost, H.M., 1960. Measurement of osteocytes per unit volume and volume components of osteocytes and canaliculae in man. Henry Ford Hospital Medical Bulletin. 8: 208-211.

Frost, H.M., 1962. Specific surface and specific volume of normal human lamellar bone. Henry Ford Hospital Medical Bulletin. 10: 35.

Gebhardt, W., 1906. Uber funktionell wichtige Anordnungsweisen der feineren und groberen lensysteme des Wirbeltieknochens. II. Spezieller Teil. Der Bau der Haversschen Lamel-lensysteme und seine funktionelle Bedeutung. Arch Entwickl Mech Org. 20: 187-322.

Giraud-Guille, M.M., 1988. Twisted plywood architecture of collagen fibrils in human compact bone osteons. Calcified Tissue International. 42: 167-180.

Grimm, M.J., and Williams, J.L., 1997. Measurements of permeability in the human calcaneal trabecular bone. Journal of Biomechanics. 30: 743-745.

Grotz, K.A., Piepkor, B., Al-Nawas, B., Duschner, H., Bittinger, F., Kann, P., Beyer, J., and Wagner, W., 1999. Confocal laser scanning microscopy: A nondestructive subsurface histotomography of healthy human bone. Calcified Tissue International. 65: 8-10.

Gross, D. and Williams, W.S., 1982. Streaming potential and the electromechanical response of physiologically-moist bone. Journal of Biomechanics. 15: 277-295.

Hui, P.W., Leung, P.C., and Sher, A., 1996. Fluid conductance of cancellous bone graft as a predictor for graft-host interface healing. Journal of Biomechanics. 29(1): 123-132.

Jee, W. S. S., 2001. Integrated Bone Tissue Physiology: Anatomy and Physiology. Chapter 1 in Bone Mechanics Handbook, 2nd edition, S.C. Cowin (Ed.), pp.1-1 - 1-68.

Katz, J.L., Yoon, H.S., Lipson, S., Maharidge, R., Meunier, A., and Christel, P., 1984. The effects of remodeling on the elastic properties of bone. Calcified Tissue International. 36 (Suppl.): 31-36.

Kamioka, H., Honjo, T., and Takano-Yamamoto, T., 2001. A three-dimensional distribution of osteocyte processes revealed by the combination of confocal laser scanning microscopy and differential interference. Bone. 28: 145-149.

Klein-Nulend, J., van der Plas, A., Semeins, C.M., Ajubi, N.E., Frangos, J.A., Nijweide, P.J., and Burger, E.H., 1995. Sensitivity of osteocytes to biomechanical stress in vitro. FASEB. 9: 441-445.

Knapp, H.F., Reilly, G.C., Stemmer, A., Niederer, P., and Knothe Tate, M.L., 2002. Development of preparation methods for and insights obtained from atomic force microscopy of fluid spaces in cortical bone. Scanning. 24: 25-33.

Knothe Tate, M.L., Niederer, P., and Knothe, U., 1998. In vivo tracer transport through the lacunocanalicular system of rat bone in an environment devoid of mechanical loading. Bone. 22: 107-117.

Knothe Tate, M.L., Knothe, U., and Neiderer, P., 1998b. Experimental elucidation of mechanical load-induced fluid flow and its potential role in bone metabolism and functional adaptation. American Journal of the Medical Sciences. 316: 189-95.

Kohles, S.S., Roberts, J.B., Upton, M.L, Wilson C.G., Bonassar, L.J., and Schlichting, A.L., 2001. Direct perfusion measurements of cancellous bone anisotropic permeability. Journal of Biomechanics. 34: 1197-1202.

Kufahl, R.H., and Saha, S., 1990. A theoretical model for stress-generated fluid flow in t the canaliculi-lacunae network in bone tissue. Journal of Biomechanics. 23: 171-180.

Lacroix, P., 1951. The organization of bone. J & A Churchill Ltd, London.

Lang, S.B., 1970. Ultrasonic method for measuring elastic coefficients of bone and results on fresh and dried bones. IEEE Transactions on Biomedical Engineering. 17: 101-105.

Li, G., Bronk, J.T., An, K., and Kelly, P.J., 1987. Permeability of cortical bone of canine tibiae. Microvascular Research. 34: 302-310.

Lim, T.H., and Hong, J.H., 2000. Poroelastic properties of bovine vertebral trabecular bone. Journal of Orthopedic Research. 18 (4): 671-677.

Loret, B., Rizzi, E., and Zefra, Z., 2001. Relations between drained and undrained moduli in anisotropic poroelasticity. Journal of the Mechanics and Physics of Solids. 49: 2593-2619.

Mak, A.T., Huang, D.T., Zhang, J.D., and Tong, P., 1997. Deformation induced hierarchical flows and drag forces in bone canaliculi and matrix microporosity. Journal of Biomechanics. 30: 11-18.

Mak, A.T., and Zhang, J.D., 2001. Numerical simulation of streaming potential due to deformation-induced hierarchical flows in cortical bone. Transactions of the ASME. 123: 66-70.

Manfredini, P., Cocchetti, G., Maier, G., Redaelli, A., and Montevecchi, F. M., 1999. Poroelastic finite element analysis of a bone specimen under cyclic loading. Journal of Biomechanics. 32: 135-144.

Marotti, G., 1979. Osteocyte orientation in human lamellar bone and its relevance to the morphometry of periosteocytic lacuna. Metab. Bone Dis. & Rel. Res. 1: 325-333.

Marotti, G., Remaggi, F., and Zaffe, D., 1985. Quantitative investigation on osteocyte canaliculi in human compact and spongy bone. Bone. 6: 335-337.

Marotti, G and Muglia, M.A., 1988. A scanning electron microscopy study of human bony lamellae. Proposal for a new model of collagen lamellar organization. Arch Ital Anat Embriol. 93: 163-175.

Marotti, G., 1990. The original contribution of the scanning electron microscopy to the knowledge of bone structure. In: Bonucci E, Motta PM: Ultrastructure of skeletal tissue; Kluwer Academic Publisher, Boston, Dordrecht, London, pp. 19-39.

Marotti, G., Ferretti, M., Muglia, M. A., Palumbo, and C., Palazzini, S., 1992. A quantitative evaluation of osteoblast-osteocyte relationships on growing endosteal surface of rabbit tibia. Bone. 13: 363-368.

Marotti, G., 1993. A new theory of bone lamellation. Calcified Tissue Int. 53 (suppl. 1): 47-56.

Marotti, G., Muglia, M.A., and Palumbo, C., 1994a. Structure and function of lamellar bone. Clin Rheumatol. 13 (Suppl. 1): 63-68.

Marotti, G., Muglia, M.A., Palumbo, C., and Zaffe, D., 1994b. The microscopic determinants of bone mechanical properties. Ital J Mineral Electrolyte Metab. 8: 167-175.

Marotti, G., Ferretti, M., Remaggi, F., and Palumbo, C., 1995. Quantitative evaluation on osteocyte canalicular density in human secondary osteons. Bone. 16: 125-128.

Marotti, G., 1996. The structure of bone tissue and the cellular control of their deposition. Italian Journal of Anatomy and Embryology. 4: 25-79.

McCreadie, B.R., Hollister, S.J., Schaffler, M.B., and Goldstein, S.A. 2004. Osteocyte lacuna size and shape in women with and without osteoporotic fracture. Journal of Biomechanics. 37: 563-572.

McLean, F.C., and Urist, M.B., 1961. Bone: An introduction to the physiology of skeletal tissue. 2nd ed, University of Chicago Press, Chicago.

Morris, M.A., Lopez-Curato, J.A., Hughes, S.P.F, An, K.N., Bassingthwaighte, J.B., and Kelly, P.J., 1982. Fluid spaces in canine bone and marrow. Microvascular Research. 23: 188-200.

Moss, M.L., and Cowin, S.C., 1997. Mechanosensory mechanisms in bone. In: Lanza, R., Langer, R., Chick, W. (Eds), Textbook of Tissue Engineering. R.G. Landes, Austin, pp. 645-659.

Mow, V.C., Kuei, S.C., Lai, W/L., and Armstrong. C., 1980. Biphasic creep and stress-relaxation of articular cartilage in compression: theory and experiment. Journal of Biomechanical Engineering. 102: 73-84.

Mullender, M.G., Van der Meer, D.D., Huiskes, R., and Lips, P., 1996. Osteocyte density changes in aging and osteoporosis. Bone. 18: 109-113.

Mullender, M.G., Huiskes, R., Versleyen, H., and Buma, P., 1996. Osteocyte density and histomorphometric parameters in cancellous bone of the proximal femur in five mammalian species. Journal of Orthopedic research.14: 972-979.

Nauman, E.A., Fong, K.E., and Keaveny. T.M., 1999. Dependence of intrabecular permeability of flow direction and anatomical site. Annals of Biomedical Engineering. 27: 517-524.

Ochoa, J.A., and Hillbery, B.M., 1992. Permeability of bovine cancellous bone. Transaction of the ORS. 17: 162.

Otter, M.W., Palmieri, V.R., Wu, D.D., Seiz, K.G., MacGinitie, L.A., and Cochran, G.V.B., 1992. A comparative analysis of streaming potentials *in vivo* and *in vitro*. Journal of Orthopedic Research. 10: 710-719.

Otter, M.W., MacGinitie, L.A., Seiz, K.G., Johnson, M.W., Dell, R.B., and Cochran, G.V.B., 1994. Dependence of streaming potential frequency response on sample thickness: implications for fluid flow through bone microstructure. Biometrics. 2: 57-75.

Palumbo, C., 1986. A three-dimensional ultrastructural study of osteoid-osteocyte in the tibia of chick embryos. Calcified Tissue International. 246: 125-131.

Palumbo, C., Palazzini, S., and Marotti, G., 1990. Morphologic study of intracellular junction during osteocyte differentiation. Bone. 136: 239-255.

Pawlicki, R., 1975. Bone canaliculus endings in the area of the osteocyte lacuna. Acta Anatomy. 91: 292-304.

Petrov, N., Pollack, S.R., and Blagoeva, R., 1989. A discrete model for streaming potentials in a single osteon. Journal of Biomechanics. 22: 517-521.

Piekarski, K., and Munro, M., 1977. Transport mechanism operating between blood supply and osteocytes in long bones. Nature. 269: 80-82.

Pollack, S.R., Petrov, N., Salzstein, R., Brankov, G., and Blagoeva, R., 1984. An anatomical model for streaming potentials in osteons. Journal of Biomechanics. 17: 627-636.

Pritchard, J.J., 1956. General anatomy and histology of bone. In: Bourne GH: The biochemistry and physiology of bone; 2nd ed, vol. 1; Academic Press, New York, London, pp. 1-25.

Qin, Y.X., 1997. Fluid flow, matrix strain and loading frequency as independent control parameters in skeletal adaptation. PhD, thesis, SUNY.

Qin, Y.X., Kaplan, T., Saldanha, A., and Rubin, C., 2002. Fluid pressure gradients, arising from oscillations in intramedullary pressure, is correlated with the formation of bone and inhibition of intracortical bone. Journal of Biomechanics.36: 1427-1437.

Qin, Y.X., Lin, W., and Rubin, C., 2003. The pathway of bone fluid flow as defined by *in vivo* intramedullary pressure and streaming potential measurements. Annals of Biomedical Engineering. 30: 693-702.

Reich, K.M., Gay, C.V., and Frangos, J.A., 1990. Fluid shear stress as a mediator of osteoblast cyclic adenosine monophosphate production. J Cell Physiol. 143: 100-104.

Reilly, D.T., and Burstein, A.H., 1975. The elastic and ultimate properties of compact bone tissue. Journal of Biomechanics. 8: 393-405.

Remaggi, F., Can, V., Palumbo, C., and Ferretti, M. 1998. Histomorphometric study on the osteocyte lacuno-canalicular network in animals of different species. I. Woven-fibered and parallel-fibered bones. Italian Journal of Anatomy and Embryology. 103: 145-155.

Rice, J.R., and Cleary, M.P., 1976. Some basic stress diffusion solutions for fluid-saturated elastic porous media with compressibility constituents. Reviews of Geophysics and Space Physics. 14: 227-241.

Riggs, B.L., and Melton, L.J., 1995. The worldwide problem of osteoporosis: Insights afforded by epidemiology. Bone. 17: (Suppl.): 505-511.

Rouhana, S.W., Johnson, M.W., Chakkalakal, D.A., and Harper, R.A., 1981. Permeability of compact bone. Joint ASME-ASCE Conference of Biomechanics Symposium AMD. 43: 169-172.

Salzstein, R.A., Pollack, S.R., Mak, A.F.T., and Petrov, N., 1987. Electromechanical potentials in cortical bone - I. A continuum approach. Journal of Biomechanics. 20: 261-270.

Salzstein, R.A., and Pollack, S.R., 1987. Electromechanical potentials in cortical bone – II. Experimental analysis. Journal of Biomechanics. 20: 271-280.

Skempton, A.W., 1954. The pore pressure coefficient A and B. Geotechnique. 4: 143-147.

Schaffler, M.B., and Burr, D.B., 1988. Stiffness of compact bone: effects of porosity and density. Journal of Biomechanics. 21: 13-16.

Scott, G.C., and Korostof, E., 1990. Oscillatory and step response of electromechanical phenomena in human and bovine bone. Journal of Biomechanics. 23: 127-143.

Sevostianov, I., and Kachanov, M., 1999. Impact of the porous microstructure on the overall elastic properties of the osteonal cortical bone. Journal of Biomechanics. 33: 881-888.

Sissons, H.A., and O'Connor, P., 1977. Quantitative histology of osteocyte lacunae in normal human cortical bone. Calcified Tissue International. 22: (Suppl.), 530-533.

Smit, T.H., Huyghe, J.M., and Cowin, S.C., 2002. Estimation of the poroelastic parameters of cortical bone. Journal of Biomechanics. 35: 829-835.

Squire, J.M., Chew, M., Nneji, G., Neal, Ch., Barry, J., and Michel, Ch., 2001. Quasi-periodic substructure in the microvessel endothelial glycocalyx: A possible explanation for molecular filtering. Journal of Structural Biology. 136: 239-255.

Starkebaum, W., Pollack, S.R., and Korostof, E., 1979. Microelectrode studies of stress-generated potentials in four-point bending of bone. Journal of Biomedical Materials Research. 13: 729-751.

Steck, R., Niederer, P., and Knothe Tate, M.L., 2003. A finite element analysis for the prediction of load-induced fluid flow and mechanochemical transduction in bone. Journal of Theoretical Biology. 220: 249-259.

Stout, S.D., Brunsden, B.S., Hildebolt, C.F., Commean, P.K., Smith, K.E., and Tappen, N.C., 1999. Computer-assisted 3D Reconstruction of the serial section of cortical bone to determine the 3D structure of osteons. Calcified Tissue International. 65: 280-284.

Van Burskirk, W.C., and Ashman, R.B., 1981. The elastic moduli of bone . In: Cowin, S.C. (Ed.), Mechanical Properties of Bone, Vol. AMD 36, ASME, New York, pp. 131-143.

Vashishth, D., Verborgt, O., Divine, G., Schaffler, M.B., and Fyhrie, D.P., 2000. Decline in osteocyte lacunar density in human cortical bone is associated with accumulation of microcracks. Bone. 26:375-380.

Wang, L., Fritton, S.P., Cowin, S.C., and Weinbaum, S., 1999. Fluid pressure relaxation depends upon osteonal microstructure: modeling an oscillatory bending experiment. Journal of Biomechanics. 32: 663-672.

Wang, L., Ciani, C., Doty, S.B., and Fritton, S.P., 2004a. Delineating bone's interstitial fluid pathway in vivo. Bone. 34: 499-509.

Wang, Y., Schaffler, M., Weinbaum, S., and Wang, L., 2004b. Morphologic variation of the osteocyte lacunar-canalicular system in inbred mice. Proceedings of the Biomedical Engineering Society Annual Fall Meeting. 939.

Weimann, J.P., and Sicher, H., 1955. Bone and bones. Fundamentals of Bone Biology. 2nd ed, Mosby, St Luis.

Weinbaum, S., Cowin, S.C., and Zeng, Y., 1994. A model for the excitation of osteocytes by mechanical loading-induced bone fluid shear stresses. Journal of Biomechanics. 27: 339-360.

Weiner, S., Arad, T., Sabanay, I., and Traub, W. 1997. Rotated plywood structure of primary lamellar bone in the rat: Orientations of the collagen fibril arrays. Bone 20(6): 509-514.

You, L., Cowin, S.C., Schaffler, M., and Weinbaum, S. 2001. A model for strain amplification in the actin cytoskeleton of osteocytes due to fluid drag on pericelular matrix. Journal of Biomechanics. 34(11): 1375-1386.

You, L., 2002. A new view of mechanotransduction in bone cells. PhD thesis, CUNY.

Zeiss LSM 510 Users Manual-V.3.2. (2000). Thornwood NY, U.S.A.: Carl Zeiss MicroImaging Inc.

Zeng, Y., Cowin, S.C., and Weinbaum, S., 1994. A fiber matrix model for fluid flow and streaming potentials in the canaliculi of an osteon. Annals Biomedical Engineering. 22: 280-292.

Zioupos, P., Currey, J.D., Mirza, M.S., and Barton, D.C., 1995. Experimentally determined microcracking around a circular hole in a flat plate of bone: comparison with predicted stresses. Philosophical Transactions of Royal Society of London B. 347: 383-396.

Zhang, D., Weinbaum, S., and Cowin, S.C., 1994. Oscillatory bending of a poroelastic beam. Journal of Mechanical Physics Solids. 42: 1575-1599.

Zhang, D., Weinbaum, S., and Cowin, S.C., 1998. Estimates of the peak pressure in the bone pore water. Journal of Biomechanical Engineering. 120: 697-703.

References For Chapter 2

Atkinson, P.J., Hallsworth, A.S., 1982. The spatial structure of bone. Progress in Anatomy 2, 179-199.

Cane, V., Marotti, G., Volpi, G., Zaffe, D., Palazzini, S., Remaggi, F., Muglia, M.A., 1982. Size and density of osteocyte lacuna in different regions of long bones. Calcified Tissue International 34, 558-563.

Cowin, S.C., 1999. Bone poroelasticity. Journal of Biomechanics 32, 217-38.

Cowin, S.C., Weinbaum, S., Zeng, Y., 1995. A case for bone canaliculi as the anatomical site of strain generated potentials. Journal of Biomechanics 28, 1281-1296.

Dillaman, R.M., Roer, R.D., Gay, D.M., 1991. Fluid movement in bone: theoretical and empirical. Journal of Biomechanics 24, 163-177.

Ferretti, M., Muglia, M.A., Remaggi, F., Cane, V., Palumbo, C., 1999. Histomorphometric study on the osteocyte lacuno-canalicular network in animals of different species. II. Parallel-fibered and lamellar bones. Italian Journal of Anatomy and Embryology 104, 121-131.

Grimm, M.J., Williams, J.L., 1997. Measurements of permeability in the human calcaneal trabecular bone. Journal of Biomechanics 30, 743-745.

Hillsley, M.V., Frangos, J.A., 1994. Review: Bone tissue engineering: the role of interstitial fluid flow. Biotechnology and Bioengineering 43, 573-581.

Klein-Nulend, J., van der Plas, A., Semeins, C.M., Ajubi, N.E., Frangos, J.A., Nijweide, P.J., Burger, E.H., 1995. Sensitivity of osteocytes to biomechanical stress in vitro. FASEB 9, 441-445.

Knapp, H.F., Reilly, G.C., Stemmer, A., Niederer, P., Knothe Tate, M.L., 2002. Development of preparation methods for and insights obtained from atomic force microscopy of fluid spaces in cortical bone. Scanning 24, 25-33.

Kohles, S.S., Roberts, J.B., Upton, M.L., Wilson, C.G., Bonassar, L.J., Schlichting, A.L., 2001. Direct perfusion measurements of cancellous bone anisotropic permeability. Journal of Biomechanics 34, 1197-1202.

Li, G., Bronk, J.T., An, K., Kelly, P.J., 1987. Permeability of cortical bone of canine tibiae. Microvascular Research 34, 302-310.

Lim, T.-H., Hong, J.H., 2000. Poroelastic properties of bovine vertebral trabecular bone. Journal of Orthopedic Research 18, 671-677.

Manfredini, P., Cocchetti, G., Maier, G., Redaelli, A., Montevecchi, F. M., 1999. Poroelastic finite element analysis of a bone specimen under cyclic loading. Journal of Biomechanics 32, 135-144.

Marotti, G., 1979. Osteocyte orientation in human lamellar bone and its relevance to the morphometry of periosteocytic lacuna. Metabolic Bone Disease & Related Research 1, 325-333.

Marotti, G., Ferretti, M., Muglia, M. A., Palumbo, C., Palazzini, S., 1992. A quantitative evaluation of osteoblast-osteocyte relationships on growing endosteal surface of rabbit tibia. Bone 13, 363-368.

Marotti, G., Ferretti, M., Remaggi, F., Palumbo, C., 1995. Quantitative evaluation on osteocyte canalicular density in human secondary osteons. Bone 16, 125-128.

Marotti, G., 1996. The structure of bone tissue and the cellular control of their deposition. Italian Journal of Anatomy and Embryology 4, 25-79.

Mathematica V.2.2. 2003. Wolfram Research Inc., USA.

Nauman, E.A., Fong, K.E., Keaveny, T.M., 1999. Dependence of intertrabecular permeability on flow direction and anatomic site. Annals of Biomedical Engineering 27, 517-524.

Qin, Y.X., 1997. Fluid flow, matrix strain and loading frequency as independent control parameters in skeletal adaptation. Ph.D. thesis, State University of New York at Stony Brook.

Qin, Y.X., Lin, W., Rubin, C., 2002. The pathway of bone fluid flow as defined by *in vivo* intramedullary pressure and streaming potential measurements. Annals of Biomedical Engineering 30, 693-702.

Remaggi, F., Cane, V., Palumbo, C., Ferretti, M., 1998. Histomorphometric study on the osteocyte lacuno-canalicular network in animals of different species. I. Woven-fibered and parallel-fibered bones. Italian Journal of Anatomy and Embryology 103, 145-155.

Rouhana, S.W., Johnson, M.W., Chakkalakal, D.A., Harper, R.A., 1981. Permeability of the osteocyte lacuno-canalicular compact bone. Joint ASME-ASCE Conference Biomechanics Symposium AMD 43, pp. 169-172.

Sander, E.A., Nauman, E.A., 2003. Permeability of musculoskeletal tissues and scaffolding materials: experimental results and theoretical predictions. Critical Reviews in Biomedical Engineering 31, 1-26.

Smit, T.H., Huyghe, J.M., Cowin, S.C., 2002. Estimation of the poroelastic parameters of cortical bone. Journal of Biomechanics 35, 829-835.

Squire, J.M., Chew, M., Nneji, G., Neal, C., Barry, J., Michel, C., 2001. Quasi-periodic substructure in the microvessel endothelial glycocalyx: a possible explanation for molecular filtering. Journal of Structural Biology 136, 239-255.

Steck, R., Niederer, P., Knothe Tate, M.L., 2003. A finite element analysis for the prediction of load-induced fluid flow and mechanochemical transduction in bone. Journal of Theoretical Biology 220, 249-259.

Wang, L., Fritton, S.P., Cowin, S.C., Weinbaum, S., 1999. Fluid pressure relaxation depends upon osteonal microstructure: modeling an oscillatory bending experiment. Journal of Biomechanics 32, 663-672.

Wang, L., Ciani, C., Doty, S.B., Fritton, S.P., 2004a. Delineating bone's interstitial fluid pathway in vivo. Bone 34, 499-509.

Weinbaum, S., Cowin, S.C., Zeng, Y., 1994. A model for the excitation of osteocytes by mechanical loading-induced bone fluid shear stresses. Journal of Biomechanics 27, 339-360.

Weisstein, E.W., 2004. "Ellipse." From MathWorld -- A Wolfram Web Resource, http://mathworld.wolfram.com/Ellipse.html.

You, L., Cowin, S.C., Schaffler, M.B., Weinbaum, S., 2001. A model for strain amplification in the actin cytoskeleton of osteocytes due to fluid drag on pericelular matrix. Journal of Biomechanics 34, 1375-1386.

You, L., Cowin, S.C., Weinbaum, S., Schaffler, M.B., 2004. Ultrastructure of the osteocyte process and its pericellular matrix. Anatomical Record 278A, 505-513.

Zhang, D., Weinbaum, S., Cowin, S.C., 1998. Estimates of the peak pressure in the bone pore water. Journal of Biomechanical Engineering 120, 697-703.

References For Chapter 3

Ascenzi, A., Benvenuti, A. Orientation of collagen fibers at the boundary between two successive osteonic lamellae and its mechanical interpretation. J Biomech 19: 455-463; 1986.

Ascenzi, A., Bonuci, E., Bocciarelli, D.S. An electron microscopy study of osteon calcification. J Ultrastruct Res 12: 278-303; 1965.

Atkinson, P.J., and Hallsworth, A.S. The spatial structure of bone. Progress in Anatomy 2: 179-199; 1982.

Baud, C.A. Morphology and inframicrosopic structure of osteocytes. Acta Anat. 51: 209-225; 1962.

Beno et al., Yoon, Y.J., Cowin, S.C., Fritton, S.P. Estimation of bone permeability using accurate microstructural measurements. Submitted to J. Biomech., Nov. 2004.

Boyde, A. Scanning electron microscopy studies of bone. In: Biochemistry and physiology of bone (Bourne G.H., ed), 2nd edition, Vol. 1, pp. 250-310. New York: Academic Press, 1972.

Boyde, A. Resolution, sampling and the determination of the lacunar size. In: Bone histomorphometry (Meunier P.J., ed). pp. 399-412. Paris: Armour Montagu; 1972.

Cane, V., Marotti, G., Volpi, G., Zaffe, D., Palazzini, S., Remaggi, F., Muglia, M.A. Size and density of osteocyte lacuna in different regions of long bones. Calcified Tissue International 34: 558-563; 1982.

Cowin, S.C., Weinbaum, S., Zeng, Y. A case for bone canaliculi as the anatomical site of strain generated potentials. J of Biomech 28: 1281-1296; 1995.

Ferretti, M., Muglia, M.A., Remaggi, F., Cane, V., Palumbo, C. Histomorphometric study on the osteocyte lacuna-canalicular network in animals of different species. Italian Journal of Anatomy and Embryology 104: 121-131; 1999.

Frasca, P., Hari Rao, C.V., Richard, A.H., Lawrence, J.K. New method of bone preparation for collagen fiber orientation studies by means of scanning electron Microscopy. J of Dental Research 55: 372-375; 1976.

Gebhardt, W. Uber funktionell wichtige Anordnungsweisen der feineren und groberen lensysteme des Wirbeltieknochens. II. Spezieller Teil. Der Bau der Haversschen Lamel-lensysteme und seine funktionelle Bedeutung. Arch Entwickl Mech Org 20: 187-322; 1906.

Giraud-Guille, M.M. Twisted plywood architecture of collagen fibrils in human compact bone osteons. Calcified Tissue International 42: 167-180; 1988.

Grotz, K.A., Piepkor, B., Al-Nawas, B., Duschner, H., Bittinger, F., Kann, P., Beyer, J., Wagner, W. Confocal laser scanning microscopy: A nondestructive subsurface histotomography of healthy human bone. Calcified Tissue International 65: 8-10; 1999.

Johnson, R.B., Highinson, G.J. A re-examination of the osteocytic network of interdental bone. J. Submisrosc. Cytol. 15(3): 619-625; 1983.

Jowsey, J. Bone in parathyroid disorder in man. In: Mechanics of hard tissue destruction. (Sognnaes R.F., ed.). pp. 447-469. Washington DC. : Amer. A. Advanc. Soi.: 1963.

Klein-Nulend, J., van der Plas, A., Semeins, C.M., Ajubi, N.E., Frangos, J.A., Nijweide, P.J., Burger, E.H. Sensitivity of osteocytes to biomechanical stress in vitro. FASEB 9, 441-445; 1995.

Li, K.C., Zernicke, R.F., Bernard, R.J. Li, A.F.Y. Differential response of rat limb bones to strenuous exercise. J Appl Physiol 70: 554-560; 1991.

Marotti, G. Osteocyte orientation in human lamellar bone and its relevance to the morphometry of periosteocytic lacuna. Metab. Bone Dis. & Rel. Res 1: 325-333; 1979.

Marotti, G. Three dimensional study of osteocyte lacunae. In: Bone Histomorphometry. W.S.S. Jee and A.M. Parfitt, eds. Armour Montagu. Paris, pp. 223-229; 1981.

Marotti, G., Remaggi, F., Zaffe, D. Quantitative investigation on osteocyte canaliculi in human compact and spongy bone. Bone 6: 335-337; 1985.

Marotti, G., Ferretti, M., Remaggi, F., Palumbo, C. Quantitative evaluation on osteocyte canalicular density in human secondary osteons. Bone 16: 125-128; 1995.

Marotti, G. The structure of bone tissue and the cellular control of their deposition. Italian Journal of Anatomy and Embryology 4: 25-79; 1996.

McCreadie, B.R., Hollister, S.J., Schaffler, M.B., Goldstein, S.A. Osteocyte lacuna size and shape in women with and without osteoporotic fracture. J of Biomech 37: 563-572; 2004.

Meunier, P.J., Bernard, J., Vignon, G. The measurement of periosteocytic enlargement in primary and secondary hyperparathyroidism. Israel J. Med. Sci. 3: 482-485; 1971.

Meunier, P.J., Bernard, J., Courpron, P., Vignon, G. Use of image analyzing computer for the study of osteocytic behavior in bone diseases. Proc. IX Europ. Symp. On Calc. Tiss., pp. 203-208. wein: Facta-Publication; 1973.

Mullender, M.G., van der Meer, D.D., Huiskes, R., Lips, P. Osteocyte density changes in aging and osteoporosis. Bone 18: 109-113; 1996a.

Mullender, M.G., Huiskes, R., Versleyen, H., Buma, P. Osteocyte density and histomorphometric parameters in cancellous bone of the proximal femur in five mammalian species. J of Orthopedic Research 14: 972-979; 1996b.

Pawlicki, R. An electron microscopic study of the structure of the wall of the bone canaliculus with particular consideration of the place of its branching. Z. Microsk.-Anat. Forsch., Leipzig 88: 537-544; 1974.

Pawlicki, R. Bone canaliculus endings in the area of osteocyte lacuna. Acta Anat 91: 292-304; 1975.

Reich, K.M., Gay, C.V., Frangos, J.A. Fluid shear stress as a mediator of the osteoblast cyclic adenosine monophosphate production. J Cell Physiol 143: 100-104; 1990.

Remaggi, F., Can, V., Palumbo, C., Ferretti, M. Histomorphometric study on the osteocyte lacuno-canalicular network in animals of different species. I. Woven-fibered and parallel-fibered bones. Italian Journal of Anatomy and Embryology 103: 145-155; 1998.

Sissons, H.A., O'Connor, P. Quantitative histology of osteocyte lacunae in normal human cortical bone. Calcified Tissue International 22: 530-533; 1977.

Smit, T.H., Huyghe, J.M., Cowin, S.C. Estimation of the poroelastic parameters of cortical bone. J of Biomech 35: 829-835; 2002.

Smith, J.W. The arrangement of collagen fibers in human secondary osteons. J Bone and Jt Surgery 42(B): 588-605; 1960.

Tanaka-Kamioka, K., Kamioka, H., Ris, H., Lim, S.S. Osteocyte shape is dependent on actin filaments and osteocyte processes are unique actin-rich projections. J of Bone and Mineral Research 13(10): 1555-1568; 1998.

Vashishth, D., Verborgt, O., Divine, G., Schaffler, M.B., Fyhrie, D.P. Decline in osteocyte lacunar density in human cortical bone is associated with accumulation of microcracks with age. Bone 26(4): 375-380; 2000.

Wang, L., Fritton, S.P., Cowin, S.C., Weinbaum, S. Fluid pressure relaxation depends upon osteonal microstructure: modeling an oscillatory bending experiment. J of Biomech 32, 663-672; 1999.

Wang, L., Ciani, C., Doty, S.B., Fritton, S.P. Delineating bone's interstitial fluid pathway in vivo. Bone 34, 499-509; 2004.

Wang, Y., Schaffler, M., Weinbaum, S., Wang, L. Morphologic variation of the osteocyte lacunar-canalicular system in inbred mice. Proceedings of the Biomedical Engineering Society Annual Fall Meeting, 939; 2004b.

Weinbaum, S., Cowin, S.C., Zeng, Y. A model for the excitation of osteocytes by mechanical loading-induced bone fluid shear stresses. J of Biomech 27: 339-360; 1994.

Weiner, S., Arad, T., Sabanay, I., Traub, W. Rotated plywood structure of primary lamellar bone in the rat: Orientations of the collagen fibril arrays. Bone 20(6): 509-514; 1997.

You, L., Cowin, S.C., Schaffler, M., Weinbaum, S. A model for strain amplification in the actin cytoskeleton of osteocytes due to fluid drag on pericelular matrix. J of Biomech 34(11): 1375-1386; 2001.

You, L., Cowin, S.C., Weinbaum, S., Schaffler, M.B. Ultrastructure of the osteocyte process and its pericellular matrix. Anatomical Record: 278A, 505-513; 2004.

References For Chapter 4

ABAQUS Manuals-V.6.2, 2002. Pawtucket RI, U.S.A.: Hibbitt, Karlsson & Sorensen.

Ascenzi, A., Bonuci, E., and Bocciarelli, D.S. 1965. An electron microscopy study of osteon calcification. J Ultrastruct Res. 12: 287-235.

Ascenzi, A., and Benvenuti, A., 1986. Orientation of collagen fibers at the boundary between two successive osteonic lamellae and its mechanical interpretation. J of Biomech. 19: 455-463.

Ashman, R.B., Cowin, S.C., Van Buskirk, W.C., and Rice, J.C., 1984. A continuous wave technique for the measurement of the elastic properties of cortical bone. J of Biomech. 17: 249-361.

Cowin, S.C., 1999. Bone poroelasticity. J of Biomech. 32: 217-238.

Gebhardt, W., 1906. Uber funktionell wichtige Anordnungsweisen der feineren und groberen lensysteme des Wirbeltieknochens. II. Spezieller Teil. Der Bau der Haversschen Lamel-lensysteme und seine funktionelle Bedeutung. Arch Entwickl Mech Org. 20: 187-322.

Giraud-Guille, M.M., 1988. Twisted plywood architecture of collagen fibrils in human compact bone osteons. Calcified Tissue International. 42: 167-180.

Knothe Tate, M.L., Niederer, P., and Knothe, U., 1998. In vivo tracer transport through the lacunocanalicular system of rat bone in an environment devoid of mechanical loading. Bone. 22: 107-117.

Li, G., Bronk, J.T., An, K., and Kelly, P.J., 1987. Permeability of cortical bone of canine tibiae. Microvascular Research. 34: 302-310.

Marotti, G., Remaggi, F., and Zaffe, D., 1985. Quantitative investigation on osteocyte canaliculi in human compact and spongy bone. Bone. 6: 335-337.

Qin, Y.X., 1997. Fluid flow, matrix strain and loading frequency as independent control parameters in skeletal adaptation. PhD thesis, SUNY.

Smit, T.H., Huyghe, J.M., and Cowin, S.C., 2002. Estimation of the poroelastic parameters of cortical bone. J of Biomech. 35: 829-835.

Steck, R., Niederer, P., and Knothe Tate, M.L., 2003. A finite element analysis for the prediction of load-induced fluid flow and mechanochemical transduction in bone. Journal of Theoretical Biology. 220: 249-259.

Schaffler, M.B., and Burr, D.B., 1988. Stiffness of compact bone: effects of porosity and density. J of Biomech. 21: 13-16.

Wang, L., Fritton, S.P., Cowin, S.C., and Weinbaum, S., 1999. Fluid pressure relaxation depends upon osteonal microstructure: modeling an oscillatory bending experiment. J of Biomech. 32: 663-672.

Zhang, D., Weinbaum, S., and Cowin, S.C., 1998. Estimates of the peak pressure in the bone pore water. Journal of Biomechanical Engineering. 120: 697-703.

References For Chapter 5

Weinbaum, S., Cowin, S.C., and Zeng, Y., 1994. A model for the excitation of osteocytes by mechanical loading-induced bone fluid shear stresses. J of Biomech. 27: 339-360.